

REPORT DOCUMENTATION PAGE			Form Approved OMB NO. 0704-0188	
Public reporting burden for this collection of information estimated to average 1 hour per response, including time for reviewing instructions, searching existing data sources, gathering and maintaining the data needed, completing and reviewing the collection of information. Send comment regarding the burden estimate or any other aspects of this collection of information including suggestions reducing the burden, Washington Headquarters Services, Directorate for Information Operations and Reports, 1215 Jefferson Davis Highway, Suite 1204, Arlington, VA 22202-4302, and to Office of Management and Budget, Paperwork Reduction Project (0704-0188), Washington, DC 20503.				
1. AGENCY USE ONLY (Leave blank)	2. REPORT DATE 11/14/2000	3. REPORT TYPE AND DATES COVERED FINAL REPORT		
4. TITLE AND SUBTITLE  STUDY OF BULK AND SURFACE STATES IN POROUS SILICON			5. FUNDING NUMBERS  DAAHO4-96-1-0405	
6. AUTHOR(S)  Dr. Zvi S. Weisz				
7. PERFORMING ORGANIZATION NAME(S) AND ADDRESS(ES)  University of Puerto Rico, P.O. Box 23343, Rio Piedras, PR 00931-3343			8. PERFORMING ORGANIZATION REPORT NUMBER	
9. SPONSORING/MONITORING AGENCY NAME(S) AND ADDRESS(ES)  U.S. Army Research Office P.O. Box 12211 Research Triangle Park, NC 27709-2211			10. SPONSORING/MONITORING AGENCY REPORT NUMBER  ARO 36312.3- MS-DPS	
11. SUPPLEMENTARY NOTES  The views, opinions and/or findings contained in this report are those of the author(s) and should not be construed as an official Department of the Army position, policy or decision, unless so designated by other documentation.				
12a. DISTRIBUTION/AVAILABILITY STATEMENT  Approved for public release; distribution unlimited.			12b. DISTRIBUTION CODE	
13. ABSTRACT (Maximum 200 words)  In this final report we summarize our findings on the study of Porous Silicon (PSi). We synthesized a variety of PSi films ranging from mesostructures to arrays of nanoparticles of the order of 2nm. We could prepare on regular basis optical quality flat self-supported highly luminescent PSi films. The materials were characterized and we studied their optical, structural and electrical properties. We obtained a correlation between the photoluminescence (PL) properties and the density of surface states, the decay time distribution of the PL signal, and nonlinear properties of the material. We carried out studies of electropolymerization of conductive polypyrrol inside the pores and electroluminescence using liquid electrolyte contacts. We finally synthesized and study nanocrystalline-Si/SiO <sub>2</sub> structures prepared by RF sputtering and start to study the emissions from rare-earth dopants (Er and Eu) and their relation with the nanostructure. We applied our findings to the development of UV-enhanced Si-based photodetectors.				
14. SUBJECT TERMS  Porous Silicon, Luminescence, Surface States, Diffusion Length			14. NUMBER OF PAGES	
			16. PRICE CODE	
17. SECURITY CLASSIFICATION OF REPORT UNCLASSIFIED	18. SECURITY CLASSIFICATION OF THIS PAGE UNCLASSIFIED	19. SECURITY CLASSIFICATION OF ABSTRACT UNCLASSIFIED	20. LIMITATION OF ABSTRACT UL	

20010117 086

DTIC QUALITY INSURED 4

## STATEMENT OF THE PROBLEM.

Photoluminescent porous silicon samples were synthesized and their physical properties studied and correlated with their electrical and optical properties. Samples were prepared by electrochemical anodization. Characterization was carried out using SEM, TEM, AFM, Auger, Raman, time resolved spectroscopy and standard optical and electrical characterization techniques. Electronic surface-states densities were determined using a novel electrolyte-semiconductor blocking array. Phototransport properties were measured using the photocarrier grating technique.

The electrode-PSi formation was investigated, for electroluminescence applications, by promoting electropolymerization in the inner walls of the pores. Applications of porous silicon to the silicon-based UV detector technology were explored.

Nanocrystalline silicon/SiO<sub>2</sub> composites were synthesized and their optical properties studied and compared with PSi. The study of the effects of the nanostructure on the rare earths-doped silicon emissions was initiated with Erbium and Europium.

## SUMMARY OF THE MOST IMPORTANT RESULTS.

- Luminescent porous silicon films synthesized from crystalline silicon wafers with a large variety of doping levels both, n- and p-type, were obtained. The samples had different pore morphologies ranging from porous sizes of the order of microns in width and columnar orientation to nanosize porous with random orientation. Self-supporting flat nanoporous films with optical quality were prepared and studied.
- Combined studies of the photoluminescent spectrum and the electronic surface-state density and effective surface area of the porous silicon surface prepared from Si p-type wafers shown that intensity and spectral position of the photoluminescence spectrum maximum changes as a function of anodizing time attaining a maximum after ~4min anodization. The effective surface area and the density of surface states, on the other hand increases monotonously, the surface state density attaining a value of  $\sim 10^{13} \text{cm}^{-2}$  suggesting that the surface states near the valence band are not involved in the luminescence process.
- For samples for which surface photovoltage spectroscopy revealed a band gap of the order of 2.0eV, the bandtails widths were of the order of 0.3eV. The majority carriers in strongly luminescent films were holes, while in the weakly luminescent films they were electrons even though the starting material in both cases was p-type.
- In macroporous Si we measured an electron diffusion length of 2 $\mu\text{m}$  and a diffusion length for holes (minority carriers) of 0.1 $\mu\text{m}$ .
- Decay time analysis of the photoluminescence of PSi brought to the development of a new approach to extract the decay time distribution. We could obtain the distribution based on the fact that the non-exponential luminescence decay behavior of the sample is multi-exponential.
- Electron Loss Spectroscopy analysis showed that the CO<sub>2</sub> involved in the critical point drying method contaminates the pores' surface with carbon.

## SCIENTIFIC PROGRESS (continuation)

- The study of the growth process of conducting polypyrrol by electropolymerization inside the pores of PSi showed coverage of the inner surfaces according to the curvature and consistent with the electric fields distribution. PSi samples with reduced size of the pores showed limited filling and coverage.
- Optical absorption and Raman measurements of highly porous, optical quality, self supporting films made from p-type Si wafers, permitted us to clarify the characteristics of the nanostructure of the samples. This nanostructure appeared to be an array of spherical nanocrystallites with a lognormal size distribution. The maximum of the distribution is dependent on the preparation parameters but is typically around  $\sim 2.5\text{nm}$  for the optical quality films.
- The analysis of picosecond nonlinear optical response of PSi samples showed a broad and intense absorption band in the UV-visible region with a cut-off edge at  $\sim 400\text{nm}$ . The non-linear optical response consisted of an instantaneous component followed by a long-lived, slowly decaying component. The former is associated with the third-order susceptibility of the material whereas the later originated from the contribution of surface states. The response from surface states was significant and with potential in practical applications.
- Silicon Based UV detector prototypes using luminescent PSi were prepared by growing PSi overlayers on top of a n-p junction. The UV photoresponse at  $366\text{nm}$  was enhanced as compared with control prototypes.
- Photoluminescent nanocrystalline silicon particles embedded in  $\text{SiO}_2$  were synthesized by RF co-sputtering of Si and  $\text{SiO}_2$  targets. Stable photoluminescence ranging from green to deep red was obtained from samples exposed to air.
- Optical absorption and Raman analysis of Si/ $\text{SiO}_2$  composites revealed nanoparticles size distributions peaking in the range between  $1.1\text{nm}$  to  $3.0\text{nm}$ . The measured photoluminescence related with each size distribution was in agreement with the corrected local density approximation calculation.
- Si/ $\text{SiO}_2$  nanocomposites were doped with Erbium and Europium and their photoluminescence properties were analyzed in relation with the nanostructure.
- The intensity of the characteristic  $1.54\mu\text{m}$  emission from  $\text{Er}^{+3}$  was found to be dependent on the nanoparticles size and density. In particular, we observed that, in the range of the Si-particles sizes we studied, larger particles produced larger IR emission. It was also observed that the use of  $\text{Er}_2\text{O}_3$  for the synthesis of the doped composite could introduce large amounts of oxygen and prevent the formation of the silicon nanocrystals.
- We were able to incorporate  $\text{Eu}^{+3}$  into the composite. We also found that we obtained  $\text{Eu}^{+2}$  in the process. The  $\text{Eu}^{+3}$  related photoluminescence peaks were only observed where the size distribution maxima of the nanoparticles were lower than  $1.3\text{nm}$ .

REPORT DOCUMENTATION PAGE (SF298)

(Continuation Sheet)

SCIENTIFIC PROGRESS (continuation)

PERSONNEL

Zvi. S. Weisz, Project Director  
Joseph Shinar, collaborator (AMES National Lab)  
Ram Katiyar, Co-PI (University of Puerto Rico)  
Luis F. Fonseca, collaborator (University of Puerto Rico)

Ravi Soni, Postdoctoral associate

Arturo Ramírez, student. Ph. D. Degree received on October 1997.

Carlos Navarro, student. MSc Degree received on August 2000.

LIST OF PUBLICATIONS

1. *Relation Between Luminescence and Electronic Surface Characteristics in p-type Porous Silicon*, S.Z. Weisz, A. Ramirez Porras, M. Gomez, A. Many, Y. Goldstein and E. Savir, J. Luminescence **72-74**, 729 (1997).
2. *The Relation Between Phototransport and Photoluminescence in Porous Silicon*, I. Balberg, Y. Lubianiker, J. Shinar, J. Partee, Y. Shapira, I. Burstein, S.Z. Weisz and M. Gomez, J. Luminescence **72-74**, 314 (1997).
3. *Luminescence and Surface State Characteristics in p-type Porous Silicon*, A. Ramirez Porras, O. Resto, S.Z. Weisz, Y. Goldstein, A. Many, and E. Savir Mat. Res. Soc. Symp. Proc. **452**, 461 (1997).
4. *The Influence on the Substrate Temperature on the Recombination Processes in a-Si:H*. Y. Lubianiker, I. Balberg, L. Fonseca and S.Z. Weisz, (Amorphous and Micro Crystalline Silicon Technology) Mat. Res. Soc. Proc. **467**, 1209 (1997).
5. *Effects of Aquaregia Treatment on Indium Tin Oxide Substrates on the Behavior of Double Layered Organic Light Emitting Diodes*. F. Li, H. Tang, J. Shinar, O. Resto and S.Z. Weisz, Appl. Phys. Lett. **70**, 2441 (1997).
6. *The Light Intensity Exponent of the Minority Carrier Lifetime and the Mobility Gap States in a-Si:H*, I. Balberg, Y. Lubianiker, L. Fonseca and S.Z. Weisz, J. Non Cryst. Solids, **227-230**, 206 (1998).
7. *Optical Properties and Nanoparticle Size Distribution in Luminescent Porous Silicon*, L.F. Fonseca, O. Resto, R. Katiyar, S. Gupta, S.Z. Weisz, Y. Goldstein, A. Many and J. Shappir. Proc 24th Int. Conference on. The Physics Semiconductor, Editor David Gershoni, World Scientific, 1999 (CD version)..
8. *A New Analysis Method to Characterize the S-Band Luminescence of Porous Silicon*, Jiaqi Yu, Humulin Liu, Yanyun Wang, Weiye Jia, Luis Fonseca, S.Z. Weisz and Oscar Resto. J. Luminescence **81**, 1-6 (1999).

## REPORT DOCUMENTATION PAGE (SF298)

(Continuation Sheet)

## SCIENTIFIC PROGRESS (continuation)

9. *Two Carrier Sensitization as a Spectroscopic Tool for a-Si:H*, L.F. Fonseca, S.Z. Weisz, R. Rapaport and I. Balberg. Mat. Res. Soc. Symp. Proc. **557**, 439 (1999).
10. *Plasmons on Luminescent Porous Silicon Prepared with Ethanol and Critical Point Drying*, O. Resto, L.F. Fonseca, S.Z. Weisz, A. Many and Y. Goldstein. Microcrystalline and Nanocrystalline Semiconductors; Mat. Res. Soc. Symp. Proc. **536**, 229 (1999).
11. *Silicon-Based UV Detector Prototypes Using Luminescent Porous Silicon Films*, Limarix Peraza, Madeline Cruz, Angel Estrada, Carlos Navaro, Javier Avalos, Luis F. Fonseca, Oscar Resto and S.Z. Weisz. Microcrystalline and Nanocrystalline Semiconductors; Mat. Res. Soc. Symp. Proc. **536**, 123 (1999).
12. *Electro-Polymerization in Porous Silicon Film*, R.K. Soni, L.F. Fonseca, O. Resto, A. Guadalupe and S.Z. Weisz. Microcrystalline and Nanocrystalline Semiconductors; Mat. Res. Soc. Symp. Proc. **536**, 197 (1999).
13. *The Effect of Hydrogen on the Network Disorder in Hydrogenated Amorphous Silicon*, S. Gupta, R.S. Katiyar, G. Morell, S.Z. Weisz and I. Balberg., Appl. Phys. Lett., 1999 (in print).
14. *The Effect of Light Soaking on the Structural Order in a-Si:H*, Gupta, R.S. Katiyar, G. Morell, S.Z. Weisz and I. Balberg., Proceedings ICAMS '8, Journal of Non-crystalline Solids, Elsevier Science Publications, 1999, (in print).
15. *Size Dependence of Optical Properties of Silicon Nanocrystals*, R. Soni, L.F. Fonseca, O. Resto, M. Buizaianu, and S.Z. Weisz, J. Luminescence **83**, 187 (1999).
16. *Observation of Picosecond Nonlinear Optical Response from Porous Silicon*, Huimin Liu, Luis F. Fonseca, S.Z. Weisz, Weiye Jia, and Oscar Resto. J. of Luminescence **83-84**, 37 (1999).
17. *Optical Property and picosecond response of Porous Silicon Wafer*. H. Liu, L. F. Fonseca, S. Z. Weisz, Q. Yan, W. Jia, and O. Resto. Nondestructive Characterization of Materials IX, edited by R.E. Green, Jr. AIP, p. 339, (1999).
18. *Line Shape in Resonant Raman Scattering from Silicon Nanoparticles*, R.K. Soni, L.F. Fonseca, O. Resto, S.Z. Weisz and R. Tripathy. Semiconductor Quantum Dots, Mat. Res. Soc. Symp. Proc. **571**, 235 (2000).
19. *Relation Between Electroluminescence and Photoluminescence in Porous Silicon*, E. Savir, J. Jedrzejewski, A. Many, Y. Goldstein, S.Z. Weisz, M. Gomez, L.F. Fonseca, and O. Resto. Materials Science and Engineering B72, 138 (2000).
20. *Comparative Analysis of the 1.54  $\mu$ m Emission of Er-Doped Si/SiO<sub>2</sub> Films and the Size Distribution of the Nanostructure*, Luis F. Fonseca, S.Z. Weisz, O. Resto, R.K. Soni, H. Liu, W. Jia, M. Gomez, A. Many and Y. Goldstein. , Materials Science and Engineering B72, 109 (2000).
21. *Study of the Luminescence of Eu-Doped Nanocrystalline Si/SiO<sub>2</sub> Systems Prepared by RF Co-Sputtering*. G. A. Nery, A. Mahfoud, L. F. Fonseca, H. Liu, O. Resto, and S. Z. Weisz. . Mat. Res. Soc. Symp. Proc. **581** (2000) (in press).

Reprinted from

ZVI CV 84

# JOURNAL OF LUMINESCENCE

---

Journal of Luminescence 72-74 (1997) 729-730

## Relation between luminescence and electronic surface characteristics in p-type porous silicon

S.Z. Weisz<sup>a</sup>, A. Ramirez Porras<sup>a</sup>, M. Gomez<sup>a</sup>, A. Many<sup>b</sup>, Y. Goldstein<sup>b,\*</sup>, E. Savir<sup>b</sup>

<sup>a</sup>*Department of Physics, University of Puerto Rico, Rio Piedras, PR 00931, USA*

<sup>b</sup>*The Racah Institute of Physics, The Hebrew University, Jerusalem 91904, Israel*





ELSEVIER

Journal of Luminescence 72-74 (1997) 729-730

JOURNAL OF  
LUMINESCENCE

## Relation between luminescence and electronic surface characteristics in p-type porous silicon

S.Z. Weisz<sup>a</sup>, A. Ramirez Porras<sup>a</sup>, M. Gomez<sup>a</sup>, A. Many<sup>b</sup>, Y. Goldstein<sup>b,\*</sup>, E. Savir<sup>b</sup>

<sup>a</sup>Department of Physics, University of Puerto Rico, Rio Piedras, PR 00931, USA

<sup>b</sup>The Racah Institute of Physics, The Hebrew University, Jerusalem 91904, Israel

### Abstract

Measurements of photoluminescence, electronic surface states and effective surface area, at various stages of the anodization process, are presented. The results show a behavior different from that observed on n-type porous Si.

**Keywords:** Porous silicon; Luminescence; Surface states

### 1. Introduction

Porous silicon [1] (PS) exhibits high luminescence efficiencies in the visible range. The reasons for the high-efficiency luminescence are still under debate [1,2]. It was suggested that the phenomenon is due to the amorphous or microcrystalline nature of the PS or that the formation of silicon compounds are involved in the luminescence. To gain some insight into this process we employed combined studies of the luminescence spectrum, and the electronic surface-state density and effective surface area of the porous surface.

### 2. Experimental

The starting material was high-grade p-type silicon wafers of resistivity in the range 30–50  $\Omega$  cm.

\*Corresponding author. Fax: 972-2-658-4437; e-mail: YGoldst@vms.huji.ac.il.

A p<sup>+</sup> layer was formed by diffusing Al into one of the faces to attain an ohmic contact. The sample was etched in 20% HF and then anodized in a solution of HF, ethanol and water (1:1:2) with a current density of 100 mA/cm<sup>2</sup>. The PS was studied at different stages of the anodization process. The luminescence was excited by a 10 mW He–Cd laser,  $\lambda = 442$  nm. The anodizing solution was replaced after each anodization stage by an indifferent electrolyte, an aqueous solution of KCl. The electronic measurements were based on the ‘pulsed capacitance’ method at the semiconductor–electrolyte interface and have been described previously [2].

### 3. Results and discussion

In Fig. 1 we present typical luminescence spectra measured after different anodization times, as marked on the spectra. We notice that both the amplitude and the wavelength of the maxima change as a function of anodizing time. This is

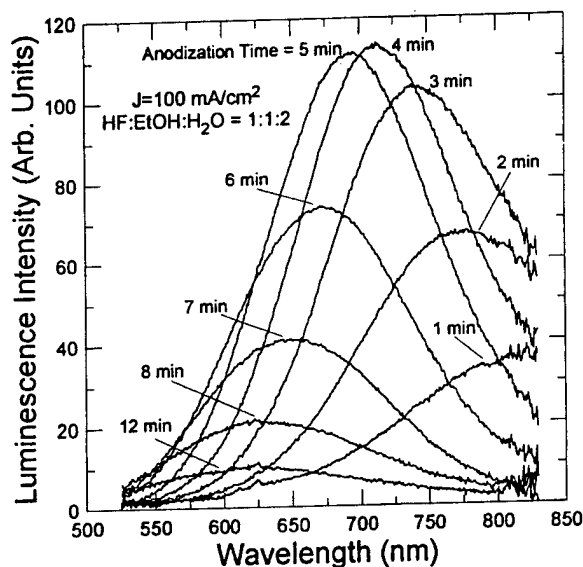


Fig. 1. Luminescence spectra for various anodization times as marked.

illustrated in Fig. 2 where we plotted the amplitude and the wavelength of the maxima as a function of anodizing time. As can be seen, the luminescence spectrum attains a maximum after  $\sim 4$  min anodization, after which it decreases. This is similar to the results found [3] on n-type PS. We measured also the effective surface area and the density of surface states. We found that the effective surface area increases upon anodization fairly monotonously by a factor of 15–40, while the surface-state density increases from  $\sim 2 \times 10^{12} \text{ cm}^{-2}$  for the 'virgin' surface to  $\sim 10^{13} \text{ cm}^{-2}$  for the anodized surface. This increase occurs already after 2 min anodization and the density stays fairly constant upon further anodization. This is quite contrary to n-type PS, where we have found [3] that the surface-state density attains a minimum when the luminescence reaches its maximum. The discrepancy between the two results can be easily reconciled once we realize that in both cases the surface states are measured under accumulation condition. The surface states involved are then those near the majority carrier band edge; namely, near the conduction band for

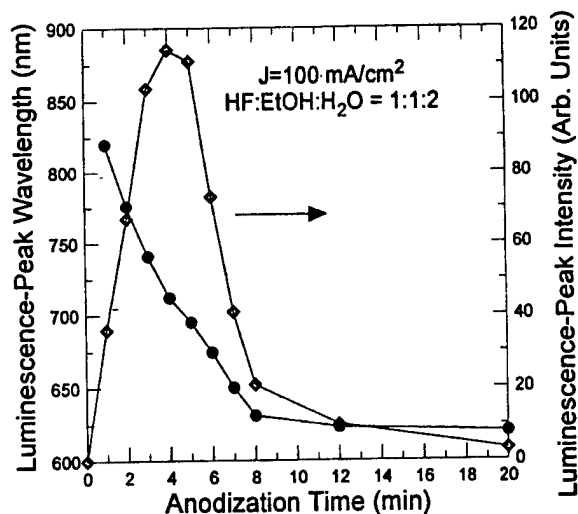


Fig. 2. Peak-luminescence intensity and wavelength as functions of anodization time.

n-type and valence band for p-type. Thus our present results suggest that the surface states near the valence-band edge are not involved in the luminescence process.

#### Acknowledgements

The work in Israel was supported by the Volkswagen Foundation Hannover, Germany, and by the Ministry of Science, Israel, within the framework of the infrastructure-applied physics support project. The work in Puerto Rico was supported by NSF EPSCoR Grant No. OSR-94-52893 and NASA grant No. NCCW-0088.

#### References

- [1] Z.C. Feng and R. Tsu, Porous Silicon (World Scientific, Singapore, 1994).
- [2] F. Koch, Mat. Res. Soc. Symp. Proc. 298 (1993) 319.
- [3] M. Wolovelsky et al., Surf. Sci. 171 (1986) 442.
- [4] S.Z. Weisz et al., Mat. Res. Soc. Symp. Proc. 378 (1995) 899.



Reprinted from

261 CV 85

# JOURNAL OF LUMINESCENCE

---

Journal of Luminescence 72-74 (1997) 314-315

## The relation between phototransport and photoluminescence in porous silicon

I. Balberg<sup>a,\*</sup>, Y. Lubianiker<sup>a</sup>, J. Shinar<sup>b</sup>, J. Partee<sup>b</sup>, Y. Shapira<sup>c</sup>, L. Burstein<sup>c</sup>, S.Z. Weisz<sup>d</sup>,  
M. Gomez<sup>d</sup>

<sup>a</sup>*The Racah Institute of Physics, The Hebrew University, Jerusalem 91904, Israel*

<sup>b</sup>*Ames Laboratory, Department of Physics and Astronomy, Iowa State University, Ames, IA 50011, USA*

<sup>c</sup>*Department of Electrical Engineering, Tel Aviv University, Ramat Aviv 89678, Israel*

<sup>d</sup>*Department of Physics, University of Puerto Rico, Rio Piedras 00931, Puerto Rico*



ELSEVIER



ELSEVIER

Journal of Luminescence 72-74 (1997) 314-315

JOURNAL OF  
LUMINESCENCE

## The relation between phototransport and photoluminescence in porous silicon

I. Balberg<sup>a,\*</sup>, Y. Lubianiker<sup>a</sup>, J. Shinar<sup>b</sup>, J. Partee<sup>b</sup>, Y. Shapira<sup>c</sup>, L. Burstein<sup>c</sup>, S.Z. Weisz<sup>d</sup>, M. Gomez<sup>d</sup>

<sup>a</sup>*The Racah Institute of Physics, The Hebrew University, Jerusalem 91904, Israel*

<sup>b</sup>*Ames Laboratory, Department of Physics and Astronomy, Iowa State University, Ames, IA 50011, USA*

<sup>c</sup>*Department of Electrical Engineering, Tel Aviv University, Ramat Aviv 89678, Israel*

<sup>d</sup>*Department of Physics, University of Puerto Rico, Rio Piedras 00931, Puerto Rico*

### Abstract

We present a summary of a comprehensive study of transport, phototransport, surface photovoltage spectroscopy and luminescence of self-standing films of mesoporous and nanoporous silicon. We conclude that the visible luminescence arises from optical bandtail transitions in the silicon crystallites, while the transport is via a disordered silicon shell that wraps the crystallites.

**Keywords:** Porous silicon; Transport; Phototransport; Surface photovoltage

It has been recently shown that visible photoluminescence (PL) in silicon can result from a quantum confinement (QC) effect. This and the findings in porous silicon (PSi) provide convincing evidence that the strong red PL in PSi is due to QC effects. The next issue that needs to be resolved is the electroluminescence, i.e. the understanding of the transport and the phototransport (PT) in PSi and their relation to the luminescence. Relatively, this issue has not been intensively studied thus far.

Accordingly, we have carried out a comprehensive study of the transport, PT [1, 2], surface photovoltage [3], and PL [4] in 'free-standing' PSi films. In particular, we have studied mesoporous films,

where QC effects are negligible, and nanoporous films, where QC effects are dominant. In this paper we summarize our results [1-4] and derive a self-consistent picture that accounts for them.

All the samples were fabricated from boron-doped c-Si (100) wafers. In order to eliminate the contribution of the c-Si substrate to the surface photovoltage and the electrical conductivity, 'free-standing' films were required. Mesoporous films were prepared from wafers of 0.005  $\Omega\text{cm}$  [1]. Using the Raman spectra, the average crystallite size  $d$  was established to be 10 nm. This and the weak PL that is peaked at 1.05 eV, as in c-Si, determine the 'mesoporous nature' of these samples.

Three sets of nanoporous samples were prepared from c-Si wafers of higher resistivity by using higher current densities [2-4]. The Raman spectra revealed that  $d \approx 3-4$  nm [1], i.e. the 'nanostructure

\* Corresponding author. Fax: 97226585680, e-mail: balberg@vms.huji.ac.il.

nature' of the films. The Raman spectra also contain features which indicate the presence of disorder, as in hydrogenated amorphous silicon (a-Si:H). In the surface photovoltage spectroscopy (SPS) measurements, it was found that the films of one set (set A) were of p-type, the second set (set B) of n-type, and the third set (set C) of 'weak' p-type [3].

Our main experimental results were:

(1) Efficient ( $\eta \sim 1\%$ ) PL in films of set A [4]. This PL peaks at a photon energy  $h\nu$  of 1.7 eV. The peak of the emission of sets B and C was at the same  $h\nu$ , but  $\eta$  was ten times smaller for set C, and was hardly detectable in set B. On the other hand, the photoconductivity in set B was ten times larger than that of set C and it was undetectable in set A. (2) The dark conductivity in all samples was orders of magnitude smaller than that of the wafer substrates. The dark conductivity activation energy is larger than half the optical bandgap or half the energy of the PL photons. If we use the 'microscopic prefactor' of a-Si:H, i.e.  $150 \Omega^{-1} \text{cm}^{-1}$ , the energy separation between the conduction band-edge and the Fermi level is found to be 0.5 eV, in both mesoporous and nanoporous materials. The current-voltage (I-V) characteristics were all linear. It was found that the presence of adsorbed oxygen and/or water vapour reduces the luminescence, enhances the conductivity and the photoconductivity and renders the films n-type. (3) The diffusion length of the electrons in the nanoporous n-type flakes is of the order of 1  $\mu\text{m}$ , while that of the holes is about 0.2  $\mu\text{m}$ . (4) The temperature dependences of the dark and photoconductivities roughly resemble those found in a-Si:H. (5) The width of the photovoltage band-to-band absorption edge is 0.3 eV for both n-type and p-type samples.

In view of the limited scope of this paper we only highlight the conclusions drawn from the above new experimental findings. Based on these results we derive the following self-consistent picture. From the findings (1) and (2) it appears that the

conduction is due to transport in a disordered Si network, and is not due to tunneling between crystallites. From finding (3) it appears that the concepts that apply to bulk semiconductors also apply to PSi, in spite of its coral structure. From findings (3) and (4), it appears that the current flows through the a-Si:H-like shell that wraps the crystallites. From findings (1) and (5) it appears that the dominant optical absorption takes place in the crystallites. Hence, there are both conduction and valence bandtails in the crystallites, which are about 0.3 eV wide. The origin of these tails and of the luminescence is mainly due to the relaxation of the lattice momentum selection rules. The PL is due to radiative transitions between the crystallites' bandtails. The high efficiency of the PL is due to the combination of this relaxation and the geometrical-potential confinement of the carriers in the crystallites.

Ames Laboratory is operated by Iowa State University for the US Department of Energy under Contract W-7405-Eng-82. The work was partially supported by the Director for Energy Research, Office of Basic Energy Sciences. The work in Israel was partially supported by the Volkswagen Foundation Hannover, Germany, and partially by the Ministry of Science and Arts, Israel, within the framework of the infrastructure-applied physics support project. The work in Puerto Rico was supported by NSF EPSCoR Grant OSR No. 94-52893 and NASA grant No. NCCW-0088.

## References

- [1] Y. Lubianiker, I. Balberg, G. Morrell, R.S. Katiyar and S.Z. Weisz, in: Proc. 22nd Int. Con. on the Physics of Semiconductors (World Scientific, Singapore, 1995) p. 2129.
- [2] Y. Lubianiker, I. Balberg, J. Partee and J. Shinar, *J. Non Cryst. Solids* 198–200 (1996) 949.
- [3] L. Burstein, J. Partee, J. Shinar, Y. Lubianiker, Y. Shapira and I. Balberg, *Phys. Rev. B* 55 (January 15, 1997).
- [4] R. Shinar, D.S. Robinson, J. Partee, D.A. Lane and J. Shinar, *J. Appl. Phys.* 77 (1995) 3403.

## LUMINESCENCE AND SURFACE-STATE CHARACTERISTICS IN P-TYPE POROUS SILICON

A. RAMIREZ PORRAS,\* O. RESTO,\* S.Z. WEISZ,\* Y. GOLDSTEIN,\*\* A. MANY,\*\* AND E. SAVIR\*\*

\*Department of Physics, University of Puerto Rico, Rio Piedras, PR 00931

\*\*Racah Institute of Physics, The Hebrew University, Jerusalem 91904, Israel

### ABSTRACT

Pulse measurements on the porous-Si/electrolyte system are employed to determine the surface effective area and the surface-state density at various stages of the anodization process used to produce the porous material. Such measurements were combined with studies of the photoluminescence spectra. These spectra were found to shift progressively to the blue as a function of anodization time. The luminescence *intensity* increases initially with anodization time, reaches a maximum and then decreases with further anodization. The surface state density, on the other hand, increases with anodization time from an initial value of  $\sim 2 \times 10^{12} \text{ cm}^{-2}$  for the virgin surface to  $\sim 10^{13} \text{ cm}^{-2}$  for the anodized surface. This value is attained already after  $\sim 2$  min anodization and upon further anodization remains fairly constant. In parallel, the effective surface area increases by a factor of 10 - 30. This behavior is markedly different from the one observed previously for n-type porous Si.

### INTRODUCTION

Porous silicon,<sup>1-4</sup> (PS) obtained by electrochemical etching procedures applied to crystalline Si surfaces, exhibits high luminescence efficiencies in the visible range. It is quite clear now that the visible luminescence originates from the band-gap enlargement due to quantum confinement.<sup>4</sup> At the same time, the reasons for the high-efficiency luminescence are still somewhat under debate.<sup>4,5</sup> It was suggested that it is the amorphous<sup>6</sup> or microcrystalline<sup>7</sup> nature of the porous Si that is responsible for the phenomenon, or that the formation of silicon compounds such as siloxene ( $\text{Si}_6\text{O}_3\text{H}_6$ ) or species of Si-H, Si-O and Si-F bonds are involved in the luminescence.<sup>8</sup> One way of gaining further insight into the luminescence process is to carry out a variety of measurements on samples of different porosity. To that end we have employed combined studies of the luminescence spectrum, the surface-state density and the effective surface area of the porous surface. Such studies were carried out at different stages of the anodization process and thus for different morphologies of the porous surface. The luminescence spectra were measured by conventional methods. The surface state characteristics and the effective surface area were determined by pulse measurements<sup>9</sup> on the PS/electrolyte system. This system is particularly suitable since a capacitative contact to the terrain of the porous surface is best achieved by an electrolyte, and it was successfully used<sup>10</sup> to investigate n-type PS. There we found<sup>10</sup> a strong correlation between the surface-state density near the conduction band edge and the luminescence intensity. In this paper we present similar measurements on *p-type* porous Si and we compare the results with those obtained on n-type material.

### EXPERIMENTAL

The starting material was high-grade p-type silicon wafers of resistivity in the range 20 - 50  $\Omega\text{cm}$ . A  $p^+$  layer was formed by diffusing metallic Al into one of the faces to obtain an ohmic

$P_{ss0}$  of "occupied" surface states.  $V_{s0}$  and  $P_{s0}$  can be determined quite accurately from measurements in the depletion range.<sup>12</sup> The entire plots of  $P_s$  and  $P_{ss}$  vs.  $V_s$  can then be constructed by using the relations  $V_s = V_{s0} + \delta V_s$ ,  $P_s = P_{s0} + \delta P_s$ , and  $P_{ss} = P_{ss0} + \delta P_{ss}$ . So much so in the absence of an insulating buffer layer (such as an oxide) at the semiconductor surface. If such a layer is present, the as-measured barrier height, i. e., the measured voltage drop between the Pt electrode and the  $p^+$  contact just after the pulse termination, yields  $V_s + V_g$ , where  $V_g$  is the voltage drop across the insulating layer.

## RESULTS AND DISCUSSION

In Fig. 1 we present typical photoluminescence spectra of p-type PS surfaces prepared by anodization. The different anodization times are marked on the spectra. We notice that the luminescence intensity at the beginning increases with anodization time, attains a maximum and then decreases. This behavior is illustrated by the higher curve in Fig. 2 and is quite similar to that observed<sup>10</sup> previously for n-type PS. The lower curve in Fig. 2 shows the appreciable blue shift of the spectra, suggesting that, on the average, the porous structure gets finer with anodization time.

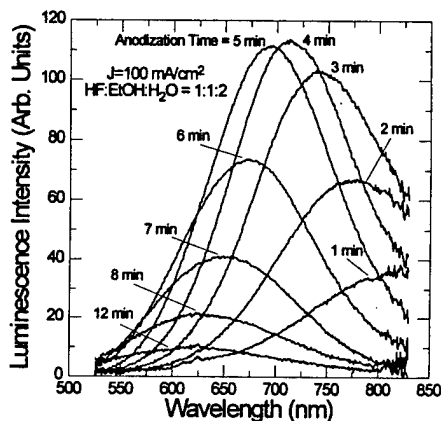


Fig. 1. Photoluminescence spectra for various anodization times, as marked.

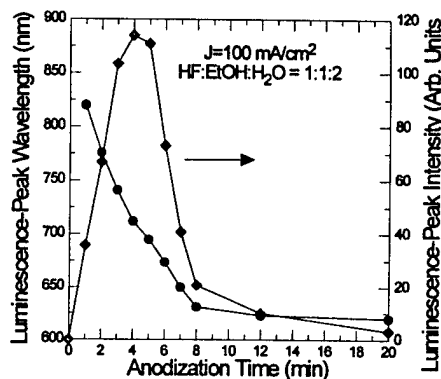


Fig. 2. Peak-photoluminescence intensity and wavelength as functions of anodization time for the sample in Fig. 1.

Typical results of the free surface-hole density  $P_s$  (diamonds) and the density of occupied surface states  $P_{ss}$  (stars) against the as-measured barrier height  $V_s + V_g$  as obtained for an etched virgin silicon surface, are displayed in the semilog plot of Fig. 3. In the depletion range,  $P_s$  is negative but, because of the logarithmic scale used, the plot is that of  $-P_s$ . The light curve, in the accumulation range, labeled  $C_g = \infty$ , represents the theoretical dependence of  $P_s$  on  $V_s$  for a buffer-free surface ( $C_g = \infty$ ,  $V_g = 0$ ), as derived from a solution of Poisson's equation for the value of the hole bulk concentration  $p_b$  marked in the figure. It is seen that this curve does not account well for the data in the accumulation range. The best fit, represented by the bold curve, labeled  $C_g = 4.5 \mu\text{F}/\text{cm}^2$ , was obtained by assuming the presence of an insulating buffer layer of  $C_g = 4.5 \mu\text{F}/\text{cm}^2$ , corresponding to a thickness of  $\sim 4 \text{ \AA}$ . Most probably this layer consists of an oxide, but a small contribution of the series Helmholtz layer cannot be ruled out. Again, this behavior is similar to that found on n-type PS. Turning now to the surface-state hole occupancy  $P_{ss}$ , it is seen to rise slowly from a low value of  $\sim 10^{11} \text{ cm}^{-2}$  at  $V_s + V_g \approx -0.5 \text{ V}$  up to  $\sim 10^{14} \text{ cm}^{-2}$

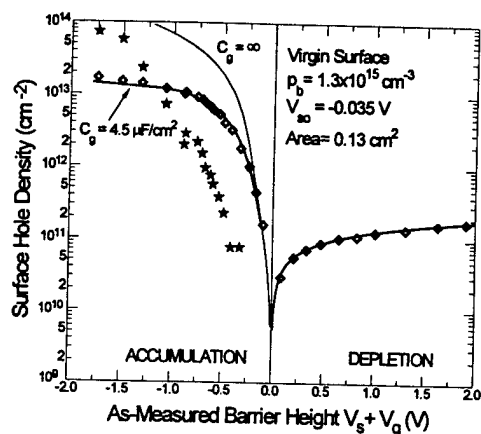


Fig. 3. Free surface hole density  $P_s$  (diamonds) and density of occupied surface states  $P_{ss}$  (stars) vs. the as-measured barrier height  $V_s + V_g$  for a virgin Si surface. The light and bold curves are theoretical plots of  $P_s$  as explained in the text.

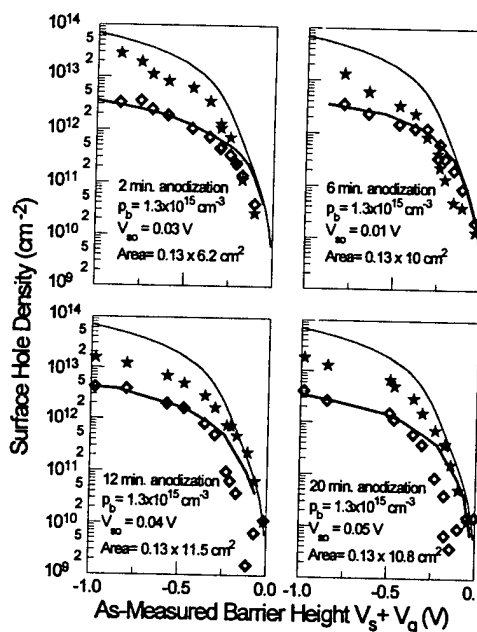


Fig. 4.  $P_s$  (diamonds) and  $P_{ss}$  (stars) vs.  $V_s + V_g$  for four anodized, porous Si surfaces. The light and bold curves are theoretical plots of  $P_s$ .

at  $V_s + V_g \approx -2$  V. No saturation value for the surface-state density could be reached. This is quite different than the behavior we found<sup>10</sup> on n-type PS, where the surface-state density saturated at  $10^{12}$  cm<sup>-2</sup>. Because of this lack of saturation, we shall use the values of  $P_{ss}$  at  $V_s + V_g \approx -1$  V to compare surface state occupancies for different anodization times. For the case of the virgin surface, this value is  $\sim 2 \times 10^{12}$  cm<sup>-2</sup>.

Results of  $P_s$  and  $P_{ss}$ , similar to those in Fig. 3, for four porous surfaces are presented in Fig. 4. These results were obtained after the sample of Fig. 3 has been anodized for different times, as marked in the figure. Since our aim is to compare the surface-state densities, we show only the accumulation range here. Because of the increase of the effective surface area, the highest surface potential barriers (for holes) attained were around -1 volt. The curves in the figure are theoretical, calculated for the same  $C_g$  values as in Fig. 3. We notice again that for all four porous surfaces, the surface-state density (stars) increases monotonously with the potential barrier through the whole region shown and does not exhibit signs of saturation. As mentioned above, we choose for comparison the values of  $P_{ss}$  at  $\sim -1$  volt. These values in the figure are scattered around  $2 \times 10^{13}$  cm<sup>-2</sup>, about an order of magnitude higher than on the virgin surface. However, the interesting thing is that this surface-state density remains fairly constant with anodization time, very much different from the results found<sup>10</sup> for n-type PS. A behavior similar to that of the surface states was observed also for the effective surface area. In Fig. 5 the surface area factor, i. e. the ratio of the effective area to the area of the virgin sample, for two typical samples is plotted against the anodization time. The area factors were derived from measurements of the type shown in Figs. 3 and 4 in the strong accumulation range. The results for the two samples are qualitatively the same; the area factor increases with anodization time till it reaches a saturation. The saturation values observed varied from sample to

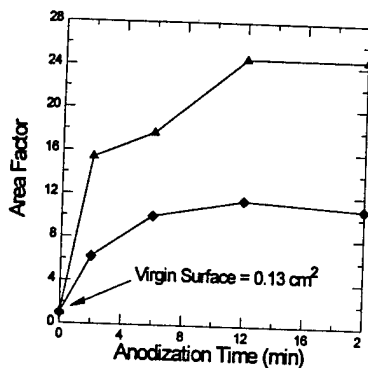


Fig. 5. Surface area factor vs. anodization time for two samples.

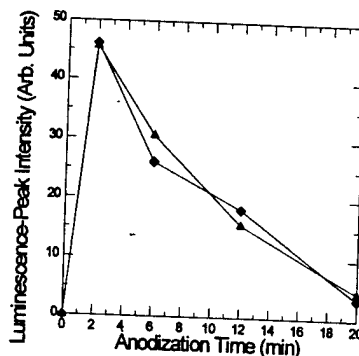


Fig. 6. Photoluminescence-peak intensity vs. anodization time for two samples.

sample between 10 and 30.

In parallel with the surface-state density, we measured the photoluminescence spectrum for each anodization time. These measurements were performed after the measurements on the PS/electrolyte system. In Fig. 6 the luminescence-peak intensity is plotted against the anodization time for the same two samples as in Fig. 5. We notice that the maximum luminescence peak obtains already after 2 min anodization and then the luminescence decreases upon further anodization. In Fig. 7 we plot the value of the luminescence-peak wavelength as a function of anodization time. The peak shifts to the blue upon anodization close to 200 nm from its value at 2 min anodization.

Comparing the results of Figs. 6 and 7 to those in Fig. 2 we notice that they both show comparable blue shifts, but there is a discrepancy in the anodization time needed to attain maximum luminescence. To check the influence of the KCl electrolyte used in the electronic measurements, we measured the spectra on PS samples that after anodization were immersed for 10 min into a KCl electrolyte. The results are shown in Fig. 8 and, for comparison, we also re-plotted the corresponding curve from Fig. 1. We notice that the KCl treatment does not shift the maximum to a different anodization time, however, it does lower the luminescence intensity. This latter is probably due to adsorption of some species, from the electrolyte. Thus we ascribe the

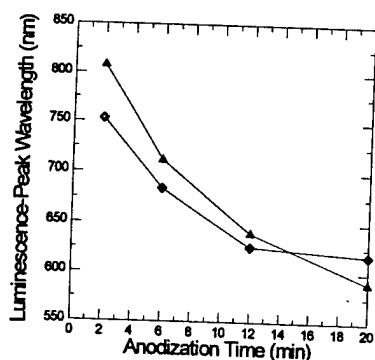


Fig. 7. Photoluminescence-peak wavelength vs. anodization time for two samples.

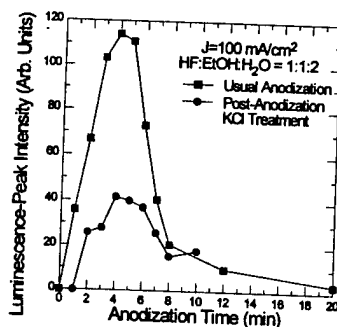


Fig. 8. Photoluminescence-peak intensity for an untreated and for a KCl treated sample vs. anodization time.

shift of the anodization time for maximum luminescence, to possible surface damage due to the application of the voltage pulses.

## CONCLUSION

P-type PS behaves quite differently from that of n-type PS. While the photoluminescence intensity exhibits a pronounced maximum with anodization time, the effective surface area and the surface state density appear to reach a more or less constant value as a function of anodization time. This is in contrast to n-type PS, where a close correlation between the effective surface area, the luminescence intensity and the surface-state density was found.<sup>10</sup> The discrepancy between the two results can be reconciled once we realize that in both cases the surface states are measured under accumulation conditions. The surface states involved are then those near the majority carrier band edge; namely, near the conduction band for the n-type material and near the valence band for the p-type material. Thus our present results suggest that the surface states near the valence-band edge are not involved in the luminescence process.

## ACKNOWLEDGMENT

The work in Israel was supported by the Volkswagen Foundation Hannover, Germany, and by the Ministry of Science, Israel, within the framework of the infrastructure-applied physics support project. The work in Puerto Rico was supported by NSF EPSCoR Grant No. OSR-94-52893, by NASA grant No. NCCW-0088 and U.S. Army Research Office grant No. DAAHO4-96-1-0405.

## REFERENCES

1. L.T. Canham, Appl. Phys. Lett. **57**, 1046 (1990).
2. I. Amato, Science **252**, 922 (1991).
3. A.G. Cullis and L.T. Canham, Nature **353**, 335 (1991).
4. For the recent developments in this field see: Z.C. Feng and R. Tsu, *Porous Silicon* (World Scientific, Singapore, 1994).
5. F. Koch in *Silicon Based Optoelectronic Materials*, edited by R.T. Collins, M.A. Tischler, G. Abstreiter, and M.L. Thewalt (Mater. Res. Soc. Proc. **298**, Pittsburgh, PA, 1993) pp. 319-324.
6. R.P. Vasquez, R.W. Fathauer, T. George, A. Ksendzov and T.L. Lin, Appl. Phys. Lett. **60**, 1004 (1992).
7. J.S. Foresi and T.D. Moustakas in *Light Emission from Silicon*, edited by S.S. Iyer, L.T. Canham, and R.T. Collins (Mater. Res. Soc. Proc. **256**, Pittsburgh, PA, 1992) pp. 77-82.
8. M.S. Brandt, H.D. Fuchs, M. Stutzmann, J. Weber and M. Cardona, Solid State Commun. **81**, 307 (1992).
9. M. Wolovelsky, J. Levy, Y. Goldstein, A. Many, S.Z. Weisz and O. Resto, Surf. Sci. **171**, 442 (1986).
10. S.Z. Weisz, J. Avalos, M. Gomez, A. Many, Y. Goldstein, and E. Savir in *Defect- and Impurity-Engineered Semiconductors and Devices*, edited by S. Ashok, J. Chevallier, I. Akasaki, N.M. Johnson, and B.L. Soporì (Mater. Res. Soc. Proc. **378**, Pittsburgh, PA, 1995) pp. 899-904.
11. A. Many, Y. Goldstein, and N.B. Grover, *Semiconductor Surfaces* (North-Holland, Amsterdam, 1971).
12. S.Z. Weisz, J. Penalbert, A. Many, S. Trokman, and Y. Goldstein, J. Phys. Chem. Solids **51**, 1067 (1990).



## THE INFLUENCE OF THE SUBSTRATE TEMPERATURE ON THE RECOMBINATION PROCESSES IN a-Si:H

Y. LUBIANIKER<sup>1</sup>\*, I. BALBERG<sup>1</sup>, L. FONSECA<sup>2</sup> and S.Z. WEISZ<sup>2</sup>

<sup>1</sup>Racah Institute of Physics, the Hebrew University, Jerusalem 91904, Israel

<sup>2</sup>Department of Physics, University of Puerto Rico, Rio Piedras, PR 00931

### ABSTRACT

We have studied the four phototransport properties as a function of temperature in undoped a-Si:H films deposited with different substrate temperatures in the range 150 - 225°C. The analysis of the results indicates how  $T_s$  determines the densities of the various defects. The general trend of decrease of both the density of dangling bonds and the Urbach energy is in agreement with the weak bond breaking model. However, we conclude that a slight modification of this model is required.

### INTRODUCTION

One of the most important parameters in the deposition of a-Si:H films and devices is the substrate temperature,  $T_s$ . Previous works have shown that the variation of  $T_s$  effects the Urbach energy ( $E_U$ ) and the density of dangling bonds [1], degree of disorder [2], concentration of Hydrogen in the film [3] and the phototransport properties [4]. The latter, and in particular the mobility-lifetime,  $\mu\tau$ , product of the minority carriers, are of particular importance for the production of high quality bipolar devices, such as solar cells [5]. Despite that importance and the basic interest in the properties of the material, the understanding of the exact relation between the phototransport properties and the nature and concentration of the various defects is still at a rudimentary stage. It is thus still unclear to which extent the minimization of material properties such as  $E_U$  and the density of the dangling bonds really leads to the optimization of the phototransport properties.

Recent works [6-8] have proposed that the recombination processes in a-Si:H are determined by an interplay between the valence band tail states and the dangling bonds. Specifically, it was suggested that at room temperature the phototransport of the majority carriers (i.e. the electrons) is determined by the dangling bonds, while the phototransport of the minority carriers (the holes) is determined by the valence band tail states [7]. In this paper we examine the validity of this suggestion by directly measuring the phototransport properties as a function of the temperature in a series of a-Si:H films. The only difference in the way these films were prepared was the  $T_s$  under which the deposition took place. The properties which were measured include the  $\mu\tau$  products of the two carriers and the exponents that characterize their light intensity dependence ( $\gamma$  and  $S$  for the electrons and the holes, respectively). As we have previously shown, this procedure provides quite a complete characterization of the recombination kinetics [9]. The determination of these four phototransport properties is done through the measurement of the photoconductivity,  $\sigma_{ph}$ , and ambipolar diffusion length,  $L$ , and the application of the relations [5]:

$$(\mu\tau)_e = \sigma_{ph} / qG \quad (1)$$

$$(\mu\tau)_h = qL^2 / 2kT \quad (2)$$

$$\sigma_{ph} \propto G^\gamma \quad (3)$$

$$L \propto G^{-\delta} \quad (4)$$

Here  $q$  is the electronic charge,  $G$  is the photogeneration rate and  $kT$  is the thermal energy.

As we show below, the results we obtained from the temperature dependence of these quantities confirm the current understanding of the recombination kinetics, yielding an excellent agreement with the conclusions of our recent Raman scattering study [2] of these films. We further show that the results are consistent in their gross features with the weak bonds breaking model [1], although further considerations should be made in order to account for the slight deviations of the experimental results from this theory.

## EXPERIMENTAL

The a-Si:H films used in this study were prepared using the rf glow discharge decomposition of silane technique. The substrates were made of Corning 7059 glass. The substrate temperatures during deposition were 150, 175, 200 and 225°C (samples 1 - 4, respectively), and the deposition rate was about 4 Å/sec. The thickness of all the films was about 0.8 μm. The a-Si:H films were deposited on top of predeposited NiCr layers, which provided coplanar ohmic contacts, with a 0.4 mm separation.

The phototransport properties were determined using the photocarrier grating (PCG) technique [5,10]. This technique yields the phototransport properties of the two charge carriers by the simultaneous measurement of  $\sigma_{ph}$  and  $L$ , followed by the application of equations (1) - (4). The light source in our measurements was a He-Ne laser with a wavelength of 633 nm. The maximum illumination flux used was 10 mW/cm<sup>2</sup>, corresponding to a photogeneration rate of  $G = 2 \cdot 10^{20}$  cm<sup>-3</sup>sec<sup>-1</sup>. For the determination of the light intensity exponents we have reduced the above photogeneration rate in steps, down to  $10^{19}$  cm<sup>-3</sup>sec<sup>-1</sup>. The samples were placed in a cryostat, which enabled us to carry out the measurements in the temperature range of 180 - 350°K.

## EXPERIMENTAL RESULTS

Following the above outlined procedure we have measured the four phototransport properties, for all four samples, as a function of the temperature. All the results are presented in Fig. 1. Starting with the majority carriers we present in Fig. 1(a) the temperature dependence of  $(\mu\tau)_h$ . It can be seen that for sample 1 ( $T_s = 150^\circ\text{C}$ )  $(\mu\tau)_h$  increases monotonically with temperature, and its values are considerably lower (by more than an order of magnitude) than those obtained for all other samples. The temperature dependence of  $(\mu\tau)_h$  in the other films is more complicated: At first  $(\mu\tau)_h$  increases sharply with temperature, and then at a much slower pace. This is a manifestation of the well known thermal quenching (TQ) of  $\sigma_{ph}$  [6,11]. The temperatures at which the TQ occurs ( $T_{TQ}$ ) are about 200, 220 and 250°K for samples 2 - 4, respectively.

It is well known that the TQ is accompanied by a cusp in the temperature dependence of corresponding exponent,  $\gamma$  [6,8,11]. In Fig. 1(b) it can be seen that indeed such peaks are observed for samples 2 - 4, thus confirming the above explanation of the results of Fig. 1(a). We can also see in Fig. 1(b) that for sample 1  $\gamma$  is monotonically decreasing. This, and the

trend of  $T_{TQ}$ , suggest that for sample 1 the TQ occurs at a temperature which is lower than the experimental range accessible in our measurements.

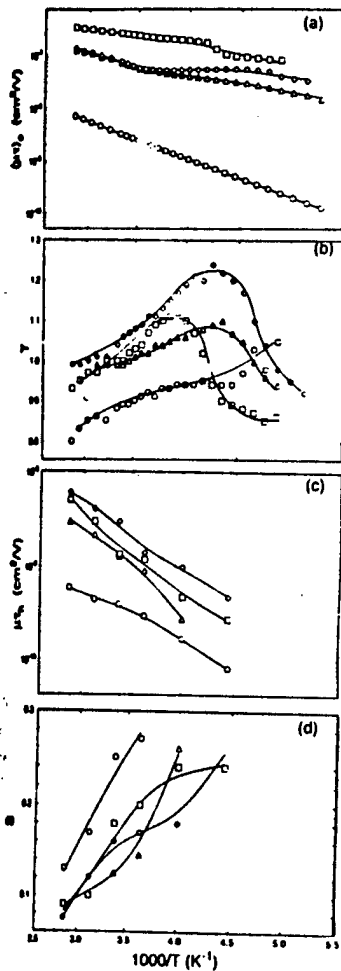


Fig. 1: The measured temperature dependence of the phototransport properties for samples 1 ( $T_s = 150^\circ\text{C}$ , circles), 2 ( $T_s = 175^\circ\text{C}$ , triangles), 3 ( $T_s = 200^\circ\text{C}$ , diamonds) and 4 ( $T_s = 225^\circ\text{C}$ , squares). The smooth lines are drawn to guide the eye.

Turning to the minority carriers, we present in Fig. 1(c) the temperature dependence of  $(\mu\tau)_h$  for our four samples. We can see that for all the samples  $(\mu\tau)_h$  increases monotonically with  $T$ . However, the  $T_s$  dependence of  $(\mu\tau)_h$  is not monotonic as that of  $(\mu\tau)_e$ : For samples 1 - 3 we observe an increase of  $(\mu\tau)_h$  with  $T_s$ , while for sample 4 the  $(\mu\tau)_h$  values are lower than those of sample 3, indicating that  $T_s = 200^\circ\text{C}$  is an optimal value for obtaining a high value of  $(\mu\tau)_h$ . Finally, we present in Fig. 1(d) the temperature dependence of the light intensity exponent of the minority carriers,  $S$ . There are two characteristics to be noted in the behavior of  $S$ : First,  $S$  has a non-zero value throughout the temperature range of this study, indicating that at least two different types of defects are involved in the recombination process [9]. Second, for all samples  $S$  is monotonically decreasing with temperature.

In order to summarize the influence of  $T_s$  on the phototransport properties as described above, we plot the  $T_s$  dependence of the two  $\mu\tau$  products (as measured at  $250^\circ\text{K}$ ) in Fig. 2(a), and of the  $T_{TQ}$  in Fig. 2(b). Since we did not find experimentally the value of  $T_{TQ}$  for sample 1 we have plotted an extrapolated dotted line for  $T_s$  values below  $175^\circ\text{C}$ .

## DISCUSSION

For the interpretation of the experimental results, let us first review the recombination model which is commonly used for the analysis of phototransport properties. We consider a recent version of this model which was analyzed in detail by Tran [6]. The model consists of a valence band tail which is roughly twice wider than the conduction band tail, and a single type of dangling bond centers, which are assumed to be neutral in equilibrium. Accordingly, there are a-priori three possible recombination channels. However, since the capture cross sections of the states in the two band tails are assumed to be symmetric, the higher total density of valence band tail states causes the

recombination rate via this tail to dominate the recombination rate via the conduction band tail at all temperatures. The temperature dependence of the phototransport properties is determined then by the recombination interplay between the valence band tail states and the dangling bonds.

Recent publications have shown quite convincingly that at low temperatures the majority carriers lifetime is determined by the valance band tail [6,8]. As the temperature increases, the thermal release of trapped holes causes a decrease of the recombination rate through this channel, and an increase in the recombination rate through the dangling bonds. This process continues until at high enough temperatures the electrons lifetime is determined solely by the dangling bonds. Naturally, there is a temperature at which the recombination rate through the two channels is about equal, and Tran has shown [6] that this is the temperature at which the thermal quenching takes place (i.e.  $T_{TQ}$ ). The TQ is caused then by a transition between temperature regions where different channels dominate the recombination process. For lower light intensity a higher temperature is required for such a transition, leading to the high sensitivity of  $(\mu\tau)_e$  to the light intensity at temperatures around  $T_{TQ}$ . This is manifested by the cusp in  $\gamma(T)$ . Furthermore, the existence of two compatible recombination channels enables that cusp to exceed unity, contrary to a situation where only one recombination channel is operative (a situation which leads to  $\gamma \leq 1$  [9]).

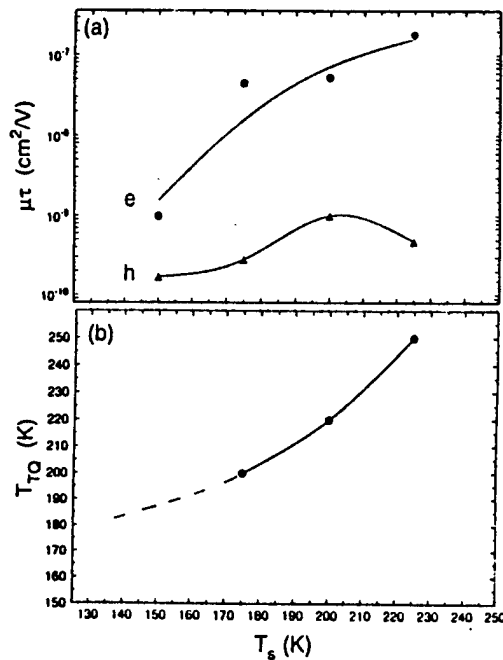


Fig. 2: The effect of  $T_s$  on (a) the values of the two  $\mu\tau$  products (taken at 250°K) and on (b) the thermal quenching temperature.

Turning to the minority carriers, it is expected that their lifetime will increase monotonically with temperature [6]. Based on the measurement of  $(\mu\tau)_h$  as a function of light soaking time Wang and Schwarz [7] concluded that at room temperature the holes lifetime is determined by the valance tail states, while the electrons lifetime is determined by the dangling bonds (i.e. that  $T_{TQ}$  is lower than room temperature). According to their analysis the dominance of the holes lifetime by the dangling bonds will be achieved only above 350°K. Recently we have shown [8] that correspondingly the exponent  $S$  should decrease with increasing  $T$  from a non zero value, which is related to the recombination process in the valance band tail, to a value of zero, which is related to the recombination process in the dangling bonds.

With all this in mind, we can now see that all the experimental results in Fig. 1 are in agreement with this model. The TQ of  $\sigma_{ph}$  is indeed accompanied by a peak in  $\gamma$  with

values higher than unity. The minority carrier  $\mu\tau$  product increases and the exponent  $S$  decreases with increasing temperature. It should be emphasized, however, that since  $S$  does not reach a zero value for any of the samples, we must conclude that there is no range of the temperature interval under study in which the dangling bonds control solely the holes recombination process. Hence, the current results provide further support to Tran's recombination model.

In view of that we can obtain spectroscopic information regarding the influence of  $T_s$  on the density of the various defects. We saw in both Fig. 1(a) and Fig. 2(a) that  $(\mu\tau)_h$  increases with the increase of  $T_s$ . This means, in accordance with previous suggestions [1], that there is a reduction of the total defect density as  $T_s$  increases within the  $T_s$  interval under study. Furthermore, following the analysis of Tran [6], we conclude that the increase of the  $T_{TQ}$  with  $T_s$  (Fig. 2(b)) indicates that the ratio of the concentrations of dangling bonds to the valence band tail states also decreases with  $T_s$ . Hence, the new conclusion of this study is that the most important effect of the increase of  $T_s$  is a reduction in the concentration of the dangling bonds. While the electrons recombination is determined by both the dangling bonds and the tail states, the holes recombination, as discussed above, is dominated by the valence band tail in the temperature interval studied here. Hence, the conclusion from Figs. 1(c) and 2(a) is that as  $T_s$  increases from 150°C to 200°C the valence band tail becomes narrower, giving rise to the increase of  $(\mu\tau)_h$ . However, a further increase of  $T_s$  causes a slight decrease in  $(\mu\tau)_h$ , which must be attributed then to a rewidening of the valence band tail. It thus seems that while the reduction of the concentration of the dangling bonds is monotonic with  $T_s$ , this is not the case for the valence band tail width, for which a minimal value is obtained for an optimal substrate temperature. Indeed it is possible [1] that the minimum of the  $E_U$  found here for  $T_s = 200^\circ\text{C}$  is only a local minimum, and that a further increase of  $T_s$  will result in a further reduction of  $E_U$ . The current results show then that the relation between  $E_U$  and the concentration of the dangling bond density is not trivial (see below).

Since this discussion is based only on the analysis of the phototransport data, we now turn to examine previous works in which the effect of  $T_s$  was studied by other means. We have recently presented a study of these films by Raman scattering [2], and found that the degree of disorder in our a-Si:H films decreases from sample 1 to 3, and then increases slightly for sample 4. This is true both for the short range disorder (i.e. width of the bond angle distribution) which effects the location and width of the spectral band of the transverse optical (TO) mode, and for the intermediate range disorder (i.e. dihedral angle distribution) which determines the ratio of the intensities of the transverse acoustic, TA, spectral band to the TO spectral band. Since the disorder in the a-Si:H is related to  $E_U$  [12] the results of the Raman scattering are consistent with the interpretation given above for the phototransport data. Furthermore, this shows that the decrease of  $(\mu\tau)_h$  with the increase of  $T_s$  from 200 to 225°C is not an experimental artifact but rather a true property of the material.

The dependencies of the defect density in the tails and in the dangling bonds on  $T_s$  have been analyzed in detail by Stutzmann [1]. Correspondingly, he suggested the weak bonds breaking (WBB) model, in which the dangling bonds originate from spontaneous break of weak silicon-silicon bonds whose energy exceeds a certain critical limit. Hence, a higher  $E_U$  means more states above this critical energy, and thus a higher density of dangling bonds. Stutzmann has further showed, by examining a collection of experimental results (obtained by different experimental methods), that minimal values for both the density of dangling bonds and the  $E_U$  are obtained for  $T_s$  of about 300°C. It is obvious then that our finding of decreasing density of dangling bonds is consistent with the collection of experimental data presented by Stutzmann.

We note, however, that the slight increase concluded here for the  $E_0$  in sample 4 seems to be in disagreement with the WBB model. It seems then that our results, while generally in agreement with this model, suggest that more refined details which depend on  $T$ , may be important. Examples for such details are the density of states at the mobility edge, the concentration of hydrogen, or the energy of the gap. The effect of these parameters will be considered elsewhere.

In conclusion, we have studied the phototransport properties as a function of temperature for a-Si:H samples deposited under different substrate temperatures. We have shown that the results are consistent with Tran's recombination model, and that the changes with  $T$ , are generally in agreement with the weak bond breaking model. However, a refinement of this model should be considered.

#### ACKNOWLEDGEMENT

The authors are indebted to A. Catalano and G. Wood for the samples used in this study. This work was supported in part by NSF-EPSCoR grant No. GSR-9452893, and in part by ARO grant No. DAAHO4-96-1-0405.

#### REFERENCES

- [1] M. Stuttmann, *Phil. Mag. B* **60**, 531 (1989).
- [2] G. Morell, R.S. Katiyar, S.Z. Weisz, H. Jia, J. Shinar and I. Balberg, *J. Appl. Phys.* **78**, 5120 (1995).
- [3] A.H. Mahan, B.P. Nelson, S. Solomon and R.S. Crandall, *Mat. Res. Soc. Symp. Proc.* **219**, 673 (1991).
- [4] M.H. Farias, A. Roche, S.Z. Weisz, H. Jia, J. Shinar, Y. Lubianiker and I. Balberg, *Mat. Res. Soc. Symp. Proc.* **336**, 425 (1994).
- [5] For a review see, I. Balberg, *Mat. Res. Soc. Symp. Proc.* **258**, 693 (1992).
- [6] M.Q. Tran, *Phil. Mag. B* **72**, 35 (1995).
- [7] F. Wang and R. Schwarz, *Phys. Rev. B* **52**, 14586 (1995).
- [8] Y. Lubianiker, R. Naidis, I. Balberg, L. Fonseca and S.Z. Weisz, *Mat. Res. Soc. Symp. Proc.* **420**, 777 (1996).
- [9] I. Balberg, *J. Appl. Phys.* **75**, 914 (1994).
- [10] D. Ritter, E. Zeldov and K. Weiser, *Appl. Phys. Lett.* **49**, 791 (1986).
- [11] H. Fritzsche, M.Q. Tran, B.-G. Yoon and D.-Z. Chi, *J. Non-Cryst. Solids* **137-138**, 467 (1991).
- [12] G.D. Cody, T. Tiedje, B. Abeles, B. Brooks and Y. Goldstein, *Phys. Rev. Lett.* **47**, 1480 (1981).

\* Present address: Department of Physics, University of Oregon, Eugene OR 97403.

# Effects of aquaregia treatment of indium–tin–oxide substrates on the behavior of double layered organic light-emitting diodes

F. Li, H. Tang, and J. Shinar

Ames Laboratory–USDOE and Department of Physics and Astronomy, Iowa State University, Ames, Iowa 50011

O. Resto and S. Z. Weisz

Department of Physics and Materials Research Center, University of Puerto Rico, Rio Piedras, Puerto Rico 00931

(Received 15 January 1997; accepted for publication 25 March 1997)

The effects of a controlled aquaregia treatment of indium–tin–oxide (ITO) substrates on the behavior of highly efficient vacuum evaporated double layered 8-tris-hydroxyquinoline Al ( $\text{Alq}_3$ )-based light-emitting diodes are described. It is found that in suitably treated devices, both current injection and the electroluminescence (EL) are significantly enhanced. The enhancement is believed to result from the greater ITO/hole transporting layer contact areas and the contact conditions. The observed dependence of  $I(V)$ , the EL output, and the EL efficiency on the ITO surface morphology indicates that space-charge-limited currents dominate the behavior of the devices. © 1997 American Institute of Physics. [S0003-6951(97)04020-5]

Transparent conducting indium tin oxide (ITO) is used widely as the anode material in organic light-emitting diodes (OLEDs) due to its efficient hole injection properties.<sup>1–5</sup> It is also generally recognized that the cleanliness of the ITO surface is an important factor governing the performance of the devices. Consequently, many cleaning methods such as scrubbing, ultrasonication, chemical washing, vapor degreasing, irradiation in a UV–ozone chamber, etc., have been developed to treat its surface.<sup>6–8</sup> Yet no studies of the effect of the ITO surface morphology on the electroluminescence (EL) of OLEDs have been reported. In order to study this effect, we developed a simple method to treat ITO by etching it with diluted aquaregia. This letter describes its effects on double-layered OLEDs with an 8-tris-hydroxyquinoline Al ( $\text{Alq}_3$ ). We show that their performance is strongly dependent on the ITO surface morphology and that optimized treatment yields highly efficient devices.

Figure 1 shows the structure of the OLEDs, which consist of the aquaregia-treated Applied Films Corp. ITO substrate (untreated sheet resistance of  $\sim 20 \Omega/\text{sq}$ ), a 500 Å thick hole transporting layer (HTL), a 500 Å thick  $\text{Alq}_3$  layer, and a 1800 Å thick  $\text{Mg}_{0.9}\text{Ag}_{0.1}/\text{Ag}$  layer. The HTL was either a “three-armed star” (3-AS) 4,4',4"-tris[*N*-(3-methoxyphenyl)-*N*-phenylamine–triphenylamine] or triphenyl diamine (TPD). The molecular structures of  $\text{Alq}_3$ , 3-AS, and TPD are shown in Fig. 2.

The aquaregia was prepared by adding  $\text{HNO}_3$  to HCl very slowly, to a ratio of 1:3, and letting the mixture brew for 15 min. The aquaregia was then diluted with distilled water to a 1:5 ratio. The extent of the aquaregia etching of the ITO was monitored via its sheet resistance  $R$ , which increased with etching. After thorough cleaning with an ultrasonic surfactant wash and rinsing with distilled water followed by acetone, the ITO substrate was immersed in the diluted aquaregia in an ultrasonic washer. When the substrate's sheet resistance reached the desired value, it was rinsed in distilled water, followed by acetone, isopropanol, and blown dry with pure  $\text{N}_2$ .

Both the HTL and  $\text{Alq}_3$  were deposited by thermal evaporation of the source materials in a vacuum chamber

with a base pressure of  $10^{-6}$  Torr located in a high-purity dry  $\text{N}_2$  glove box, in which water and oxygen levels were typically less than 1 ppm. The deposition rate of the organic layers was 3–5 Å/s. A 1500 Å  $\text{Mg}_{0.9}\text{Ag}_{0.1}$  metal mixture was coevaporated on the  $\text{Alq}_3$  from separate sources at a rate of 5 Å/s Mg and 0.5 Å/s Ag, in a separate vacuum chamber with a base pressure of  $10^{-6}$  Torr. A 300 Å thick Ag layer was deposited on the MgAg layer to inhibit oxidation. The broadband EL intensity  $I_{\text{EL}}$  was measured with a calibrated silicon photodiode.  $I(V)$  and  $I_{\text{EL}}(V)$  measurements were all performed in air.

Figures 3 and 4 display  $I(V)$  and  $I_{\text{EL}}(V)$ , respectively, of LEDs with 3-AS and TPD deposited on treated ITO with varying  $R$ . To minimize the effects due to variations in the fabrication procedure, the 3-AS and TPD devices were fabricated simultaneously. As clearly seen, at any given bias, all devices with treated ITO had moderately higher  $I$  and much higher  $I_{\text{EL}}$  than those with untreated ITO. Indeed, relative to devices with untreated ITO, optimal treatment enhanced  $I_{\text{EL}}$  more than 100-fold and  $I$  more than tenfold over a broad bias range, which translates into a considerably higher luminescence efficiency  $\eta$ . The treated ITO devices also exhibited a lower EL threshold voltage  $V_{\text{th}}$ .

We note that the optimal treatment depended on the HTL. For 3-AS, treated ITO with  $R \approx 30 \Omega/\text{sq}$  exhibited the lowest  $V_{\text{th}}$  ( $\sim 4.2$  V) and highest  $I$  and  $I_{\text{EL}}$  at all bias. For TPD, however, the devices with  $R \approx 70 \Omega/\text{sq}$  exhibited the lowest  $V_{\text{th}}$  ( $\sim 5$  V) and highest  $I$  and  $I_{\text{EL}}$  at all bias voltages.

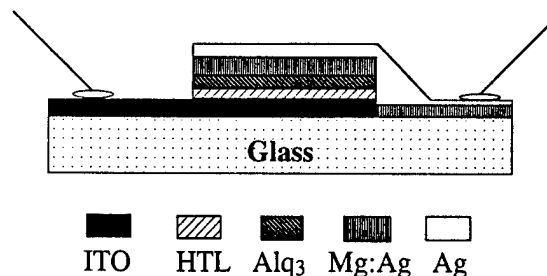


FIG. 1. The structure of a typical organic LED described in this work.

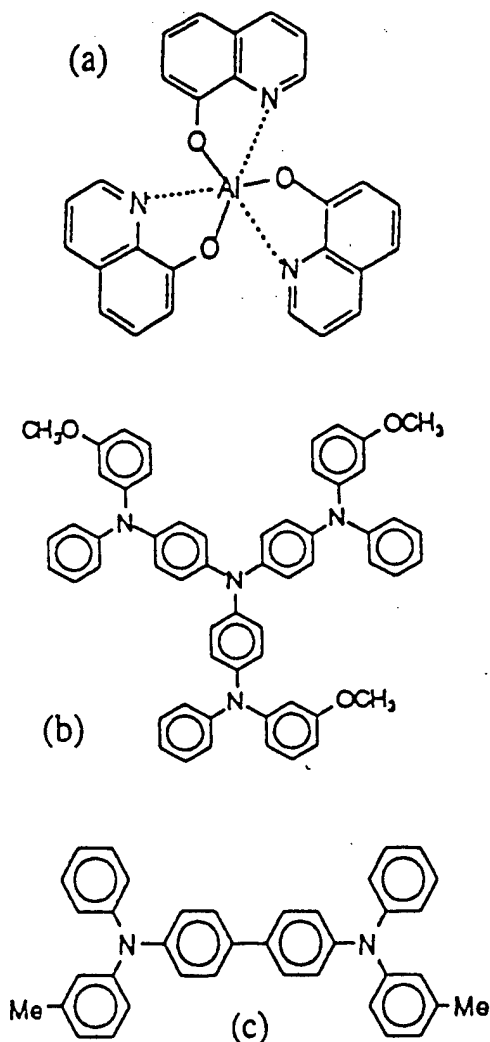


FIG. 2. Molecular structures of (a) 8-tris-hydroxyquinoline Al (Alq<sub>3</sub>), (b) "three-armed star" (3-AS) 4,4',4''-tris[N-(3-methoxyphenyl)-N-phenylamine-triphenylamine], and (c) triphenyl diamine (TPD).

Note that the ionization potentials of 3-AS and TPD are 4.9 and 5.2 eV, respectively. At high bias, the current injected into 3-AS was much higher than into TPD, but  $I_{EL}$  of the former saturated at lower  $V$  than that of the latter. In the high bias region, it was also observed that the decay rate of  $I_{EL}$  was proportional to the injection current density, consistent with other studies.<sup>8</sup>

Figures 3 and 4 also suggest that in LEDs with treated ITO and two HTLs such as 3-AS/TPD, lower  $V_{th}$ , higher  $I_{EL}$ , and high  $\eta$  should be observed over a broad bias region, consistent with other observations.<sup>9</sup> We note that in all devices, the  $I(V)$  curves followed a power-law behavior above  $V_{th}$ , but below  $V_{th}$  they clearly deviated from such behavior.

In order to understand the behavior of these LEDs, we performed both x-ray photoelectron spectroscopy (XPS) and atomic force microscopy (AFM) measurements on the aquaregia-treated ITO. XPS indicated no chemical difference between the treated and untreated ITO. However, the AFM images presented in Fig. 5 show that the surface morphology of the treated ITO is more porous than that of the untreated ITO. In OLEDs, both space-charge-limited (SCL) injection effects and tunneling processes have been used to explain

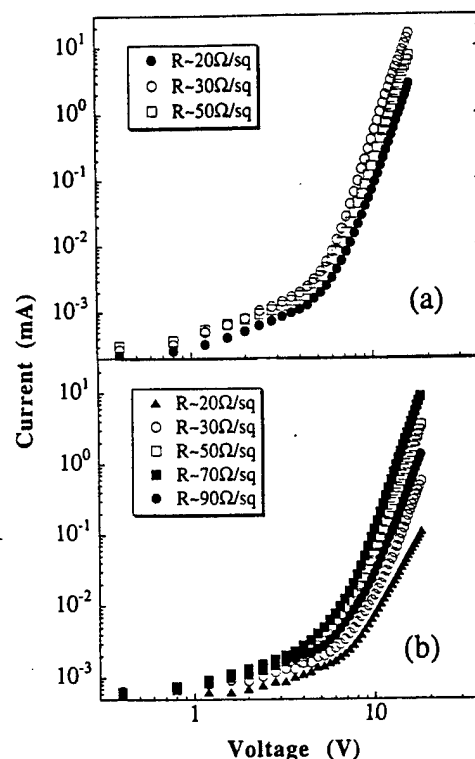


FIG. 3.  $I(V)$  behaviors of LEDs with (a) 3-AS as the HTL, and (b) TPD as the HTL.

some aspects of the  $I(V)$  and  $I_{EL}(V)$  behaviors.<sup>10,11</sup> It is also generally accepted that tunneling dominates for large barriers while SCL current injection is dominant in smaller barriers. Based on the latter, Burrows and Forrest suggested that in ITO/TPD/Alq/MgAg devices the  $I(V)$  curve is controlled by trapped-charge-limited (TCL) electron transport through

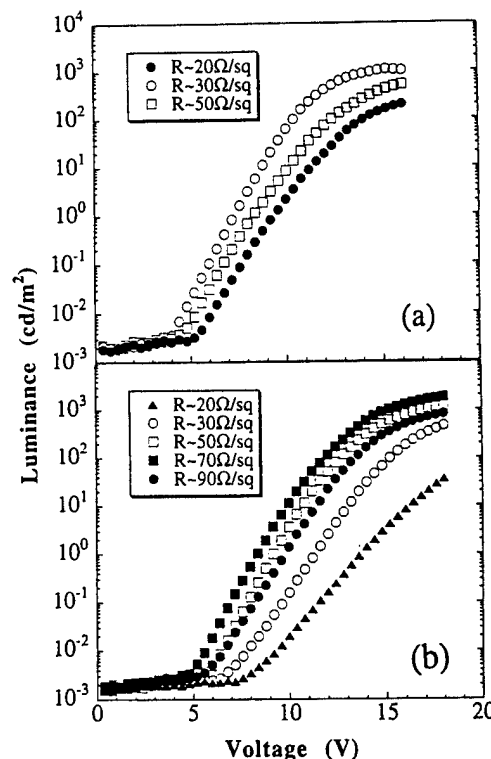


FIG. 4.  $I_{EL}(V)$  behaviors of LEDs with (a) 3-AS as the HTL, and (b) TPD as the HTL.



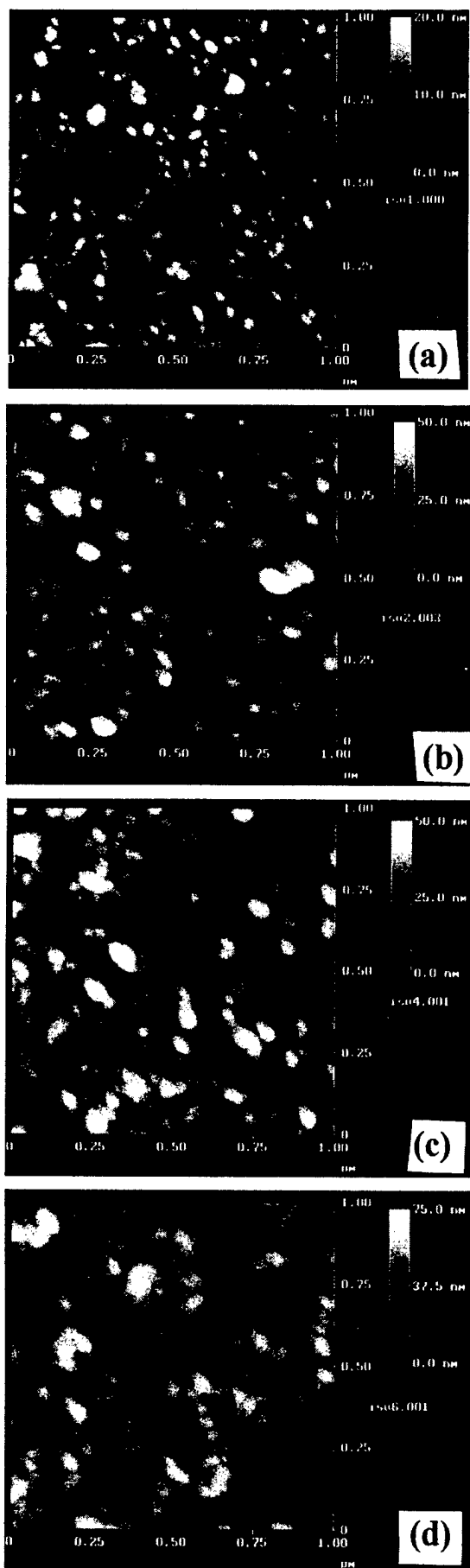


FIG. 5. AFM images of (a) untreated ITO (surface sheet resistance  $\sim 20 \Omega/\text{sq}$ ) and aquaregia-treated ITO with surface sheet resistances of (b)  $\sim 30 \Omega/\text{sq}$ , (c)  $\sim 70 \Omega/\text{sq}$ , and (d)  $\sim 90 \Omega/\text{sq}$ .

$\text{Alq}_3$ .<sup>10</sup> Yet, the porous surface morphology of aquaregia-treated ITO provides more contact area with the organic layer, which induces greater hole injection into the HTL. This can account for the lower  $V_{\text{th}}$  in the LEDs with treated ITO; the power-law behavior of  $I(V)$  above  $V_{\text{th}}$  is consistent with the SCL current mechanism. However, the observed dependence of  $I(V)$  and  $\eta$  on surface morphology of the ITO is equivalent to their dependence on the ITO/HTL. This suggests that the SCL currents are not only controlled by TCL electron transport through  $\text{Alq}_3$ , but also by hole injection from the ITO to the HTL, as well as hole transport through the HTL and injection from the HTL into the  $\text{Alq}_3$ .

SCL effects alone, however, cannot completely account for the relative behavior of the LEDs. From Fig. 5, it is clear that the surface of the  $\sim 30 \Omega/\text{sq}$  treated ITO is not the most porous, yet the LEDs with 3-AS fabricated on such treated ITO exhibited the largest  $I$  above  $V_{\text{th}}$  among all devices with either 3-AS or TPD. These results, and the fact that the voltage drop across the ITO (typically  $\sim 1 \text{ mA} \times 50 \Omega \approx 50 \text{ mV}$ ) is negligible, indicate that effects other than the ITO/HTL contact area are significant. Although their nature is unclear, our results do show that with the optimized aquaregia treatment enhanced hole injection, EL output, and EL efficiency are achieved.

In summary, we have found that by using aquaregia-treated ITO substrates, both current injection and EL output of double-layered organic LEDs are significantly improved. The improvement is believed to be due to enhanced hole injection current density from the ITO into the hole transporting layer, resulting from the increased contact area as well as the contact conditions between them. The observed dependence of the  $I(V)$  characteristics, EL output, and EL efficiency on the ITO surface morphology indicate that space-charge-limited currents, which are determined by the bulk properties of the organic materials, are dominant in double-layered  $\text{Alq}_3$ -based LEDs.

The authors thank Dr. M. Bernius and Dr. E. P. Woo for valuable discussions. Ames Laboratory is operated by ISU for the U.S. DOE under Contract No. W-7405-Eng-82. This work was partially supported by The Dow Chemical Company, NSF Grant No. DMR-9202981, and the Director for Energy Research, Office of Basic Energy Sciences, USDOE.

<sup>1</sup> C. W. Tang and S. A. VanSlyke, *Appl. Phys. Lett.* **51**, 913 (1987).

<sup>2</sup> J. H. Burroughes, D. D. C. Bradley, A. R. Brown, R. N. Mark, K. Mackay, R. H. Friend, P. L. Burn, and A. B. Holmes, *Nature (London)* **347**, 539 (1990).

<sup>3</sup> D. Braun and A. J. Heeger, *Appl. Phys. Lett.* **58**, 1982 (1991).

<sup>4</sup> A. R. Brown, D. D. C. Bradley, J. H. Burroughes, R. H. Friend, N. C. Greenham, P. L. Burn, A. B. Holmes, and A. Kraft, *Appl. Phys. Lett.* **61**, 2793 (1992).

<sup>5</sup> G. Gustafsson, Y. Cao, G. M. Treacy, F. Klavetter, N. Colaneri, and A. J. Heeger, *Nature (London)* **357**, 477 (1992).

<sup>6</sup> S. Saito, T. Tsutsui, M. Era, N. Takada, C. Adachi, Y. Hamada, and T. Wakimoto, in *Electroluminescent Materials, Devices, and Large-Screen Displays*, edited by E. M. Conwell, M. Stolka, and M. R. Miller [SPIE Proc. **1910**, 212 (1993)].

<sup>7</sup> E. Aminaka, T. Tsutsui, and S. Saito, *J. Appl. Phys.* **79**, 8808 (1996).

<sup>8</sup> S. A. Van Slyke, C. H. Chen, and C. W. Tang, *Appl. Phys. Lett.* **69**, 2160 (1996).

<sup>9</sup> F. Li, H. Tang, and J. Shinar (unpublished).

<sup>10</sup> P. E. Burrows and S. R. Forrest, *Appl. Phys. Lett.* **64**, 2285 (1994).

<sup>11</sup> J. R. Sheats, H. Antoniadis, M. Hueschen, W. Leonard, J. Miller, R. Moon, D. Roitman, and A. Stocking, *Science* **273**, 884 (1996).

# The light intensity exponent of the minority carrier lifetime and the mobility gap states in a-Si:H

I. Balberg <sup>a,\*</sup>, Y. Lubianiker <sup>a</sup>, L. Fonseca <sup>b</sup>, S.Z. Weisz <sup>b</sup>

<sup>a</sup> Racah Institute of Physics, Hebrew University, Jerusalem-91904, Israel

<sup>b</sup> Department of Physics, University of Puerto Rico, San Juan 00931, Puerto Rico

## Abstract

We recently gave physical arguments that the recombination in a single type of dangling bond centers will yield a zero value for the light intensity exponent of the minority carriers,  $\lambda$ . We then concluded that the observed  $\lambda \neq 0$  value in a-Si:H indicates the presence of other states in its mobility gap. In this paper, we substantiate those arguments by an analytic proof, by computer simulations and by considering our recent experimental findings on the temperature dependence of  $\lambda$ . In particular, we show that in an n-type photoconductor the dangling bond acts as a single acceptor-like recombination center. © 1998 Elsevier Science B.V.

**Keywords:** Light intensity exponent; Minority carriers; Mobility gap

## 1. Introduction

The ability to measure the ambipolar diffusion length in hydrogenated amorphous silicon, a-Si:H, has provided another source of information regarding the state distribution in this material [1–5]. However, one parameter which can be derived from the corresponding measurements has hardly been discussed [1,2,5]. This is the light intensity exponent,  $\lambda$ , which is associated with the minority carrier recombination time,  $\tau_h$ , by the definition,  $\tau_h \propto G^{-\lambda}$ , where  $G$  is the carrier generation rate. Recently, we have applied [1] a Rose-like [6] argument [7] to find the above-mentioned information from the dependence of  $\lambda$  on various controllable parameters. This application yielded the conclusion that  $\lambda$  is a unique parameter

in the sense that it can provide a qualitative test for the presence of recombination centers other than a single type of dangling bonds. In particular, we concluded that a  $\lambda \neq 0$  is an indication that at least one other type of recombination center must be active. Following this conclusion we, suggested that in a-Si:H, one must assume the presence of other types of states. Such states are bandtails [8–10] and/or other types of dangling bonds [2,4]. A priori, the well-known [8–10] existence of bandtails would immediately suggest that we should have  $\lambda \neq 0$  and thus this test is trivial. However, it is expected [9,10] that above room temperature, the recombination rate in the bandtails is diminished and thus the  $\lambda \neq 0$  phenomenon is informative, indicating other active recombination processes. This makes the  $\lambda \neq 0$  test a conclusive tool for state distribution spectroscopy for semiconductors in general and for amorphous semiconductors in particular.

\* Corresponding author. Fax: +972-2-6584437; e-mail: balberg@vms.huji.ac.il.

Following these considerations and since we gave [1] only qualitative arguments in support of this test, it appeared important to substantiate the above argument by an analytical proof and by model simulations. This need was further amplified when the relevance of the test to a-Si:H was questioned. The doubts came following an analytical argument [5] that there is a possible ‘curious situation’ for which a  $\lambda \neq 0$  value can be found for a single type of dangling bonds in a-Si:H. In the present paper, we also disprove that claim by analytical, numerical and experimental results.

The structure of this paper is as follows. In Section 2, we derive analytically the expression for the lifetime of both charge carriers in the case of a single acceptor-like level showing that it is the same as the one obtained for the single type of dangling bonds. Then we determine the corresponding values of  $\lambda$ . In Section 3, we apply the model to a-Si:H and show that it cannot produce the  $\lambda \neq 0$  result claimed in Ref. [5]. Finally, in Section 4, we discuss experimental results and present our main conclusion.

## 2. Analytical derivation of the light intensity exponents

The four parameters which can be derived from phototransport measurements are the electron and hole mobility-lifetime products,  $\mu_e \tau_e$ ,  $\mu_h \tau_h$ , and their corresponding exponents,  $\gamma$  and  $\lambda$  [1–5]. The light intensity exponents,  $\gamma$  and  $\lambda$ , are defined by  $\tau_e \propto G^{\gamma-1}$  and  $\tau_h \propto G^\lambda$ . We note in passing that in other papers the parameter  $\lambda$  was defined as  $2S$  [1,3] or  $\phi_h$  [2]. The dependence of these four parameters on  $E_c - E_F$  has been used [2,3,5] for deriving information on the state distribution in a-Si:H. Here,  $E_c$  is the conduction band edge,  $E_F$  is the dark (equilibrium) Fermi level.

We turn then to prove that in an n-type semiconductor, the single dangling bond acts as a single acceptor-like recombination center. For this, we assume that  $n_i/p_i > 1$ , where  $n_i$  and  $p_i$  are the steady state concentrations of free electrons and holes under light excitation. Since the p-type photoconductor yields a symmetric situation, we do not discuss it here.

Let us start our analytic derivation with the sim-

plest version of the Shockley–Read analysis for a deeply lying acceptor-like state [6,7]. For the electrons in this system we assume a capture coefficient,  $\sigma_n^0$ , and for the holes a capture coefficient,  $\sigma_p^-$ . If the concentration of these states is  $N_a$ , a fraction of them,  $f^- N_a$ , is occupied by electrons and a fraction of them,  $(1 - f^-) N_a$ , is occupied by holes. Under steady state conditions the recombination rates for electrons and holes must be equal, so that:  $n_i(\sigma_n^0 N_a)(1 - f^-) = p_i(\sigma_p^- N_a)f^-$ . Using the definition of the ‘deep trapping times’ [7]  $\tau_n^0 \equiv 1/(\sigma_n^0 N_a)$  and  $\tau_p^- \equiv 1/(\sigma_p^- N_a)$  we obtain then that the steady state kinetics is governed by the relation:

$$n_i(1 - f^-)/\tau_n^0 = p_i f^-/\tau_p^- \quad (1)$$

Eq. (1) is *exactly* the expression obtained in Ref. [5] for the n-type photoconductor ( $n_i > p_i$ ) in which the recombination center is the multilevel, occupation-correlated, dangling bond. In particular, it is important to note (see below) that this result is found in Ref. [5] for both the high and low  $n_i/p_i$  cases. This finding and the fact that Eq. (1) was derived here using the single level Shockley–Read model justifies, a posteriori, our argument [1] that the dangling bond acts as a single level-like recombination center. In turn it disproves the claim in Ref. [5] that the low  $n_i/p_i$  case (the ‘curious situation’) ‘does not exist in the classical Shockley–Read recombination scheme’. Hence, to make Eq. (1) pertinent to the case of a single type of dangling bonds, all that has to be done is simply replace  $N_a$  by the concentration of dangling bonds,  $N_{db}$ .

Let us now discuss  $\gamma$  and  $\lambda$  which are relevant to the recombination via acceptor-like states. For this purpose, we repeat briefly the argument given by Rose [6] (for  $\gamma$ ) and by Balberg [1] and Balberg and Lubianiker [3] (for  $\lambda$ ), but, this time, in relation to Eq. (1).

Consider then two distinct situations under the condition (both assumed in Refs. [1,5]) that  $N_a \gg n_i, p_i$ . The first case is when  $f^- \approx 1 - f^- \approx 0.5$ . In this case [1], the increase of  $G$  and thus the increase of  $n_i$  and  $p_i$  will hardly effect the electron occupation of the recombination centers, and their recombination times,  $\tau_n^0/(1 - f^-)$  and  $\tau_p^-/f^-$ , will be independent of  $G$ . We will have then that  $\gamma = 1$  and  $\lambda = 0$ . The other extreme case is when  $f^- \geq 1$  so that

$(1 - f^-)N_a \geq n_f$ . In this case, the charge neutrality restriction will not allow  $n_f$  to increase with  $G$  without a corresponding increase of  $(1 - f^-)$ , so that the condition  $n_f = (1 - f^-)N_a$  must be obeyed. If so, since the steady state recombination rate equals  $G$ , i.e., (see Eq. (1))  $G \propto n_f(1 - f^-)N_a$ , we get that  $G \propto n_f^2$  and thus  $\gamma = 1/2$ . On the other hand,  $f^-N_a$  is essentially a constant and since  $G \propto p_f f^- N_a$  we get that  $\lambda = 0$ . The transition from the first case to the other can be obtained [1] by moving  $E_F$  towards  $E_c$ . Consequently, the value of  $\gamma$  shifts from 1 to  $1/2$  with increase of  $E_F$ , while  $\lambda = 0$  is maintained throughout the increase of  $E_F$ .

In principle, it is possible (see Section 3) that, even if  $n_f > p_f$ , under an extreme ratio of the recombination capture coefficients, we will still have a situation where  $f^- \ll 1$  so that the charge neutrality condition is  $p_f = f^- N_a$ .

This 'curious situation' is noted in Ref. [5] in which  $(1 - f^-)N_a$  is practically a constant, and  $G \propto p_f f^- N_a$ . Hence, under the requirements of charge neutrality we get that  $G \propto p_f^2$  and that  $G \propto n_f$ , yielding  $\lambda = -1/2$  and  $\gamma = 1$ . It is important to note then, that in general we will *never* have a situation where  $\gamma \neq 1$  and  $\lambda \neq 0$  simultaneously, since, mathematically, we cannot have that both  $f^-$  and  $(1 - f^-)$  much smaller than unity, and, physically, since the charge neutrality condition can affect the concentration of *only* one of the charge carriers.

### 3. Application of the analytical derivation to a-Si:H

The central argument of Ref. [5] was that 'in reality' the 'curious situation' described above may account for the observation of a  $\lambda \neq 0$  in undoped a-Si:H. We will show now that this is very unlikely for a-Si:H, by using the very recombination parameters suggested in Ref. [5]. We note that these parameters are most favorable (within the range of known [8–10] a-Si:H parameters) for the 'curious situation' for a-Si:H.

In principle, the general 'curious situation' may occur under the special combination of the deep trapping times given by [5]:

$$\tau_n^0/\tau_p^0 \ll n_f/p_f \ll \tau_n^0/\tau_p^-, \quad (2)$$

where  $\tau_p^0$  is the deep trapping time of holes in the neutral dangling bonds. The right-hand inequality is already the case implied by Eq. (1) for the 'curious' case of  $f^- \ll 1 - f^-$ . As for the left-hand side inequality, it is commonly agreed that in a-Si:H,  $\tau_n^0/\tau_p^0 \approx 1$ . Hence, the particular way of writing [5] unity as  $\tau_n^0/\tau_p^0$  does not reflect the multilevel nature of the dangling bond but rather the a priori assumption that we have an n-type photoconductor ( $n_f > p_f$ ). Hence, the simple single acceptor level-like nature of the problem is *maintained*, in the 'curious situation'. Turning to the numerical evaluation of the right hand side inequality we note that  $\tau_n^0/\tau_p^-$  derived from the experimental data by Ref. [5] (and others [8–10]) is  $\tau_n^0/\tau_p^- = 100$ . This means (Eq. (2)) that the 'curious situation' should correspond to  $n_f/p_f \approx 10$ . Now, for the common  $G = 10^{19} \text{ cm}^{-3} \text{ s}^{-1}$  the authors of Ref. [5] find that the maximum value of  $p_f$  is smaller than  $4 \times 10^{11} \text{ cm}^{-3}$ . Accordingly,  $n_f$  must be smaller than  $10^{13} \text{ cm}^{-3}$ . Since  $N_{db}$  (as given in Refs. [5,8]) is larger than  $10^{16} \text{ cm}^{-3}$ , we obtain that  $N_{db}/n_f, N_{db}/p_f > 10^3$ .

Returning to the above analysis of  $\gamma$  and  $\lambda$  as given in Section 2, we remember, that in order for the charge neutrality condition to affect the carrier concentration (yielding  $\gamma \neq 1$  or  $\lambda \neq 0$ ) we must have that either  $n_f \approx (1 - f^-)N_{db}$  or  $p_f \approx f^- N_{db}$  (the 'curious situation'). In view of those requirements, we conclude from the above discussion that for a-Si:H,  $f^-/(1 - f^-) = 10^{-3}$ . Examining Eq. (1), we see that even if  $n_f = p_f$  (favorable conditions for the 'curious case') the  $\tau_n^0/\tau_p^- = 100$  will yield that  $f^-/(1 - f^-) \approx 10^{-2}$  rather than the above observed value of  $10^{-3}$ . We saw in Section 2 that as long as  $n_f < (1 - f^-)N_{db}$  or  $p_f < f^- N_{db}$ , the carrier concentrations do not affect the occupation of the recombination centers and the lifetime. Hence, *even* under the above very favorable parameters for the 'curious case', we get that  $\gamma = 1$  and  $\lambda = 0$  which in turn, explains why in the numerical simulations of the single type of dangling bonds model [2] one always finds the  $\lambda = 0$  result for all reasonable parameters of a-Si:H. The interpretation [5] of the  $\lambda$  variation as a transition between the 'normal' case of  $\lambda = 0$  to

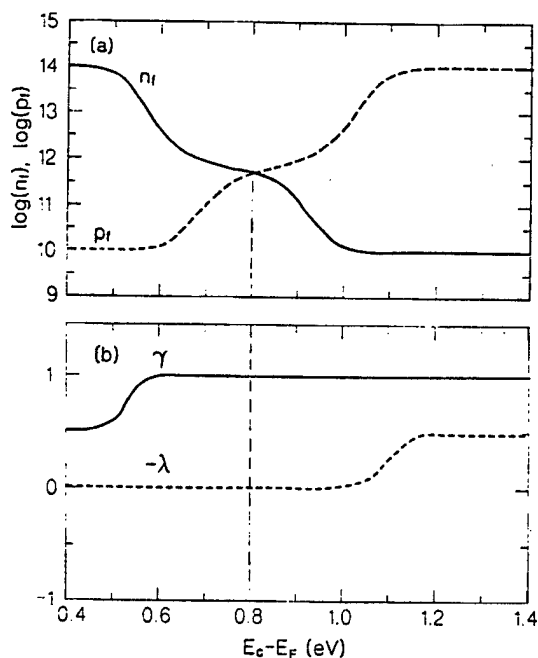


Fig. 1. The calculated optically excited free electron, and free hole concentrations (a), and their corresponding light intensity exponents (b), as a function of the Fermi level position, for the single type of dangling bonds model. Note that  $\gamma$  and  $\lambda$  are associated here with the electrons and holes, respectively. For the 'n-type' material ( $E_c - E_F \leq 0.8$  eV) these are majority and minority carriers, respectively.

the 'curious situation' of  $\lambda = 1/2$  is therefore unfounded in a-Si:H, and one must resort to a model that has at least one other type of recombination center in addition to the single level dangling bond centers.

To further illustrate the above point, we show in Fig. 1 the results of our own numerical computations of the  $E_c - E_F$  dependence of  $n_f$ ,  $p_f$ ,  $\gamma$  and  $\lambda$ , when the parameters mentioned above were utilized. The other parameters, less critical for the present work, were taken from Refs. [2,8] and the numerical calculations were done using the dangling bond statistics of Ref. [8]. We show these results in order to affirm the results of Morgado [2] as well as (unlike Morgado) to present them in terms of  $n_f$  and  $p_f$ . The 'n-type' cases discussed above are given in Fig. 1 for the interval of  $E_c - E_F \leq 0.8$  eV. For the larger  $E_c - E_F$  values the material is 'p-type' and the behavior is analogous to that of the 'n-type' material. It is clearly seen that for the 'n-type' range the decrease-

ing  $n_f/p_f$  ratio does not yield the 'curious situation' ( $\lambda \neq 0$ ) claimed in Ref. [5] and that a rather simple n-type to p-type transition [1] takes place. This  $\lambda = 0$  finding proves then that the 'curious situation' is not 'relevant' to a-Si:H and that a single type of dangling bonds cannot account for the experimental  $\lambda \neq 0$  observation in undoped a-Si:H.

#### 4. Discussion and conclusions

Following the results of Section 3, it is obvious that our test [1] of  $\lambda \neq 0$  is enough to establish the existence of states other than a single type of dangling bonds, but it is not enough for the determination of which of the more complex models is the correct one. On the other hand the dependence of  $\lambda$  on 'external' parameters, such as  $E_c - E_F$  or the temperature, can yield some new conclusions regarding the state distribution in a-Si:H. For example, we expect [9,10] that the role of the recombination in the bandtails diminishes with increasing temperature. According to our  $\lambda \neq 0$  test, we expect then that in this material we will find a  $\lambda \rightarrow 0$  behavior with increasing  $T$ . Indeed, we have experimentally found [11] this expected behavior. This finding yields then further support to the applicability of our test for a-Si:H. It also shows that this test can yield information that is otherwise obtained by comparison of the experimental results with detailed numerical computations [9,10].

#### Acknowledgements

This work was supported in part by the Enrique Berman Solar Energy Research Fund and in part by NSF EPSCoR Grant OSR No. 94-52893 and NASA grant No. NCCW-0088.

#### References

- [1] I. Balberg, J. Appl. Phys. 75 (1994) 914.
- [2] E. Morgado, J. Non-Cryst. Solids 164–166 (1993) 627.
- [3] I. Balberg, Y. Lubianiker, Phys. Rev. B 48 (1993) 8709.
- [4] G. Schumm, C.-D. Abel, G.H. Bauer, J. Non-Cryst. Solids 137–138 (1991) 351.

- [5] J. Hubin, A.V. Shah, E. Sauvain, P. Pipoz, *J. Appl. Phys.* 78 (1995) 6050.
- [6] A. Rose, *Concepts in Photoconductivity and Allied Problems*, Wiley-Interscience, New York, 1963.
- [7] R.S. Crandall, in: J.I. Pankove (Ed.), *Semiconductors and Semimetals*, Academic Press, New York, Vol. 21, Part C, 1986, p. 245.
- [8] F. Vaillant, D. Jousse, *Phys. Rev. B* 34 (1986) 4088.
- [9] M.Q. Tran, *Philos. Mag.* 72 (1995) 35.
- [10] R. Bruggemann, in: J.M. Marshal, N. Kirov (Eds.), *Photoconductive Properties in Future Directions. in Thin Film Science and Technology*, World Scientific, Singapore, 1997.
- [11] Y. Lubianiker, I. Balberg, L. Fonseca, S.Z. Weisz, *Mater. Res. Soc. Symp. Proc.*, 1997, in press.

## OPTICAL PROPERTIES AND NANOPARTICLE SIZE DISTRIBUTION IN LUMINESCENT POROUS SILICON

L.F. FONSECA, O. RESTO, S. GUPTA, R.S. KATTIYAR, AND S.Z. WEISZ

*Physics Dept., University of Puerto Rico, P.O. Box 23343, San Juan, PR, USA 00931*

Y. GOLDSTEIN, A. MANY, AND J. SHAPPIR

*The Hebrew University, Jerusalem 91904, Israel*

We measured the photoluminescence, optical transmission and Raman spectra of free standing, luminescent porous Si films of high optical quality. The optical transmission data were used to derive the size distribution of the nanoparticles in the porous Si films. The procedure is based on the assumption that interband transition is the principal mechanism for the absorption and that quantum confinement in the nanoparticles determines the optical gap. The distribution obtained is centered around 22 Angstroms and is not symmetric, exhibiting a tail towards larger sizes. On the basis of this distribution we predicted a shift of  $\sim 20 \text{ cm}^{-1}$  in the  $521 \text{ cm}^{-1}$  silicon line in the Raman spectrum. This shift was indeed observed in our samples, thus confirming the size distribution obtained from the optical data.

### 1 Introduction

It is generally accepted that quantum confinement plays a crucial role in the photoluminescence properties of porous silicon (PSi). The structure of the porous system depends on the preparation method but, in general, nanoscale-sized silicon crystallites are required to get visible luminescence. Extensive work has been done during the last seven years to characterize the PSi nanostructure and to correlate it with its optical, photoluminescence and electroluminescence properties. Raman analysis is an important tool to characterize Si nanostructures giving information about size and shape [1]. Raman studies of electrochemically etched PSi report spherical nanostructures in most of the cases [2-4]. Many of the size analyses using the Raman technique yield only the average size of the particles. The particles' size distribution,  $F(r)$ , is addressed only in an indirect way through the Fourier coefficients of the confined phonon wavefunctions [5].

In order to study the nanostructure characteristics of high porosity PSi samples, we measured two independent quantities, the optical transmission and the Raman spectrum. High optical quality, free-standing luminescent porous silicon was used. We derived  $F(r)$  from the optical transmission data and calculated the Raman spectrum associated with this distribution of particles. The calculated spectrum was compared with the measured Raman data.

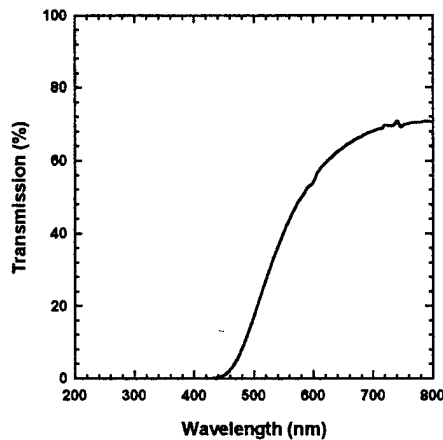


Figure 1. Transmission spectrum of the PSi film.

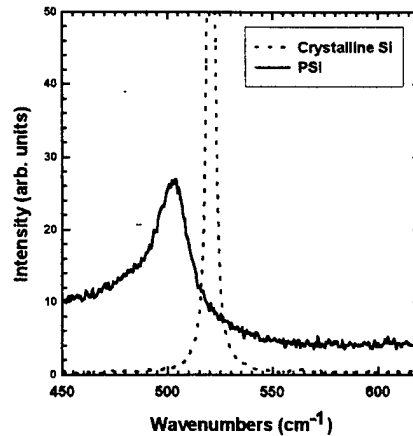


Figure 2. Raman spectra of the Si wafer and the PSi film.

## 2 Experiments and Calculations

PSi samples were prepared by electrochemical anodization of a p-type, 0.5-1.5  $\Omega\text{cm}$ , (100) silicon wafer using a HF:ethanol:water (1:2:1) solution. The anodization current (200 mA/cm<sup>2</sup>) was applied in 280 steps of 0.8 sec each and with resting intervals of 1.4 sec between anodizations, in order to ensure a high-optical quality film.

The optical transmission spectrum was measured by a Perkin Elmer Lambda 6 spectrometer. The results are shown in Fig. 1. The Raman spectra of the crystalline silicon wafer and of the free standing sample were taken by a ISA T64000 spectrometer. The results are plotted in Fig. 2. The peak of the spectrum of the crystalline Si is obtained at 521 cm<sup>-1</sup> as expected. The peak for the PSi sample occurs at 501 cm<sup>-1</sup>, a shift of 20 cm<sup>-1</sup>. The optical transmission spectrum of the sample was used as the starting point to calculate the size distribution of the silicon particles in the PSi sample. This calculation was done by assuming that the porous silicon sample is a collection of spherical crystallites whose sizes are described by a distribution function,  $F(r)$ , and also that the absorption is due to the interband transition of the electrons in the individual crystallites.

We assume that each particle is transparent for energies ( $E$ ) lesser than its optical gap ( $E_g$ ) and its absorbance increases abruptly for  $E > E_g$ , the transmission coefficient of a film can be expressed as,

$$T(\lambda) \propto 1 - C \int_0^{\infty} F(r) A(r, \lambda) dr$$



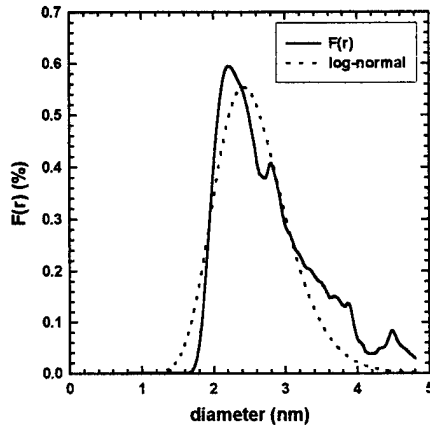
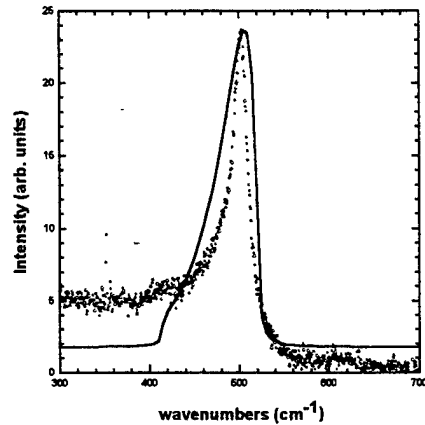
Figure 3. Calculated  $F(r)$  and log-normal fit.

Figure 4. Comparison between the observed Raman spectrum (dots) and the predicted one (solid line)

where  $C$  is a constant and  $A(r, \lambda)$  is proportional to the energy absorbed by a particle of radius  $r$ .  $A(r, \lambda)$  is approximated by the Heavyside step function,  $A(r, \lambda) \propto \Theta(\lambda_{g,r} - \lambda)$  where  $\lambda_{g,r} = 2\pi\hbar c / E_{g,r}$ , and  $E_{g,r}$  is the energy gap for particles of size  $r$ . From the above expression, we obtain that the first derivative of the transmission spectrum is proportional to the size distribution density,

$$\left. \frac{\partial T}{\partial \lambda} \right|_{\lambda_0} \propto - \int_0^{\infty} F(r) \delta(r - r_0) dr \propto -F(r_0)$$

where  $r_0$  is the size which gives an energy gap corresponding to  $\lambda_0$ .

Figure 3 shows the size distribution (solid line) obtained from the transmission spectrum (Fig.1) under the above considerations giving a non-symmetric size distribution peaking at 2.2 nm. To obtain this size distribution, we assumed a spherical particle shape [2-4] and used the relation between the magnitude of the energy gap and the size of the (spherical) particle suggested in reference [6],  $E_{g,r} = 1.1 + 3.65r^{-1.3}$  where  $E_{g,r}$  is in eV and  $r$  in nm.

Using the size distribution given in Fig.3, the Raman spectrum for the sample was calculated as

$$I_{\text{predicted}}(\omega) = \int_0^{\infty} F(r) I_{\omega}(r) dr$$

where  $I_{\omega}(r)$  is obtained from the phonon-confinement model [1, 4].

Figure 4 shows a comparison between the calculated Raman intensity and the experimental data. We notice that the calculation reproduces accurately the peak position but is somewhat wider than the experimental curve.

### 3 Conclusions

Two independent measurements, optical transmission and Raman spectrum, were used to determine the size distribution,  $F(r)$ , in highly porous luminescent PSi films.  $F(r)$  obtained from the transmission spectrum peaks at 2.2 nm and agrees with the Raman observation assuming that the PSi film is composed of spherical particles rather than wires. A wire-like nanostructures would yield a size distribution peaking at smaller sizes and thus would predict a Raman shift larger than the observed 20  $\text{cm}^{-1}$ . This provides support to the assumption that PSi films of high porosity are composed of particles nearly spherical in shape. The width of the Raman peak, as predicted from  $F(r)$ , is larger than the observed one. Probably because the size distribution was obtained assuming an abrupt increase of the optical absorption at the gap energy of each nanoparticle. This simplification can be improved by the addition of a parabolic dependence on energy of the absorption coefficient of the nanoparticles. Such a dependence would reduce the width of  $F(r)$ .

### 4 Acknowledgment

This work was supported by US ARO No. DAAHO4-96-1-0405, NSF EPSCoR OSR No. 94-52893, NASA No. NCCW-0088 and by Ministry of Science and Arts, Israel, within the framework of the infrastructure-applied physics support project.

### 5 References

1. Campbell I.H. and Fauchet P.M., The effects of microcrystal size and shape on the one phonon Raman spectra of crystalline semiconductors, *Solid State Comm.* **58** (1986) pp. 739-741.
2. Sui Z., Leong P.P., Herman I.P., Higashi G.S., and Temkin H., Raman analysis of light-emitting porous silicon, *Appl. Phys. Lett.* **60** (1992) pp.2086-2088.
3. Munder H., Andrzejak C., Berger M.G., Klemradt U., Luth H., Herino R., and Ligeon L., A detailed Raman study of porous silicon, *Thin Solid Films* **221** (1992) pp.27-33.
4. Kanemitsu Y., Uto H., Masumoto Y., Matsumoto T., Fugati T., and Mimura H., Microstructure and optical properties of free-standing porous silicon films: Size dependence of absorption spectra in Si nanometer-sized crystallites, *Phys. Rev. B* **48** (1993) pp.2827-2830.
5. Brunetto N., Amato G., A new line shape analysis of Raman emission in porous silicon, *Thin Solid Films* **297** (1997) pp. 122-124.
6. Delerue C., Lannoo M., and Allan G., Theory of the luminescence of porous silicon, *J. Luminescence* **57** (1993) pp. 249-256.

## A new analysis method to characterize the S-band luminescence decay of porous Si

Jiaqi Yu<sup>1a</sup>, Huimin Liu<sup>a</sup>, Yanyun Wang<sup>a</sup>, Weiyi Jia<sup>a,\*</sup>, Luis F. Fonseca<sup>b</sup>,  
S.Z. Weisz<sup>b</sup>, Oscar Resto<sup>b</sup>

<sup>a</sup>Department of Physics, University of Puerto Rico, Mayaguez, PR 00681-9016, Puerto Rico

<sup>b</sup>Department of Physics and Materials Research Center, University of Puerto Rico, Rio Piedras, PR 00931, Puerto Rico

Received 1 April 1998; received in revised form 9 July 1998; accepted 28 August 1998

### Abstract

Analysis of the non-exponential luminescence decay and extraction of additional physical information from it are important issues for the spectroscopic study of porous Si. In this work a new approach to extract the decay time distribution function is proposed, based on the fact that the non-exponential luminescence decay of porous Si is a multiple exponential. It was found that the integrated intensities of different exponential components could be fitted by a Gaussian distribution function, characterized by  $\tau_0$ , the decay time with maximum probability, and  $d$ , the width of the Gaussian distribution function. The parameters  $\tau_0$  and  $d$  were found to vary with emission wavelengths.  $\tau_0$  decreases exponentially with an increase of the emission energy and  $d$  has a smaller value in the middle of the emission wavelengths. © 1999 Elsevier Science B.V. All rights reserved.

**Keywords:** Porous Si; S-band luminescence decay

### 1. Introduction

Porous Si has become increasingly attractive since its efficient visible luminescence at room temperature was reported in 1990 [1,22]. The S-band emission (400–800 nm, slow decay) has been studied extensively because of its great potential for applications [1,22]. Much attention has been paid to the study of the temporal behavior of the luminescence, since it is important for understand-

ing the nature of the luminescence mechanism. The luminescence decay of porous Si was found to exhibit a complicated non-exponential behavior. The characterization of the luminescence decay and extraction of physical information from it have been discussed extensively in the literature. Xie has defined the decay time as the time when the luminescence intensity has fallen by a factor of  $e$  [2]. However, the fast components characterized by this decay time may not dominate the multi-exponential decay. Vial has defined an “average lifetime” as the integral of the intensity with respect to time, divided by the initial luminescence intensity [3]. But a single parameter cannot fully characterize a non-exponential decay behavior. A number of workers have analyzed the form of the luminescence decay by fitting a stretched exponential or by

\*Corresponding author. Tel.: 1 787 832 4040; fax: 1 787 832 1135; e-mail: wjia@rumac.upr.clu.edu.

<sup>1</sup>On leave from Laboratory of Excited State Processes, Changchun Institute of Physics, Chinese Academy of Sciences, Changchun 130021, People's Republic of China.

extracting lifetime distributions from the multi-exponential decays [4–10]. However, a deviation of the decay curves from the stretched exponential was observed in the longer time region at low temperature [9]. Some of the proposed lifetime distribution functions seem difficult to understand with clear physical pictures.

In this work, a new method to derive the decay time distribution function is introduced to analyze the luminescence data of our porous Si samples, assuming a decay time distribution originating from isolated (or confined) multiple optical centers in a random system. It is found that the integrated intensities of different exponential components can be fitted by a Gaussian distribution function, which was characterized by  $\tau_0$ , the decay time of the component with maximum probability, and  $d$ , the width of the Gaussian function.  $\tau_0$  and  $d$  for different emission wavelengths were obtained through the fitting procedure.  $\tau_0$  was found to decrease exponentially with an increase of the emission energy and the smallest  $d$  (the narrowest distribution) was found to be at the middle wavelength region of the emission.

## 2. Samples and experiments

The samples were prepared by the conventional electrochemical anodization method [11,12,23]. The electrolytic solution for the anodic etching was 1:2:1 (HF: ethanol: water). The cell included a standard Platinum electrode as the cathode and a Boron-doped crystalline silicon wafer with a resistivity in the range 0.5–1.5  $\Omega$  cm as the anode. The aluminum ohmic contact at the bottom of the wafer was made by sputtering deposition and annealing. Previous to the anodization, the silicon surface of the wafer was cleaned with 20% HF-aqueous solution for 5 min. Samples were anodized with a current density of 100 mA/cm<sup>2</sup> for 600 s and finally dried using the critical point method [13].

A Nd:YAG laser with a pulse width of 35 ps and an optical parametric generator were employed as a tunable pulse excitation source. A double Spex 1403 spectrometer was used to analyze luminescence signals. Time-resolved emission spectra were measured using a SR250 boxcar averager with time

resolution of 0.05  $\mu$ s. Luminescence decay was measured by a SR430 multi-channel transient scaler. The temperature of the samples was controlled by a helium-close-cycle refrigerator from 10 K to room temperature.

## 3. Experimental results and discussion

Luminescence decay curves of different wavelengths at 11 K and time-resolved emission spectra at room temperature were measured under excitation with 532 nm laser pulses. Typical results are shown in Figs. 1 and 2, respectively, and are similar to those reported in literature [2–10]. The decay curves are not exponential. In Table 1, the values of  $\tau_0$  and  $\tau_e$  are listed for different emission wavelengths.  $\tau_e$  is the time when the fluorescence intensity falls to 1/e of the initial value.  $\tau_0$  is the decay time of the component with maximum probability, derived using the new approach introduced

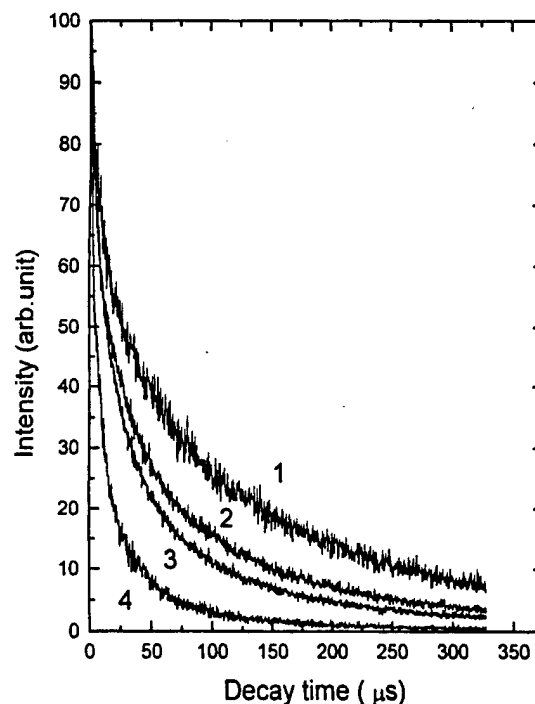


Fig. 1. Luminescence decay of different wavelengths under excitation with 532 nm at 11 K. (1) 700 nm; (2) 640 nm; (3) 600 nm; (4) 540 nm.

in this work. The luminescence decay becomes slower at longer emission wavelengths.  $\tau_0$  increases from 30.8  $\mu\text{s}$  at 540 nm to 432.6  $\mu\text{s}$  at 750 nm.

It is generally believed that the blue-shifted visible emission from porous Si samples is the result of quantum confinement [1–3,14,15]. Structure studies revealed that porous Si has a wire-like microstructure with wire-width randomly distributed

[14,15]. Electrons participating in the visible luminescence are those excited in those highly confined regions.

For the time-resolved emission spectra, the peak position shifts from 640 to 690 nm with an increase of the delay time. The band width was found to have no significant broadening with increasing temperature from 10 to 300 K. All the results imply that the emission spectra are inhomogeneously broadened and are an overlap of the emission bands from different confined regions, each having an exponential decay with its own characteristic decay time.

The questions raised are how the exponential components distribute (intensity versus lifetime) and which component dominates.

It is assumed that, due to strong quantum confinement, the excited electron-hole pairs are localized and spatial energy transfer is negligible. The emission of each confined region has an exponential decay. The measured luminescence decay at certain wavelength can then be expressed as

$$I = \sum_i I_i \exp(-\tau_i^{-1}t) = \sum_j \frac{Q_i}{\tau_i} \exp(-\tau_i^{-1}t), \quad (1)$$

where  $Q_i = I_i\tau_i$ , it is the integrated intensity of  $i$ th exponential component. After careful study of the decomposition of decay curves of different emission wavelengths, it was found that  $Q_i = I_i\tau_i$  can be fitted by a Gaussian function of  $\ln \tau_i$ .

$$Q_i(\tau_i) = A \cdot \exp(-4 \ln 2 ((\ln \tau_i - \ln \tau_0)/d)^2), \quad (2)$$

where  $\tau_0$  and  $d$  are the fitting parameters,  $\tau_0$  is the decay time of the exponential component which has maximum distribution probability,  $d$  is the full-width at the half-height and  $A$  is a constant

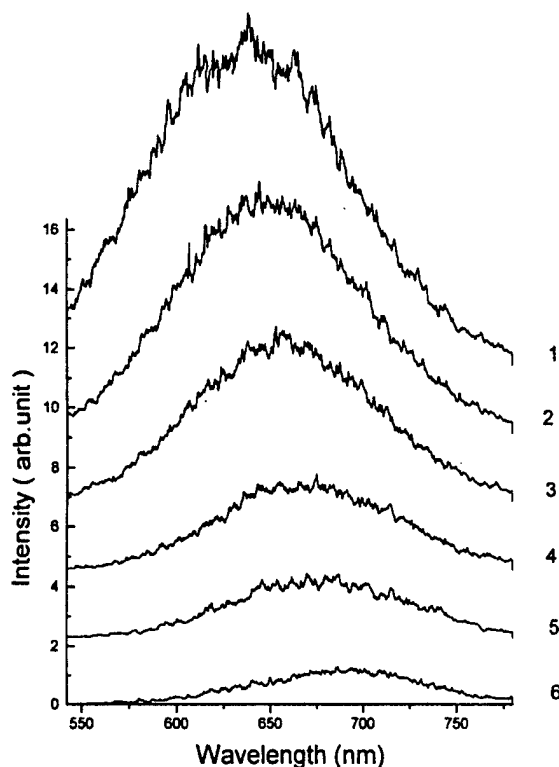


Fig. 2. Time-resolved emission spectra of a porous Si sample at room temperature, excited at 532 nm. (1) 4  $\mu\text{s}$ ; (2) 14  $\mu\text{s}$ ; (3) 24  $\mu\text{s}$ ; (4) 44  $\mu\text{s}$ ; (5) 64  $\mu\text{s}$ ; (6) 84  $\mu\text{s}$ .

Table 1

Fitting parameters  $\tau_0$  and  $d$  of a sample for different emission wavelengths. Excitation at 532 nm at 11 K.

$\lambda$ (nm)	540	565	600	630	660	720	750
$\tau_0(\mu\text{s})$	30.8	48.4	80.0	117.7	162.7	278.0	432.6
	$\pm 0.8$	$\pm 1.2$	$\pm 2.0$	$\pm 2.9$	$\pm 4.1$	$\pm 7.0$	$\pm 10.8$
$d$	2.78	2.61	2.41	2.15	2.09	2.60	2.96
	$\pm 0.07$	$\pm 0.07$	$\pm 0.06$	$\pm 0.05$	$\pm 0.05$	$\pm 0.07$	$\pm 0.07$
$\tau_e(\mu\text{s})$	9.4	18.2	33.6	58.2	82.2	102.5	116.7
	$\pm 0.1$	$\pm 0.2$	$\pm 0.3$	$\pm 0.6$	$\pm 0.8$	$\pm 1.0$	$\pm 1.2$

determined by the initial intensity of the fitted decay curve.

The Gaussian distribution function (2) was used to fit the decay curves of different emission wavelengths at different temperatures. All decay curves were fitted quite well.

The following equation was used for routine fitting procedure:

$$\begin{aligned}
 I(t) &= A \sum_{i=-m}^m \frac{1}{\tau_i} \exp \left( -4 \ln 2 \left( \frac{\ln \tau_i - \ln \tau_0}{d} \right)^2 \right) \\
 &\quad \times \exp \left( -\frac{t}{\tau_i} \right) \\
 &= A \sum_{i=-m}^m \frac{1}{(\tau_0 n^i)} \exp \left( -4 \ln 2 \right. \\
 &\quad \times \left. \left( \frac{\ln(n^i \tau_0) - \ln \tau_0}{d} \right)^2 \right) \exp \left( -\frac{t}{\tau_0 n^i} \right), \quad (3)
 \end{aligned}$$

where  $\tau_i = n^i \tau_0$ . The parameter  $A$  can be determined by the initial intensity  $I(0)$

$$A = I(0) \tau_0 / \sum_{i=-m}^m n^{-i} \exp \left( -4 \ln 2 \left( \frac{\ln(n^i)}{d} \right)^2 \right). \quad (4)$$

Therefore,

$$\begin{aligned}
 I(t) &= I(0) \left[ \sum_{i=-m}^m n^{-i} \ln \left( -4 \ln 2 \left( \frac{i \ln n}{d} \right)^2 \right) \right. \\
 &\quad \times \exp \left( -\frac{t}{\tau_0 n^i} \right) \left. \right] / \left[ \sum_{i=-m}^m n^{-i} \right. \\
 &\quad \times \exp \left( -4 \ln 2 \left( \frac{i \ln n}{d} \right)^2 \right) \left. \right]. \quad (5)
 \end{aligned}$$

The number of terms in the sum is  $2m + 1$ .  $m$ , as an appropriate integer number, is chosen to be 3 or larger. The ratio  $n$  will be automatically optimized during the fitting procedure. Two fitting parameters  $\tau_0$  and  $d$  in Eq. (5) can be easily obtained by a simple fitting program. The fitting parameters are not sensitive to the initialization values. There are a unique set of fitting parameters for a given decay curve. User's function in Microcal Origin was used in this work as a routine fitting procedure to analyze the decay curves of the porous Si samples. As an example, the fitting of the decay curve and the distribution  $Q_i$  versus  $\ln \tau_i$  with  $m = 3$  for the 660 nm emission at 290 K are shown in Fig. 3a, b,

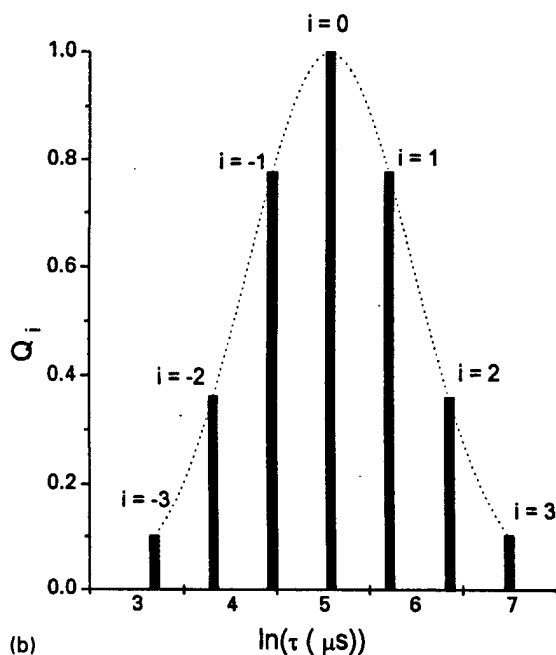
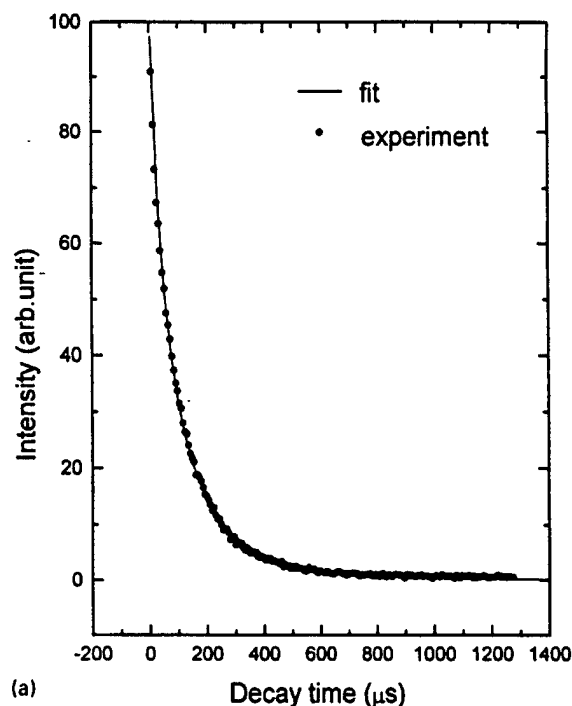


Fig. 3. (a) A decay curve fitted by a multi-exponential function. (b)  $Q_i$  versus  $\ln \tau$  of the fitting function.

respectively. Only a small number of the experimental points in Fig. 3a were used for clarity.

The suitability of the fitting function was checked using data published by other authors. For example, Ookubo found that decay curves of their samples fit a stretched exponential function at temperatures above 20 K, and deviated in the long time region at 20 K [9]. We reproduced some of their data from the parameters in the paper and fit decay curves for  $T \geq 20$  K satisfactorily in whole time region with our fitting function.

The fitting parameters  $\tau_0$  and  $d$  of a sample for different emission wavelengths at 11 K are listed in Table 1. Values of  $\tau_c$  were included in the table for comparison. The decay time  $\tau_0$  increases with an increase of the emission wavelength and varies from 30.75  $\mu\text{s}$  for 540 nm to 432.6  $\mu\text{s}$  for 750 nm. The values of  $\tau_0$  and  $\tau_c$  are quite different. The width  $d$  of the Gaussian distribution is smaller near the center of the emission band and larger at the extreme wavelengths. For 660 nm,  $d = 2.09$ , and the ratio of the decay time of the half height at the longer side to that of the shorter side was found to be about 8, while at 750 nm the width  $d$  is 2.96 and the ratio is about 19. The decay time distribution functions  $Q$  against  $\ln \tau$  for different emission wavelengths are shown in Fig. 4a. Redrawing the distribution functions  $Q$  in the abscissa of  $\tau$  as shown in Fig. 4b, it is clearly seen that  $Q$  has a long tail in the longer decay side. This is similar to what was expected for disordered systems as discussed by Scher and others [16].

It is interesting to note that  $\tau_0$  and the emission photon energy  $w$  satisfy the following exponential relation:

$$\tau_0 = \tau_c \exp(-w/w_c), \quad (6)$$

where  $\tau_c$  and  $w_c$  are constants. A typical result for the emission of a sample excited at 532 nm and 11 K is shown in Fig. 5 with the fitting parameters  $\tau_c = 2.77 \times 10^5 \mu\text{s}$  and  $w_c = 0.25$  eV.  $\tau_c$  is also plotted in the figure for comparison.

The decrease in the decay time with increasing emission energy has been ascribed to the increases of the oscillator strength of the radiative transition at the high-energy side resulting from stronger quantum confinement [17–19]. It was found that

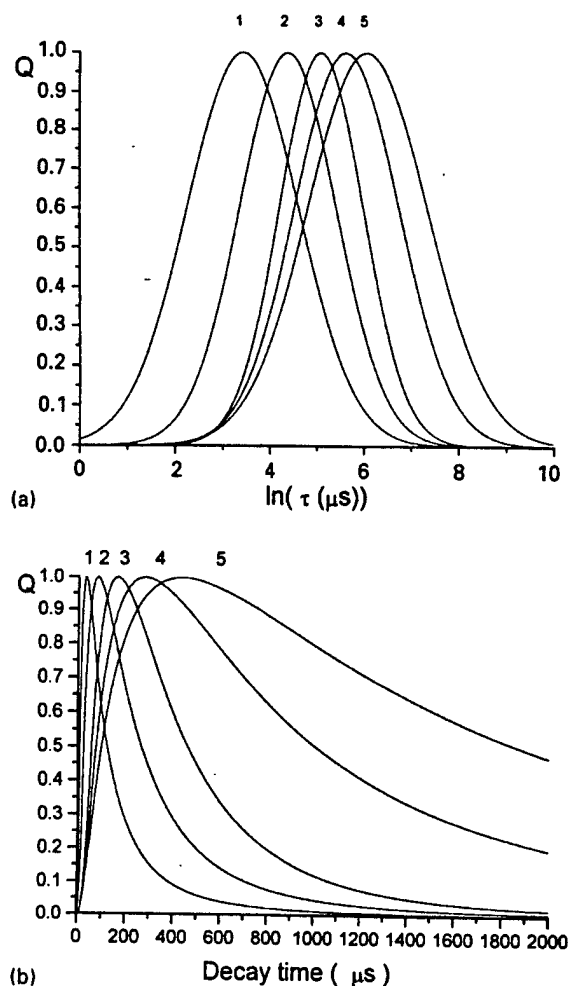


Fig. 4. The Gaussian distribution function of decay times for different emission wavelengths excited at 532 nm at 11 K, plotted in (a) vs.  $\ln \tau$  and in (b) versus  $\tau$  (1) 540 nm; (2) 600 nm; (3) 660 nm; (4) 720 nm; (5) 750 nm.

the Si conduction band edge shifted to higher energy and the oscillator strength of the radiative transitions increased with a decrease of particle sizes [20,21]. The variation of the decay time with temperature in the high-temperature region has been reported by Vial et al. [3]. They found that the decay rate increased exponentially with the luminescence energy up-shift. This observation is consistent with our result described by Eq. (6).

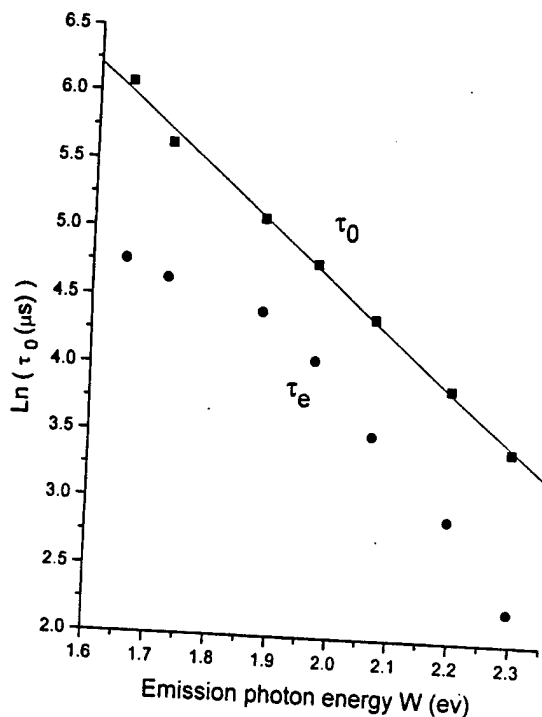


Fig. 5.  $\ln \tau_0$  versus emission energy  $w$ , under excitation at 532 nm at 11 K.

#### 4. Summary

A new method to analyze the multi-exponential decay of fluorescence of porous Si is proposed. It was found that the integrated intensities of different exponential components could be fit by Gaussian distribution functions which were characterized by  $\tau_0$ , the decay time with maximum probability, and  $d$ , the width of the Gaussian function. The decay time  $\tau_0$  was found to decrease exponentially with an increase of the emission energy and the distribution width  $d$  had a smaller value at the middle wavelength of the emission. The parameters  $\tau_0$  and  $d$  introduced in this work might be useful to characterize multiple exponential decay for system with random isolated optical centers, each of which have an exponential decay.

#### Acknowledgements

This work was supported by NSF-EPSCoR, US ARO-DAAH04-96, US. DOE and NASA-MURC (NCCW-00088).

#### References

- [1] L.T. Canham, *Appl. Phys. Lett.* 57 (1990) 1046.
- [2] Y.H. Xie, W.L. Wilson, F.M. Ross, J.A. Mucha, E.A. Fitzgerald, J.M. Macauley, T.D. Harris, *J. Appl. Phys.* 71 (1992) 2403.
- [3] J.C. Vial, A. Bsiesy, F. Gaspard, R. Herino, M. Ligeon, F. Muller, R. Romestain, R.M. Macfarlane, *Phys. Rev. B* 45 (1992) 14171.
- [4] X. Chen, B. Henderson, K.P. O'Donnell, *Appl. Phys. Lett.* 60 (1992) 2672.
- [5] N. Ookubo, H. Ono, Y. Mochizuki, S. Matsui, *Appl. Phys. Lett.* 61 (1992) 940.
- [6] Lorenzo Pavesi, Matteo Ceschini, *Phys. Rev.* 48 (1993) 17625.
- [7] Yoshihiko Kanemitsu, *Phys. Rev.* 48 (1993) 12357.
- [8] G. Mauckner, K. Thonke, T. Baier, T. Walter, R. Sauer, *J. Appl. Phys.* 75 (1994) 4167.
- [9] N. Ookubo, S. Sawada, *Phys. Rev.* 51 (1995) 17526.
- [10] Hideki Koyama, Ysuyoshi Ozaki, Nobuyoshi Koshida, *Phys. Rev.* 52 (1995) 11561.
- [11] F. Koch, *Mat. Res. Soc. Symp. Proc.* 298 (1993) 319.
- [12] G. Morell, R. Katiyar, M. Gomez, S.Z. Weisz, I. Balberg, *Mat. Res. Soc. Symp. Proc.* 297 (1993) 321.
- [13] J. Von Benren, P.M. Fauchet, E.H. Chimowitz, C.T. Lira, *Mat. Res. Soc. Symp. Proc.* Fall 96.
- [14] A.G. Cullis, L.T. Canham, P.D.J. Calcott, *J. Appl. Phys.* 82 (1997) 909.
- [15] H. Koyama, N. Koshida, *Phys. Rev. B* 52 (1995) 2649.
- [16] H. Scher, M.F. Shlesinger, J.T. Bendler, *Physics Today* 41 (1991) 26.
- [17] A. Bsiesy, J.C. Vial, F. Gaspard, R. Herino, M. Ligeon, F. Muller, R. Romestain, A. Wasiela, A. Halimaoui, G. Bomchil, *Surf. Sci.* 254 (1991) 195.
- [18] G.D. Sanders, Y.C. Chang, *Phys. Rev. B* 45 (1992) 9202.
- [19] M.S. Hybertsen, *Phys. Rev. Lett.* 72 (1994) 1514.
- [20] P.E. Batson, J.R. Heath, *Phys. Rev. Lett.* 71 (1993) 911.
- [21] C. Delerue, M. Lannoo, G. Allan, *J. Lumin.* 57 (1993) 249.
- [22] L.T. Canham, *Phys. Stat. Sol. B* 190 (1995) 9.
- [23] M.S. Brandt, H.D. Fuchs, M. Stutzman, J. Weber, M. Cardona, *Solid State Commun.* 81 (1992) 307.



## TWO CARRIER SENSITIZATION AS A SPECTROSCOPIC TOOL FOR a-Si:H

L.F. FONSECA\*, S.Z. WEISZ\*, R. RAPAPORT\*\* AND I. BALBERG\*\*

\*Department of Physics, University of Puerto Rico San Juan 00931, PR

\*\*The Racah Institute of Physics, The Hebrew University, Jerusalem 91904, Israel

### ABSTRACT

In a recent letter we have reported the first observation of the phenomenon of minority carrier-lifetime sensitization in hydrogenated amorphous silicon (a-Si:H). We find now that combining the study of this phenomenon with the study of the well-known phenomenon of majority carrier lifetime sensitization, in this material, can provide direct information on its density of states (DOS) distribution. This finding is important in view of the limitations associated with other methods designed for the same purpose. We have carried out then an experimental study of the effect of light soaking on the phototransport in a-Si:H. We found that the increase of the dangling bond concentration with light soaking affects the sensitization and thermal quenching of the majority carriers lifetime. Using computer simulations, we further show that the details of the observations associated with the sensitization effect yield semiquantitative information on the concentration and character of the recombination centers in a-Si:H.

### INTRODUCTION

The phenomenon of thermal quenching of the photoconductivity in intrinsic a-Si:H is known for many years [1]. The interpretation of this phenomenon is two-fold. First, it requires that the capture coefficients of the electrons is much smaller for the bandtail states (BTS) than for the dangling bonds (DB), and second, it requires that with increasing temperature (T) the number of BTS available for recombination,  $P_v$ , decreases until at some T it equals the concentration of the dangling bonds  $N_D$ . While this basic picture is in accord with the results of numerical simulations [2,3], we do not know of a direct experimental proof that establishes this model and that ties this phenomenon with the phenomenon of sensitization. The latter phenomenon is that the addition of excess recombination centers can prolong the lifetime of the charge carriers in a given photoconductor [4]. In this paper we study this effect by applying the tool of light soaking (LS) in order to change the concentration of desensitizing recombination centers in a-Si:H. We do that here in the "reverse mode" to the one used classically [4], i.e. by keeping the total concentration of the sensitizing centers nearly constant and changing the concentration of the desensitizing recombination centers.

After establishing experimentally the above basic picture of the sensitization, we have turned to numerical simulations that enabled us to evaluate the relation between the manifestations of the phenomenon of the sensitization and various parameters of the concentration and capture coefficients of the recombination centers in the mobility gap of a-Si:H. As we show below, these features give further semiquantitative spectroscopic information on the concentration and character of the recombination centers in the material.

## EXPERIMENTAL STUDIES

The samples used in the present experimental study were device quality a-Si:H films which were deposited [5] on a Corning 7059 glass and had a thickness of  $1.3\mu\text{m}$ . The temperature of the substrate at deposition was  $250^\circ\text{C}$ . Two planar contacts of NiCr were predeposited on the substrate in a configuration that we have described previously [6]. The photoconductivity  $\sigma_{\text{ph}}$  was measured as a function of the (HeNe laser) illumination intensity and  $T$ , in the  $T$  range of  $80 \leq T \leq 300\text{K}$ . The latter yielded a carrier generation rate,  $G$ , of  $5 \times 10^{18} \leq G \leq 5 \times 10^{20} \text{cm}^{-3}\text{s}^{-1}$ . The value of the mobility-lifetime product  $(\mu\tau)_e$  of the electrons (the majority carriers) was derived from the relation  $(\mu\tau)_e = \sigma_{\text{ph}}/qG$  where  $q$  is the electronic charge. It was thus implicitly assumed that the carrier generation quantum efficiency is unity and the absorption of the light is uniform. To find the light intensity exponent,  $\gamma_e$ , at a given  $T$ , the best fit of the data to a linear relation between  $\log \sigma_{\text{ph}}$  and  $\log G$  has been used. The importance of the value of  $\gamma_e$  is, as will be discussed below, that it reflects semiquantitatively some basic features of the recombination centers [4]. In particular, when  $\gamma_e > 1$ , the  $T$  dependence of  $\gamma_e$  yields information on their energy position, their concentration and their capture coefficient. In the present study we have measured the  $T$  dependence of  $(\mu\tau)_e$  and  $\gamma_e$ , before and after LS of the a-Si:H film. This was done in order to find out what spectroscopic information can be derived from these dependences. In the present study the light soaking was carried out under a HeNe illumination of  $100 \text{ mW/cm}^2$  for 10 hours.

The results of our measurements are presented in Fig. 1. In this figure we show the  $T$  dependence of  $(\mu\tau)_e$  before and after LS. It is clearly seen that before LS there is a clear change in the sign of the slope of the  $\sigma_{\text{ph}}(T)$  dependence around  $150^\circ\text{K}$ . We call the temperature of this change the  $T$  of thermal quenching,  $T_{\text{tq}}$ . After LS the  $(\mu\tau)_e$  drops, as expected, and the  $T_{\text{tq}}$  shifts to a somewhat lower  $T$ . This is in agreement with previous experimental results and numerical simulations [2] of the effect of the increase of the DB concentration on the  $(\mu\tau)_e$  dependence on  $T$ . The sensitization, as mentioned above, is manifested by a  $\gamma_e > 1$  value [4]. In the present case we find that, by comparison of the above behavior with the  $\gamma_e(T)$  dependence given in the inset of Fig. 1, the sensitization and the thermal quenching are two aspects of the same phenomenon. This is since we see that there is a clear downward shift in the  $\gamma_e(T)$  peak as well as a decrease in its amplitude around  $T_{\text{tq}}$  with the increase of LS.

The above features of the  $(\mu\tau)_e$  and  $\gamma_e$  dependences on  $T$  are simply explained along the lines of the

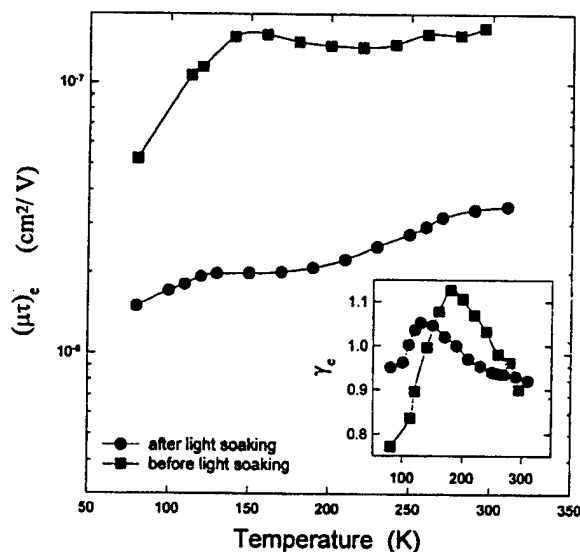


Figure 1. The measured  $T$  dependence of the mobility-lifetime product and the corresponding light intensity exponent for a typical sample of intrinsic a-Si:H.

general Rose model [4] as follows. The fact that the  $(\mu\tau)_e$  values, before LS, are much closer to each other at low T indicates that the recombination is not dominated there by the recombination centers that are induced by the LS. This is in contrast with the situation at the higher T. Following the well-known observation that LS increases the concentration of the dangling bonds  $N_D$  but does not cause an increase in the concentration of the valence band tail (VBT) states [7,8] it is expected that the latter states are responsible for the recombination at low temperatures. It thus appears that at the higher T the recombination is controlled by the dangling bonds (DB), while at the lower T it is controlled by the VBT states. We consider the VBT states rather than the conduction band tail (CBT) states since the lowering of T causes the shift of the quasi-Fermi level for holes towards the valence band edge thus increasing the concentration of centers available for electron recombination. The analysis of the above data in view of the classical picture of sensitization suggests then that as T is lowered there is a sensitization of the DB states by the VBT states, and that around  $T_{iq}$  the conditions for sensitization [4] are fulfilled. As (following the LS) there are more desensitizing DB the conditions for sensitization require more sensitization centers i.e., in our case, the decrease of T. In all of this we must assume that the electron capture coefficient of the BT states is considerably smaller than that of all relevant (known as the  $D^0$  and  $D^+$ ) DB. Hence, all the above results are consistent with our suggested explanation of the  $T_{iq}$  and with the observed  $\gamma_e > 1$  values. The question arises then whether the data shown in Fig. 1 can yield information beyond the above general picture. To consider this question we will discuss, in the next section, the T dependence of  $\gamma_e$ . This dependence is used since, as can be appreciated from Fig. 1,  $\gamma_e(T)$  has more conspicuous features than the  $(\mu\tau)_e$  dependence. For example, as far as we know the shape of  $\gamma_e$  has not been considered before. We will find out then the significance of the features in the of  $\gamma_e(T)$  dependence by using numerical simulations.

## NUMERICAL SIMULATIONS

Let us start by establishing the basic sensitization and thermal quenching picture described above. In Fig. 2(a) we show the T dependence of  $(\mu\tau)_e$  for the standard model of a-Si:H with parameters similar [9,10] to those used previously by Tran [2], in his "B1" model, but with four values of  $N_D$ . For the highest  $N_D$ , we have, below room temperature (RT), almost a T independent  $(\mu\tau)_e$ , while for the lowest  $N_D$  we have a strongly dependent  $(\mu\tau)_e$ . (The behavior above RT has to do with the thermal excitation of the carriers and will be discussed elsewhere). The above results can be simply interpreted by the fact that the quasi-Fermi levels for electrons and holes  $E_{Fn}$  and  $E_{Fp}$  embrace all the DB levels in the entire T range so that the concentration of DB centers available for electrons recombination,  $N_D'$ , does not change in the T range under study. In contrast, the concentration of the VBT states available for electron recombination,  $P_v(T)$ , is sensitive to the shift of  $E_{Fp}$  because of its "movement" through the exponential distribution of the density of states (DOS) in this tail. Hence, when we eliminate the DB (smallest  $N_D$ ) we get (considering the power-law T-dependence of  $P_v(T)$  in an exponential tail [4]) that the recombination is dominated by  $P_v(T)$ . This interpretation leads naturally to the expected behavior of  $(\mu\tau)_e$  for the intermediate values of  $N_D$ . For these values there is a T ( $\approx T_{iq}$ ) below which the recombination via the available DB states  $N_D' C_{Dn}$  equals the recombination via the VBT states  $P_v' C_{vn}$ . Here  $N_D'$  is the concentration of "hole" occupied DB,  $C_{Dn}$  is their capture coefficient,  $P_v'(T)$  is the available concentration of holes in the VBT states and  $C_{vn}$  is their capture coefficient. When T is lowered so that  $P_v' C_{vn} > N_D' C_{Dn}$  the sensitization is completed. The latter is of course true only if  $C_{vn} \ll C_{Dn}$  as discussed by Rose [4]. Correspondingly, we expect the transition from a recombination via the DB to a recombination via the VBT yielding

the effect of the thermal quenching, as is clearly confirmed by the numerical results seen for the intermediate  $N_D$  values. We further see that  $T_{iq}$  shifts towards low  $T$  with increasing  $N_D$ . Again, this is in complete agreement with the above picture since the above condition will be fulfilled then for larger  $P_v(T)$  values, i.e. at lower  $T$ . Hence, the above picture is consistent with both the experimental results and the numerical simulations.

All the above becomes even much more conspicuous when we consider the  $T$  dependence of  $\gamma_e$ . This dependence is shown in Fig. 2(b). When there is no thermal quenching the  $\gamma_e$  values are smaller than unity while when thermal quenching is present a very distinct peak with a  $\gamma_e > 1$  value is observed around  $T_{iq}$ . This is the well-known manifestation of the sensitization effect [4]. The clear shift of the position of the  $\gamma_e$  peak with increasing  $N_D$  to a lower  $T$ , as in Fig. 1 establishes the association of this effect with the thermal quenching. We further see that with the increase of  $N_D$  the value of  $\gamma_e$  decreases and its width, at its peak, increases. Again, this is consistent with the experimental observation shown in Fig. 1, and the above interpretation, since a "wider" section of the VBT (and thus a wider  $T$ -range) is required in order to dominate the recombination process. Hence, the basic picture described in the context of Fig. 1 is confirmed by the simulations. On the other hand, the details of the  $T$  dependences of  $(\mu\tau)_e$  and  $\gamma_e$  can convey many more details regarding the recombination centers in a-Si:H. In the present case the lower and wider the  $\gamma_e(T)$  peak the larger the ratio between  $N_D$  and the concentration of the VBT states. In the rest of this section we will derive such semiquantitative information from the  $\gamma_e(T)$  dependences around  $T_{iq}$  showing that one can follow the changes in the electronic structure in a series of samples by just measuring the above easily measured phototransport properties.

Our first check was then to find out the behavior, when the bandtails are eliminated, in order to evaluate the role of the bantails. We see in Fig. 3 that this elimination causes the absence of sensitization and that above about  $RT$   $\gamma_e(T)$  is determined by the thermal excitation of carriers from the DB. The fact that we have found a similar result in the presence of the CBT without the presence of the VBT establishes the conclusion discussed above that the VBT states are the sensitizing centers of the DB. Hence, for reasonable parameters which are consistent with all we know about the CBT states, these states are not the sensitizing centers of the DB. We also conclude from the simulations that an increase in the peak value (to  $\gamma_e \geq 1$ ) without a significant shift in  $T_{iq}$  indicates a change in  $P_v(T)$  without a change in  $N_D$ .

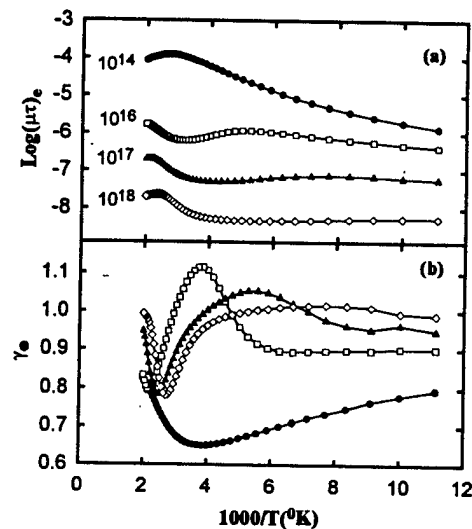


Figure 2. The computed  $T$ -dependence of the mobility-lifetime product (a) and the light intensity exponent (b) for four values of the dangling bond concentration (in  $\text{cm}^{-3}$ )

To check the effect of the first condition for sensitization, i.e. that  $C_{Dn}/C_{vn}$  will be large, we carried out a simulation with two values of this ratio. Indeed, as seen in Fig. 4, if this ratio is 3 the value of  $\gamma_e$  does not exceed 1 while if this ratio is 30 it does exceed the value of 1. We note then that since the capture coefficients are not expected to change significantly with preparation conditions, the above interpretation of the variation in  $\gamma_e$  values when a series of samples is studied, is valid.

The value of  $P_v(T)$  is also determined by the energy separation of the dark Fermi level  $E_F$  and the valence band edge  $E_v$ . As to be expected, the smaller the  $E_F - E_v$  the deeper the  $E_{Fp}$  for a given illumination intensity and  $T$ , and thus the larger the  $P_v(T)$ . Indeed, the comparison made in Fig. 5 of the  $\gamma_e$  values for  $E_F - E_v = 0.9$  eV and  $E_F - E_v = 1.3$  eV reveals this point. In the former we can get sensitization with  $\gamma_e > 1$  while in the latter  $\gamma_e < 1$ . This is important since it indicates, as was found in many experimental studies [11-13], that in doped (n-type) samples no sensitization or thermal quenching will be observed. Since, most of the recombination center parameters are fixed in a-Si:H, we can conclude that the absence of sensitization and thermal quenching is usually a signature of a large  $E_F - E_v$ , i.e. of a doped or contaminated sample. Whether this is the reason for the absence of sensitization can be distinguished from the reasons mentioned above, by finding (from the  $T$  dependence of the dark conductivity in a corresponding set of samples) whether a change in  $E_F - E_v$  took place.

From all the above we can further conclude that the appearance of a  $\gamma_e > 1$  limits the parameter space to an  $E_F$  located just above the midgap, to an  $N_D$  concentration of about  $10^{16} \text{ cm}^{-3}$  and to a VBT, of a width of about 0.05 eV and a DOS at the valence band edge of about  $10^{21} \text{ eV}^{-1}$ .

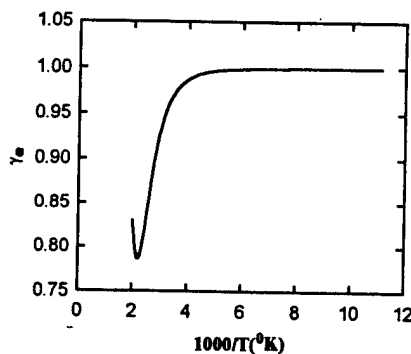


Figure 3. The computed  $T$ -dependence of the  $\gamma_e$  for dangling bonds in the case of negligible concentration of bandtail states.

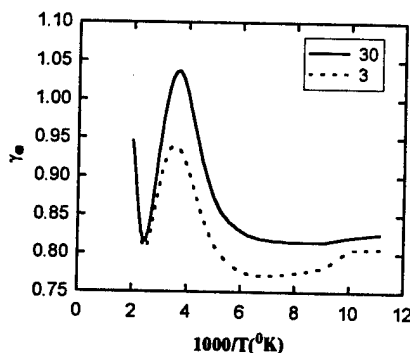


Figure 4. The computed temperature dependence of the light intensity exponent for two values of the  $C_{Dn}/C_{vn}$ .

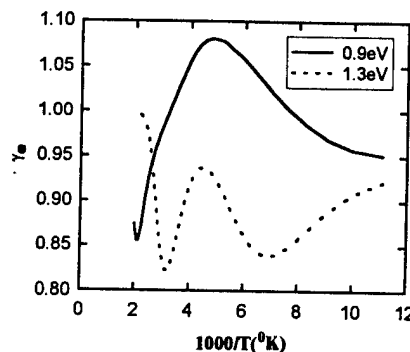


Figure 5. The computed  $T$ -dependence of the light intensity exponent for two positions of the Fermi level.

$1\text{ cm}^{-3}$ . These values are consistent with results derived from very different measurements [2] and thus shows that combining the computer simulation with the experimental features associated with the sensitization can indeed narrow the parameter space of the recombination centers, thus yielding quantitative spectroscopic information on these parameters.

## CONCLUSIONS

We have shown that the thermal quenching and sensitization of the electrons' lifetime in a-Si:H follows the Rose model of two types of recombination centers. The VBT states are the sensitizing centers of the DB. The examination of the T dependence of the light intensity exponent in the vicinity of the thermal quenching T reveals then non-trivial information on the recombination centers. This is useful in particular when a series of materials is considered as follows; A shift of the  $\gamma_c$  peak towards low T indicates an increase of the concentration of the DB. A decrease and broadening of the  $\gamma_c$  peak without a T shift indicates a reduction in the concentration of the VBT states, provided there is no significant change in the (easily measured) activation energy of the dark conductivity. Hence, given a series of samples, the simple measurements of the T dependence of the conductivity and photoconductivity can yield semiquantitative information on the recombination centers in a-Si:H. It will be also shown that combining such data with that of the ambipolar diffusion length can yield a more quantitative information.

## ACKNOWLEDGMENTS

The authors are indebted to Dr. A. Catalano for the samples used in this study. The present work was supported by US ARO grant No. DAAHO4-96-1-0405.

## REFERENCES

1. P.E. Vanier, A.E. Delahoy and R.W. Griffith, *J. Appl. Phys.* **52**, 5235 (1981).
2. M.Q. Tran, *Philos. Mag. B* **872**, 35 (1995).
3. R. Bruggemann, Photoconductive Properties, in *Future Directions in Thin Film Science and Technology*, Proc. 9<sup>th</sup> ISCMS, edited by J.M. Marshall and N. Kirov, (World Scientific, Singapore, 1997), p. 80.
4. A. Rose, *Concepts in Photoconductivity and Allied Problems* (Wiley Interscience, NY, 1963). For a recent manifestation of the sensitization effect see, I. Balberg and R. Naidis, *Phys. Rev. B* **57**, R6783 (1998). A semiquantitative theory of this manifestation in a-Si:H has been developed recently: R. Rapaport, M.Sc. Thesis, The Hebrew University, Jerusalem.
5. Y.-M. Li, B.F. Fieselmann and A. Catalano, Proc. of XXII PVSC (IEEE, NY, 1991), p. 123.
6. I. Balberg and Y. Lubianiker, *Phys. Rev. B* **48**, 8709 (1993).
7. M. Stutzmann, *Philos. Mag. B* **60**, 531 (1989).
8. W. Graf, K. Leihkamm, M. Wolf, J. Ristein and L. Ley, *Phys. Rev. B* **53**, 4522 (1996).
9. Y. Lubianiker, I. Balberg and L. Fonseca, *Phys. Rev. B* **55**, R15997 (1997).
10. R. Rapaport, Y. Lubianiker, I. Balberg and L. Fonseca, *Appl. Phys. Lett.* **72**, 103 (1998).
11. M. Hoheisel and W. Fuhs, *Philos. Mag. B* **57**, 411 (1988).
12. B. Cleve and P. Thomas, *Mater. Res. Soc. Symp. Proc.* **192**, 317 (1990).
13. R. Naidis and I. Balberg, unpublished.

# PLASMONS ON LUMINESCENT POROUS SILICON PREPARED WITH ETHANOL

## AND CRITICAL POINT DRYING

O. Resto\*, L.F. Fonseca\*, S.Z. Weisz\*, A. Many\*\*, Y. Goldstein\*\*

\*Department of Physics, University of Puerto Rico, Rio Piedras, PR 00931, USA

\*\*Racah Institute of Physics, The Hebrew University, Jerusalem 91904, Israel

### ABSTRACT

We investigated the plasmon characteristics on luminescent porous silicon using electron energy loss spectroscopy. The samples were prepared from p-type crystalline silicon, (100) face, using the conventional electrochemical etching technique with the usual solution of HF, ethanol and water, followed by a critical point drying process. The energy of the bulk plasmon was measured both before and after sputter cleaning the sample with argon-ion bombardment. We found that initially the plasmon energy was slightly higher, ~18 eV, than the plasmon energy of crystalline silicon. After sputter cleaning the sample with 5 keV Ar<sup>+</sup> ions, the plasmon energy increased to ~20 eV. Exposure to the electron beam used for the measurements caused a slow upward shift of the plasmon energy as a function of time, toward a saturation energy of 22-23 eV, an energy close to the plasmon energy of SiC. Auger spectroscopy performed in parallel showed an increasing carbon coverage. We prepared also samples without ethanol in the etching solution and/or with no critical point drying. Samples that did not undergo the critical point drying process showed consistently a practically constant plasmon energy, with almost no change upon sputtering and/or exposure to the electron beam. On the other hand, samples that were prepared with or without ethanol but using the critical point drying process, showed an appreciable increase in the plasmon energy upon exposure to the electron beam.

We conclude that traces of CO<sub>2</sub>, used in the critical point drying process, are stored in the pores of the porous silicon surface and serve as a source of carbon. Apparently, upon activation by argon bombardment or by the electron beam, the carbon interacts with the porous Si surface forming a carbon-silicon compound, most probably SiC.

### INTRODUCTION

Porous silicon [1-4] (PSi), obtained by electrochemical etching procedures applied to crystalline Si surfaces, exhibits high luminescence efficiencies in the visible range. It is quite clear now that the visible luminescence originates from the band-gap enlargement due to quantum confinement [3,4]. At the same time, the reasons for the high-efficiency luminescence are still somewhat under debate [3-5]. It was suggested that it is the amorphous or microcrystalline nature of the porous Si that is responsible for the phenomenon, or that the formation of silicon compounds such as siloxene (Si<sub>6</sub>O<sub>2</sub>H<sub>6</sub>) or species of Si-H, Si-O and Si-F bonds are involved in the luminescence [3,4]. The study of the plasmon energies on luminescent PSi is of interest for two main reasons. The nanostructure of PSi was shown [4,5] to have a coral-like structure consisting of a continuous hierarchy of columns and pores. Typical lengths of the columns are a few tens of nanometers, while their average radius is a few nanometers. As

(World  
f Low-

33), M.

cott, J.

Symp.

ersma,

od, R.  
6, 387

. B 54,

lman,

D. O.  
1876

1829

1620

State

such, one may expect that the energy of the surface plasmon will be downshifted with respect to its value on crystalline silicon. This has indeed been found to be the case by Sasaki *et al.* [6]. Another reason is that the plasmon structure is very sensitive to even minute quantities of adsorbates on the surface [7]. Thus a study of the plasmon structure may possibly detect and lead to the identification of surface species that may be involved in the luminescence process in PSi. Berbezier *et al.* [8] concluded from their investigation of the plasmon structure of PSi that the nanocrystalline PSi clusters are surrounded by an amorphous Si surface layer passivated by hydrogen.

In our study of the PSi plasmon structure we too observed the surface plasmon at a reduced energy due to the nanocrystalline structure of PSi [6] and also the plasmon attributed [8] to the collective oscillations of the interface between an amorphous Si-H cap layer and the Si crystallites. However, during our studies we encountered a strange phenomenon, namely we found that the energy of the silicon volume plasmon was shifting during the measurements to higher energies. We decided to investigate this effect and we present here the results and the probable reason for this effect.

## RESULTS AND DISCUSSION

The starting material was high-grade p-type silicon of resistivity in the range 0.5 - 1.5  $\Omega$  cm. A p<sup>+</sup> layer was formed by diffusing metallic Al into the back faces of the silicon wafers to obtain an ohmic contact. The sample was attached to a cylindrical Teflon cell via a Kalrez O-ring, the sample constituting the bottom of the cell, with its front surface, the (100) face, facing upwards. Before anodization, the samples were etched in 20% HF. In order to prepare the porous surface [4], a solution of HF, ethanol and water (1:2:1) was poured into the cell. A platinum electrode was immersed in the solution and a spring contact was attached to the p<sup>+</sup> contact. The anodization of the Si surface was carried out with a current density of 100 mA/cm<sup>2</sup>. After anodization, the samples were removed from the cell. Some of the samples underwent a critical point drying [9] sequence while others were simply rinsed by de-ionized water and dried with N<sub>2</sub> gas.

The photoluminescence of the PSi was excited by a 10 mW He-Cd laser beam ( $\lambda = 442$  nm). The spectra were measured by an ISA-320 Triax UV-visible spectrometer. Figure 1 shows a typical photoluminescence spectrum measured on one of our PSi samples. The maximum of the spectrum obtains at around 640 nm.

The samples studied were mounted in the vacuum chamber of a Physical Electronics model 560 Auger microprobe. An electron beam of ~100 nA intensity on a ~50x50  $\mu$ m<sup>2</sup> area was used to excite the plasmons and the scattered electrons were energy analyzed with a cylindrical mirror analyzer. The plasmons were measured mostly using a retarding field applied to the electrons so that they enter the

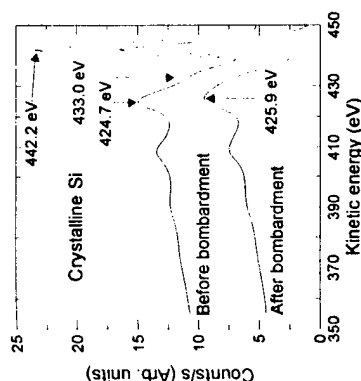


Fig. 2. Electron loss spectra of crystalline Si.

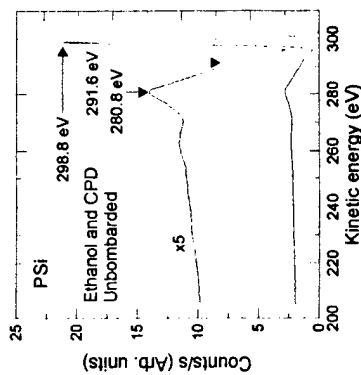


Fig. 3. Electron loss spectrum of unbombarded PSi prepared with ethanol and CPD.

analyzer at a low (constant) energy. The resolution attained in this mode was better than 600 meV. The measurements were done both before and after a bombardment cleaning with Ar ions at 5 keV and at a current intensity of ~200 nA on an area of ~2x2 mm<sup>2</sup>. For comparison purposes we performed measurements on crystalline silicon as well.

Figure 2 shows the plasmon peak (and its satellites) measured on crystalline silicon both before and after argon ion bombardment. The electron beam energy in this measurement was 442.2 eV, as marked in the figure. The plasmon peak energies are also marked. We see that the plasmon energy after the bombardment is 16.3 eV, about what is expected for the bulk plasmon of silicon [6,8]. We see also the peaks due to multiple plasmon losses, and their energies scale with the single-plasmon loss. The plasmon energy before the bombardment is somewhat larger, 17.5 eV. Here we see also a shoulder at 9.2 eV due perhaps to some Si-H compounds as suggested in ref. 8. In Fig. 3 we show typical electron loss results from a PSi sample that underwent the critical point drying (CPD) procedure and was not ion bombarded. (The upper curve in the figure is a blow-up by a factor of 5 of the lower curve.) The e-beam energy for this measurement was 298.8 eV, as marked. The energy of the plasmon peak (280.8 eV) is also marked in the figure. We see that the plasmon energy here has already increased to 18.0 eV and similarly the energies of the multiple plasmon losses. There appears also a shoulder at ~7.2 eV, probably due to the surface plasmon, its energy reduced because of the PSi nanostructure [6].

When we ion bombarded the PSi sample, we noticed that the plasmon loss peak shifted to higher energies, to about 20 eV. In addition, we also observed a shift to higher energies just by exposing the PSi samples to the electron beam used to excite the plasmon losses. This is illustrated in Fig. 4 which shows the dependence of the plasmon energy on the exposure time to the electron beam for a PSi sample that had undergone critical point drying, before (triangles) and after (circles) argon ion bombardment. As we can see, before the bombardment the plasmon energy increases with exposure time from a starting value of ~18.3 eV up to ~19.3 eV. After bombardment, the initial plasmon energy is already ~20 eV and with exposure time it continues

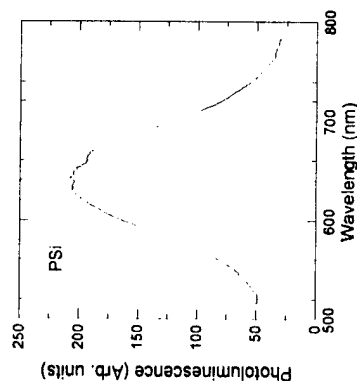


Fig. 1. Typical photoluminescence spectrum of our PSi samples.



to increase until it saturates at ~23 eV.

The saturation plasmon energy is close to the plasmon energy of SiC [10]. This prompted the idea that the Ar bombardment and/or electron-beam irradiation promote the formation of SiC on the surface of the PSi. This may be somewhat similar to the phenomenon reported by Heera et al. [11] who found that bombardment by Ge<sup>+</sup> ions caused a crystallization of amorphous SiC.

We performed Auger surveys to check for possible carbon increase on the PSi surface due to e-beam irradiation. Figure 5 shows two such surveys, the first, curve (a), was taken 17 min. after turning on the e-beam and the second, curve (b), after an additional interval of 7 min. The positions of the Si, C and O peaks are marked in the figure. We see that both the C and O peaks in curve (b) show a marked increase. No similar increase was detected on the crystalline-Si part of the sample.

The preparation of the porous samples involves carbon both in the anodization process, via ethanol, and in the critical point drying process, via liquid CO<sub>2</sub>. In order to eliminate these sources of carbon, we prepared a sample without ethanol in the anodizing solution, and cleaned it only by rinsing with de-ionized water and drying with N<sub>2</sub> gas. We measured the plasmon energy for this sample before and after argon-ion bombardment as a function of the exposure time to the electron beam. In both cases the plasmon energy was found to be practically constant, around 17.5 eV, and did not change with exposure time and argon bombardment.

In order to identify which of the forms of carbon, ethanol or CO<sub>2</sub>, is responsible for the carbon contamination of the PSi surface, we prepared two types of samples: samples that were anodized without ethanol in the anodizing solution and then went through the critical point drying process, and samples that were anodized with ethanol but did not go through the CPD process. We measured the plasmon energy as a function of exposure time to the e-beam, and the results are shown in Figs. 6 and 7. In Fig. 6 we plot the plasmon energy measured on the PSi sample that was prepared without ethanol but underwent the

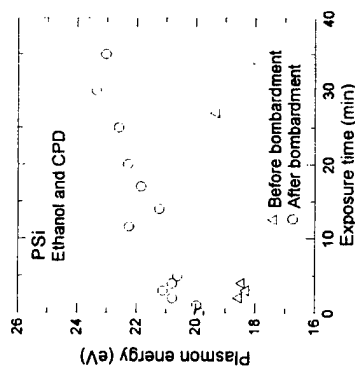


Fig. 4. Plasmon energy as function of exposure time to e-beam for a PSi sample prepared with ethanol and CPD, before (triangles) and after (circles) Ar bombardment.

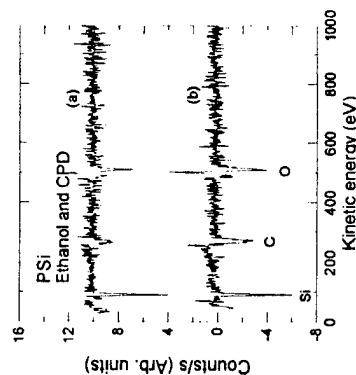


Fig. 5. Auger surveys of a PSi sample prepared with ethanol and CPD. Curve (a) was taken 17 min. after turning on the e-beam and curve (b) after an additional interval of 7 min.

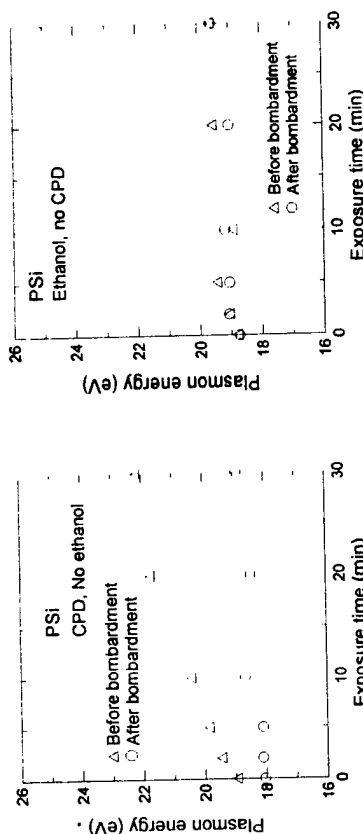


Fig. 6. Plasmon energy as function of exposure time to e-beam for a PSi sample anodized without ethanol and dried by CPD, before and after argon bombardment.

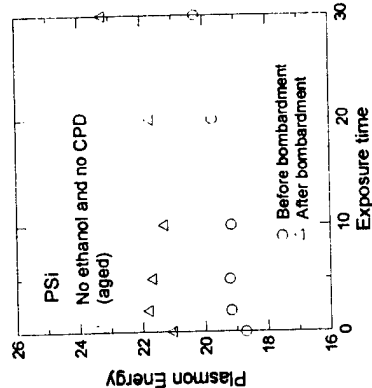


Fig. 7. Plasmon energy as function of exposure time to e-beam for a PSi sample prepared with ethanol but without CPD, before and after argon bombardment.

CPD process. As we can see, the plasmon energy before the bombardment (triangles) starts close to 19 eV and increases with exposure time, even above the plasmon energy for samples prepared with ethanol and CPD (see Fig. 4). The plasmon energy saturates around 22.2 eV. We also measured, in parallel, by Auger electron spectroscopy, the surface carbon concentration and found that it increased by ~40% compared to its value before turning on the e-beam. The plasmon energy after the bombardment (circles) starts at a little above 18 eV and changes only slightly and, in parallel, the surface carbon concentration remains practically constant. In Fig. 7 we plot the plasmon energy measured on the other PSi sample, that which was prepared with ethanol but did not undergo the CPD process. Here we see that the plasmon energy is almost unchanged upon exposure to the electron beam and/or upon argon bombardment. The surface carbon concentration increased only by ~10% compared to its value before turning on the e-beam. Apparently, the possible remnants of ethanol in the pores are not an efficient source of surface carbon.

A PSi sample that was prepared without ethanol and without critical point drying, was left to age in room atmosphere. After 4 months we re-measured the plasmon energy and the results are plotted in Fig. 8. We see that after the aging the plasmon energy before sputtering (triangles) starts close to 22 eV and still rises a little upon exposure to the e-beam. This again suggests very strongly that we are looking on

plasmons affected by CO<sub>2</sub> and/or CO adsorbed from the atmosphere. After sputtering (circles), the plasmon energy starts at a lower energy (~19 eV) but again increases upon exposure to the e-beam. Our interpretation is that the bombardment removed some of the carbon from the surface but there is still carbon stored in the pores.

## CONCLUSIONS

We found that the plasmon energy, measured on porous silicon surfaces prepared with critical point drying, drifts to higher energies upon electron beam irradiation and/or ion bombardment of the surface. The saturation energy of the plasmon is close to the plasmon energy of SiC. Apparently, due to the critical point drying process, CO<sub>2</sub> accumulates in the pores and the electron beam irradiation and/or ion bombardment decompose the CO<sub>2</sub> and promote the formation on the porous surface of a silicon-carbon compound, most probably SiC. Aging the PSi surface in room air causes a similar drift of the plasmon energy, due apparently to adsorbed CO<sub>2</sub>.

## ACKNOWLEDGMENTS

This work was supported by US ARO grant No. DAAH04-96-1-0405, by NASA grant No. NCCW-0088, and by the Ministry of Science and Arts, Israel, within the framework of the infrastructure-applied physics support project.

## REFERENCES

1. L. T. Canham, *Appl. Phys. Lett.* **57**, p. 1046 (1990).
2. I. Amato, *Science* **252**, p. 922 (1991).
3. See, for instance, Z.C. Feng and R. Tsu, *Porous Silicon* (World Scientific, Singapore, 1994).
4. See review article by A.G. Cullis, L.T. Canham and P.D.J. Calcott, *J. Appl. Phys.* **82**, p. 909 (1997) and references therein.
5. F. Koch in *Silicon Based Optoelectronic Materials*, edited by R.T. Collins, M.A. Tischler, G. Abstreiter, and M.L. Thewalt (Mater. Res. Soc. Proc. **298**, Pittsburgh, PA, 1993), p. 319-324.
6. R.M. Sasaki, F. Galembeck, and O. Teschke, *Appl. Phys. Lett.* **69**, p. 206 (1996).
7. Millo, Y. Goldstein, A. Many, and J.I. Gersten, *Phys. Rev. B* **39**, p. 1006 (1989).
8. I. Berbezier, J.M. Martin, C. Bernardi, and J. Derrien, *Appl. Surf. Sci.*, **102**, p. 417 (1996).
9. J. Von Behren, P.M. Fauchet, E.H. Chimowitz, and C.T. Lira in *Advances in Microcrystalline and Nanocrystalline Semiconductors*, edited by R.W. Collins, P.M. Fauchet, I. Shimizu, J.-C. Vial, T. Shimada, and A.P. Alivisatos (Mater. Res. Soc. Proc. **452**, Pittsburgh, PA 1997), p. 565-570.
10. H. Raether, *Excitation of Plasmons and Interband Transitions by Electrons* (Springer, Berlin, 1980), Ch. 5.
11. V. Heera, J. Stoemenos, R. Kögler and W. Skorupa, *J. Appl. Phys.* **77**, p. 2999 (1995).

## SILICON-BASED UV DETECTOR PROTOTYPES USING LUMINESCENT POROUS SILICON FILMS.

Limarix Peraza\*, Madeline Cruz\*, Angel Estrada\*, Carlos Navarro\*\*, Javier Avalos\*, Luis F. Fonseca\*\*, Oscar Resto\*\*, and S. Z. Weisz\*\*

\*Dept. of Sciences and Technology, Metropolitan University, San Juan, PR.

\*\*Dept. of Physics, University of Puerto Rico, San Juan, PR 00931.

### ABSTRACT

The luminescent properties of porous silicon (PSi) films in the visible region were used to improve the photoresponse of PSi/Si-wafer and PSi/Si p-n junctions UV detector prototypes in the region below 500nm. A luminescent PSi overlay was formed on top of the Si wafers and p-n junctions by electrochemical anodization. These overlayers have emission spectra peaking close to 690nm. In the case of the PSi/Si wafer, the PSi film was produced with a high optical transparency above 600nm and highly absorbent below this value. With such characteristics, the incident UV radiation is partially absorbed and converted into visible radiation that can be highly transmitted through the PSi film and efficiently absorbed by the wafer or the junction. The UV measurements show enhancement of the photoresponse at 366nm as compared with control prototypes without PSi. Details about the enhancement process are discussed.

### INTRODUCTION

The use of silicon for UV-photodetection applications faces the problem of the silicon surface UV response that reduces significantly the interband light absorption in this region of the EM spectrum. In a typical commercial Si-based detector, the photosensitivity at 400nm is of the order of 5 times smaller than at 800nm around which the detector has its maximum sensitivity. Methods have been developed to overcome such difficulty and produce the so-called UV-enhanced silicon detectors. Today, a new possibility to enhance the UV-photoresponse of silicon-based detectors is the inclusion of photoluminescent PSi layers into the design of the device.

After the report of efficient photoluminescence from electrochemically etched silicon wafers [1], considerable effort has been done on the study and the development of electrooptical applications of PSi [2,3]. The maximum of the photoluminescence emission of PSi changes with the characteristics of the silicon wafer and the preparation method but it is in the range between 800nm and 650nm for a typical freshly dried and exposed to air sample. These emission spectra have broad bands. The main idea to improve the sensitivity of a silicon-based UV detector using PSi is to exploit the efficient UV-to-visible conversion mechanism of PSi layers. A prototype of such a PSi-based new detector will operate under the assumption that UV incoming radiation is absorbed by the PSi layer and re-emitted as visible radiation according to the above discussed photoluminescence properties of the PSi layer. The converted energy then is in the frequency range of maximum photosensitivity of the bottom part of the device. Several prototypes have been developed in recent years using PSi to improve the photosensitivity of the Si-based UV detectors. Some of the studied photodiode structures are: metal/PSi/c-Si, and n-PSi/p-PSi/c-Si [4-7]. The performance of those structures is based on the I-V response for electric charge transport along the direction perpendicular to the layers. Characteristic band bending and an increasing photosensitivity with strong dependence on the reverse bias voltage were found at the PSi/c-Si interface [8].

We studied the photoresponse of two types of structures under UV illumination: PSi/p-Si/Al and PSi/n-Si/p-Si/Al. The first structure was studied by measuring the change in the voltage drop, with and without illumination, for an electric current passing through the p-Si layer. In this case

PSi overlayer was used as a UV-to-visible conversion interface. The second heterostructure was studied by measuring the photovoltage across the p-n junction/PSi structure.

## EXPERIMENT AND RESULTS

We prepare PSi by electrochemical anodization of crystalline Si using an acid solution containing HF, water, and ethanol. The Si wafer, as well as the p-n structure, are previously prepared to have an aluminum ohmic contact at the bottom (at the p-Si side) deposited by sputtering and annealed at 440 °C during 10min. The wafer is then mounted at the bottom of a teflon electrolytic cell with the crystalline Si surface facing towards the cell where the acid solution is poured once the surface is cleaned with 20%HF-water solution during 20min. A platinum cathode in contact with the acid solution and a computer controlled constant current source complete the circuit. With this procedure, the PSi layer grows from the top towards the bottom of the wafer as the electric current is applied.

It is generally accepted that the visible photoluminescence of PSi is related to the quantum confinement of the free carriers in nanocrystalline Si-structures formed by the electrochemical etching process [1,2]. Depending on the resistivity of the silicon wafer and the anodization parameters, one can get luminescent PSi with quite different microstructures. SEM and TEM of PSi samples show that it can indeed be prepared to yield nanoporous or microporous films. Samples in which a columnar or coral-like structure of pores with diameters of the order of microns also exhibit PL indicating the existence of nanoporous structure on the pore-walls but this kind of microstructure produces large light scattering at the visible wavelengths. Optically, nanoporous-Si behaves as a homogenous material in the visible and longer wavelength regions, as shown by ellipsometry, reflectivity, and transmittance measurements, and effective medium calculations for the dielectric function of such samples. Considering that our application requires high transparency above 600nm, the formation parameters were set to produce nanoporous PSi layers.

A prototype was prepared from a 250 $\mu$ m-thick p-type Si wafer with 20 $\Omega$ cm resistivity and (100) surface orientation. After the corresponding sputtering and annealing processes that produces the bottom aluminum ohmic contact, the disk was mounted on the electrolytic cell and a central circular area of 0.5cm<sup>2</sup> was reduced in thickness to 60 $\mu$ m by dissolving the wafer during 105s by pouring a mixture of hydrofluoric, nitric and acetic acids (CP-4) in proportions 3:5:3 into the cell. After this step, the cell and the wafer were washed with deionized water and the cell filled up with a 1:1:2 (HF:water:ethanol) electrolytic solution. The exposed area was then anodized for 120s by passing a current density of 100mA/cm<sup>2</sup> between the aluminum contact and the platinum cathode. With this current density, a PSi film of 10 $\mu$ m was formed. After anodization, the wafer was washed with ethanol and left under ethanol during 3 hours. Finally, the prototype was dried using the supercritical point drying method [9]. After the drying process, two bottom ohmic contacts were prepared by partially dissolving the aluminum bottom layer with HCl. Figure 1 shows the schematic configuration of the prototype.

Figure 2 shows the photoluminescence spectrum of the PSi overlayer. The spectrum was obtained by exciting the layer with a 442nm defocused laser beam. The figure shows a broad band emission peaking at 670nm which is within the radiation energy range of high sensitivity for Si-based photodetection. Figure 3 shows the transmission spectrum of a free standing PSi film prepared from a p-type Si wafer and with similar characteristics to the one used in the prototype. The figure shows high transparency above 600nm. The significant reduction of the transmission coefficient below 500nm is associated with a large absorption of the incident radiation at this frequency range. This absorption is related with the conversion of the UV incoming radiation to visible as is shown in the photoluminescence response of the PSi film (figure 2).

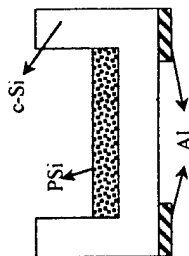


Figure 1. Schematic configuration of the first prototype.

The UV photoresponse of the prototype was determined and compared with a control device similarly prepared but without the PSi cover layer. We studied the photoresponse by passing a lateral current through the c-Si layer between the two aluminum ohmic contacts. The change in the voltage drop across the devices ( $\Delta V$ ), with and without UV illumination, as a function of the lateral current was measured using an exciting 360nm UV radiation with an intensity of 7 $\mu$ W/cm<sup>2</sup>. Figure 4 shows the photoresponse of the prototype as compared with the control.

The second studied prototype was prepared from a 250 $\mu$ m p-type Si wafer of ~1 $\Omega$ cm resistivity and with a 20 $\mu$ m thick n-type Si overlayer, epitaxially grown on top forming a p-n junction. The resistivity of the epitaxial n-type layer was ~4  $\Omega$ cm. This wafer was treated in similar way as the previous one. First, the aluminum ohmic contact was formed at the bottom side, after that the n-type epitaxial layer was cleaned with 20% HF solution and exposed to the 1:1:2 electrolytic solution and anodized during 40s using a current density of 100mA/cm<sup>2</sup>. Because of the hole-deficiency of the n-type layer, the surface was illuminated during anodization with a quartz white lamp with an intensity of 100mW/cm<sup>2</sup>. The process, as describe above, results in the formation of a PSi layer of ~3 $\mu$ m. After the anodization, the prototype was dried using the same procedure as explained for the first prototype. In this case the photoresponse was tested on the photovoltage across the p-Si/n-Si/PSi structure. For such measurements, the contacts were the

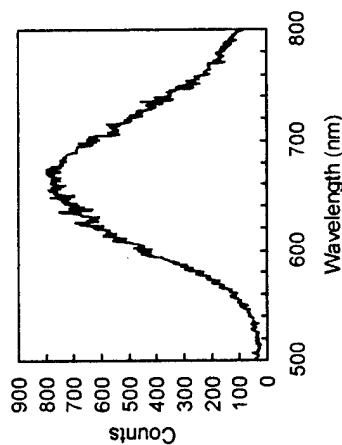


Figure 2. Photoluminescence spectrum of the PSi overlayer.

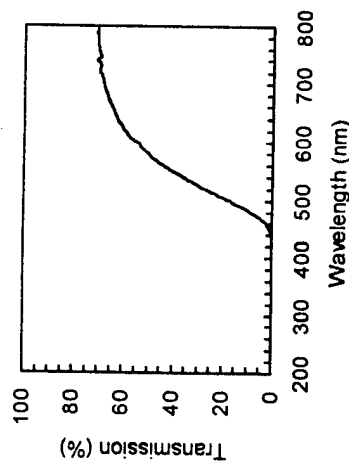


Figure 3. The transmission spectrum of a PSI free standing film.

aluminum bottom contact deposited at the p-side and a sputtered gold thick film of 1mm in diameter deposited on top of the PSI overlayer and close to the border of the anodized region, as shown in figure 5. To determine the UV photoresponse of this prototype, we measured the voltage between the gold and the aluminum contacts when the PSI layer was illuminated with the exciting 360nm UV radiation with an intensity of  $7\mu\text{W}/\text{cm}^2$ . The measured voltage was 12.3mV. The measured voltage for a control prototype prepared in similar way but without the PSI layer was 1.2mV under similar conditions.

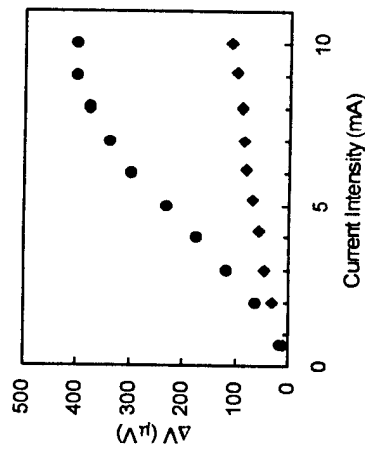


Figure 4. Photoresponse of the first prototype (circles) as compared with the control (diamonds).

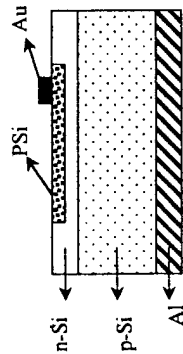


Figure 5. Schematic configuration of the second prototype

## CONCLUSIONS

Two Si-based light detector prototypes using PSI and with enhanced UV response were prepared and studied. The supporting idea for using PSI to produce such enhancement rests on the fact that Si have reduced UV photosensitivity and PSI can be used as an interface that converts UV radiation into visible radiation which is efficiently used by Si for the photogeneration of free carriers. The application of such procedure requires the preparation of a PSI overlayer with enough optical quality that will allow the transmission of the re-emitted visible photons to the crystalline Si region. We succeeded on the preparation of high optical quality PSI films, as is evident from figure 3. The enhancement of the photoresponse of the first prototype, measured as the increasing of the slope of the  $(\Delta V)-I$  curve, was confirmed from the graph of figure 4 which shows an increasing of 354% as compared with the corresponding slope for the control. It is worth noting that in the case of the first prototype, the electric current flows in a lateral configuration instead of along the different layers. In that case, it is reasonable to assume that the electric current is passing mainly through the c-Si layer that has less resistivity than the PSI layer which acts as a visible photons provider.

The second prototype based on a p-n junction structure also showed a significant enhancement of the UV photoresponse in the near UV region. The electric charge transport in this case transverses through the different layers, including the PSI region. It is worth mentioning that the SEM image of the PSI structure for the case of the p-n junction points to the existence of porous structures with diameters of the order of  $4\mu\text{m}$ . The size of these pores are large enough that scattering of visible light is expected. However, for that kind of prototype, the thickness of the PSI film is small, as compared with the first prototype, to reduce the scattering losses.

Both prototypes have shown that PSI can be used to increase the photosensitivity of Si-based detectors in the UV spectral region. The operational principle is based on the ability of PSI to absorb UV photons and reemit in the visible region where the Si shows better photosensitivity. The expected enhancement will depend on the efficiency of the energy conversion process related with the fraction of visible photons that are re-emitted from the total absorbed UV photons. From the presented results, one can conclude that the re-emission efficiency is large enough to overpass the small fraction of UV photons that causes direct free carriers photogeneration in c-Si. As a final remark, due to the geometry of our prototypes, there is a possibility that free carriers generated at the PSI layer can diffuse into the active region. This other mechanism will also contribute to the enhanced photoresponse of the detector.

#### ACKNOWLEDGMENTS

Authors at the Metropolitan University acknowledge support from NSF-MJE grant Authors from University of Puerto Rico acknowledge partial support from NASA grant No. NCCW-0088 and US ARO grant No. DAAH04-96-1-0405.

#### REFERENCES

1. L. T. Canham, *Appl. Phys. Lett.*, **57**, 1046 (1990).
2. A. G. Cullis, L. T. Canham, and P. D. Calcott, *J. Appl. Phys.* **82**, 909 (1997).
3. See contributions to *MRS Bulletin* **23**, (1998).
4. J. P. Zheng, K. L. Jiao, W. P. Shen, W. A. Anderson, and H. S. Kwok, *Appl. Phys. Lett.* **61**, 459 (1992).
5. L. V. Belyakov, D. N. Goryachev, O. M. Sreseli, and I. D. Yorasbeskii, *Semiconductors* **27**, 758 (1993).
6. T. Ozaki, M. Araki, S. Yoshimura, H. Koyama, and N. Koshida, *J. Appl. Phys.* **76**, 1986 (1994).
7. B. Unal and S. C. Bayliss, *J. Phys. D: Appl. Phys.* **30**, 2763 (1997).
8. L. A. Balagurov, D. G. Yarkin, G. A. Petrovicheva, E. A. Petrova, A. F. Orlov, and S. Ya. Andryushin, *J. Appl. Phys.* **82**, 4647 (1997).
9. J. Von Beheren, P. M. Fauchet, E. H. Chimowitz, and C. T. Lira, *Mat. Res. Soc. Symp. Proc.* **452**, 565 (1997).

## ELECTRO-POLYMERIZATION IN POROUS SILICON FILMS

R.K. SONI, L.F. FONSECA, O. RESTO, A. GUADALUPE\*, AND S.Z. WEISZ

Department of Physics, University of Puerto Rico, Rio Piedras, San Juan-00931, PUERTO RICO

\*Department of Chemistry, University of Puerto Rico, Rio Piedras, San Juan-00931, PUERTO RICO

### ABSTRACT

Luminescent porous silicon films were created by electrochemical anodization of n-type substrate under light illumination. Semi-transparent conducting polypyrrole films were deposited by electrochemical polymerization at a low current density. The SEM micrographs showed that the polymer film impregnates into the wide vertical pores of 1-5  $\mu\text{m}$  and grows sideways suggesting strong current distribution on the walls. The AFM images of polymer surface reveal nanometer size polymer aggregates on the porous layer. The impregnation of the polymer film due to sideways growth provides a useful mean to fabricate stable contact for light emitting diodes from porous silicon.

### INTRODUCTION

Efficient visible photoluminescence (PL) from porous silicon has resulted in enormous interest in the optoelectronic properties of the material with an eye on silicon based light emitting devices. While stable and highly efficient PL, originating from radiative recombination of carriers in nanocrystalline silicon, is obtained routinely, the electroluminescence (EL) efficiency is rather low and unstable [1]. Early attempts with aqueous electrolytic contact showed high EL efficiency and an ideal rectifying characteristic but poor stability caused by surface oxidation of the top porous layer [2]. Efforts with all solid contacts, such as semitransparent gold, indium tin oxide, have not met with desired efficiency and stability due, partly, to local injection of carriers at the interface between electrode-porous layer [3-4]. For better electrical contacts and uniform carrier injection, it is desirable to completely fill the pores of highly disordered surface of the porous silicon layer with a transparent and conducting polymer. Conducting polymers, such as polypyrrole [5-7] or polyaniline [8], have shown promising results in the formation of rectifying junction with porous silicon film.

Polypyrrole (PPy) is one of the most stable conducting polymer known [9] and can be easily synthesized by electro-chemical oxidation. One of the key advantage of electro-chemical method is that the thickness of the polymer film is proportional to the time integral of the anodic current pulse, thus by controlling either the current or the time of oxidation, polymer film of desired thickness can be grown. Physical properties of PPy are, however, influenced by growth conditions such as monomer concentration, electrolyte concentration, solvent composition, and preparation temperature. Furthermore, during polymerization the PPy is simultaneously oxidized owing to the lower oxidation potential compared to that of monomer and this causes incorporation of counter-anion from the electrolyte during the growth process to maintain electrical neutrality. It is therefore expected that the electrical properties of PPy will be sensitive to the nature of the counter-anion present in the grown film.

We report here the growth of semitransparent conducting polypyrrole film on the n-porous silicon layers with varying surface morphology and formation of a rectifying junction between conducting pyrrole and porous silicon.

## EXPERIMENT

Porous silicon layers were created by usual anodic oxidation in a solution of 25% HF in ethanol from n-type silicon wafers of (100) under light illumination of  $100 \text{ mW/cm}^2$ . The sample was etched with a solution of 20% HF in ethanol for 10 minutes before the anodization and rinsed with ethanol and deionised (DI) water after the completion of the anodization process. Drying was avoided to prevent cracking of the grown porous film. Each sample was checked for PL by exciting with the 442 nm line of a He-Cd laser. The film thickness and pore size was determined from cross-sectional SEM micrographs. Table-I lists the growth parameters of porous films.

Table-I: Growth parameters of porous silicon film

Sample	Substrate	Resistivity $\rho$ (ohm-cm)	Current density J ( $\text{mA/cm}^2$ )	Anodization time (sec.)	Film thickness $\mu\text{m}$	Pore size $\mu\text{m}$
A	n-p junction	4.6	50	600	12	2-6
B	n-type	0.4-1.6	100	120	11	1-2

Polypyrrole film was deposited at low temperature ( $0^\circ\text{C}$ ) immediately after the porous silicon film was created by applying a controlled current pulse to the cell containing solution of 0.5 M vacuum freshly distilled pyrrole monomer, solvent and 0.5 M  $\text{HClO}_4$  as the supporting electrolyte. The solvent was either acetonitrile or DI water, we observed that acetonitrile quenches PL from the porous layer, therefore DI water was preferred as solvent as well as for final rinsing

## RESULTS

On a bulk silicon substrate the PPY film grows linearly with time at low current density  $J = 2 \text{ mA/cm}^2$ . The grown film appears black in color and inhomogeneous. The extent of oxidation in PPY increases its room temperature conductivity, which is comparable to that of silicon, but also enhances absorption in the visible region of spectrum. In order to study the growth of PPY on highly disordered porous layers, we synthesized porous layers with variety of surface morphology by varying anodization conditions as well as the substrate.

Figure 1 (a) shows cross-sectional SEM micrograph of porous silicon layer (sample A) prepared on an epitaxial layer. A large minority carrier injection in the  $20 \mu\text{m}$  n-type epitaxial layer causes strong anodic reaction and results in a highly disordered comb like structure with  $2-5 \mu\text{m}$  wide vertical pores. The polypyrrole film synthesized on a freshly prepared sample A at current density  $2 \text{ mA/cm}^2$  in a solution containing monomer in acetonitrile with  $0.5 \text{ M HClO}_4$ . The conducting polymer penetrates into the large-scale pore structure of the material and grows on the pore walls, Fig. 1 (b). With increasing pulse duration, the film grows side ways suggesting strong and even distribution of current on the pore walls. The SEM micrograph provides a direct evidence of the extent of PPY incorporation inside the pores. Earlier evidences of polymer incorporation were estimated either by polymer film thickness measurement [6,7] or by micro Raman [5] detection of polymer on porous layer. It appears that the pore filling is mainly through side way growth of polymer rather than from bottom to top [5-7]. When the current is high, voids are observed inside the pore, effective filling of the pores is possible when charge transfer process across the polymer/porous silicon interface is slow.

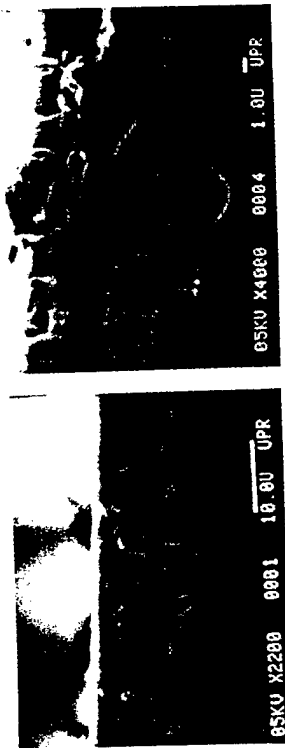


Fig. 1 Cross-sectional SEM micrograph of (a) porous silicon layer on an n-type epitaxial film showing wide pores and (b) impregnation of conducting polypyrrole in these pores by electro-polymerization at low current density.

The porous film emits strong orange-red PL before the polymerization with a peak at  $670 \text{ nm}$ , and after the polymerization there is an expected decrease in PL intensity of about 60% accompanied by a small shift of peak towards lower wavelength, indicating a good transmission for the visible light. The electrical transport property of the sample was investigated by depositing semitransparent gold film on the polymerized porous silicon layer. In the forward bias condition, gold film connected to the positive electrode, the device shows weak conductivity with rectification ratio of 80 at 20 volts.

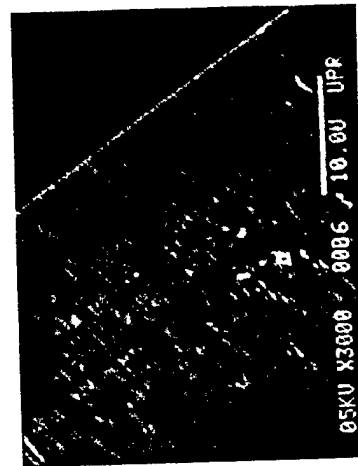


Fig. 2 Cross-sectional SEM micrograph of conducting polypyrrole film on n-type porous silicon.

Sample B is prepared by anodic reaction with 25% non-ethonic HF solution. The porous layer, consists of a large density of  $\sim 1 \mu\text{m}$  wide vertical pores, emits strong orange-red PL when



excited with 442 nm laser line as well as strong red EL with 5% solution of NaCl. At low current density, the polymer film grows on the surface as well as with in the pore through sidewalls.

With increasing current density or time, the polymer film deposits preferentially on the surface so much so that a large number of pores remain unfilled suggesting large charge carrier injection at the surface. Figure 2 shows SEM micrograph of 1  $\mu\text{m}$  pyrrole film deposited on sample B at the current density  $J = 2 \text{ mA/cm}^2$  for 180 sec. An Atomic Force Microscope (AFM) is utilized to reveal morphology of polymer surface. Figure 3 shows an AFM image of sample B surface. The surface is flat and reveals nanometer size (50-70 nm) polymer aggregates on nanocrystalline silicon surrounding the pore.

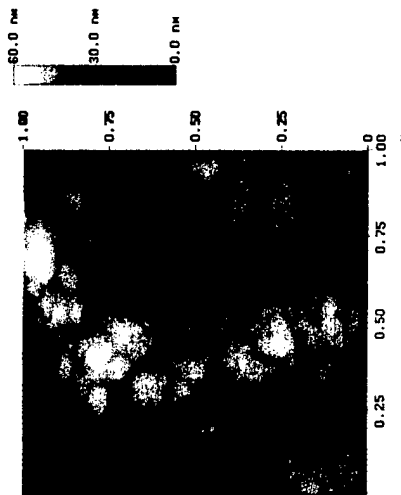


Fig. 3 Atomic force microscopy image of conducting polypyrrole film grown on n-type porous silicon.

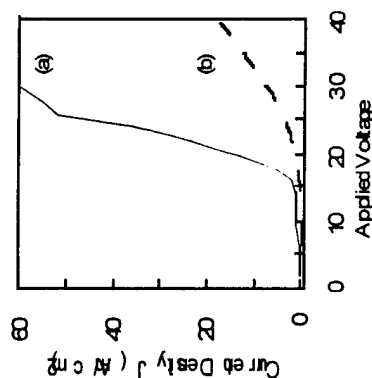


Fig.4 Current-voltage curve of gold/n-porous silicon (a) with and (b) without polymer film.

The current-voltage characteristic of gold/pyrrole/n-porous silicon diode exhibits, Fig. 4, a typical rectifying junction with a marked improvement in the conductivity compared to diode fabricated without pyrrole film. We believe that the large potential drop in the porous layer is a consequence of low carrier mobility across the highly structured interface between polymer aggregates and nanostructured silicon.

## CONCLUSIONS

We have shown that it is possible to fill the pores in a porous silicon layer with conducting pyrrole by slow electro-polymerization at very low current density. The polymer grows preferentially on the pore walls, not from the bottom as generally believed, due to large charge injection from the walls. Though SEM micrograph provides a direct evidence of the extent of polymer incorporation inside the pores, further microscopic experiments are required to study the pore filling under various growth conditions. A thin ( $< 1 \mu\text{m}$ ) and homogeneous layer of the polymer can be grown on the porous silicon surface under suitable growth conditions, AFM images reveal nanometer size polymer aggregates and micro holes at the surface of the polymer. The electrical transport in a diode structure is enhanced by impregnation of conducting polymer, the conductivity is inferior compared to liquid contacts due to highly disorder nature of the polymer surface and polymer/porous silicon interface.

## ACKNOWLEDGEMENTS

Authors acknowledge partial support from NASA grant No. NCCW-0088, US ARO grant No. DAAHO4-96-1-0405 and DOE-EPSCoR 046138.

## REFERENCES

1. A.G. Cullis, L.T. Canham, and P.D.J. Calcott, *J. Appl. Phys.* **82**, 909 (1997).
2. M.I.J. Beale, L.T. Canham, and T.J. Cox, in *Mat. Res. Soc. Symp. Proc.* **283**, (1993) p. 377.
3. N. Koshida and H. Koyama, *Appl. Phys. Lett.* **60**, 347 (1992).
4. F. Namavar, H.P. Muruska, and N.M. Kalkhoran, *Appl. Phys. Lett.*, **60**, 2514 (1992).
5. J.D. Moreno, F. Agullo-Rueda, R. Guerrero-Lemus, R.J. Martin Palma, J.M. Martinez-Duart, M.L. Marcos, and J. Gonzalez-Velasco, in *Mat. Res. Soc. Symp. Proc.* **452**, (1997) p.479-484.
6. N. Koshida, H. Koyama, Y. Yamamoto, and G.J. Callins, *Appl. Phys. Lett.* **63**, 2655 (1993).
7. G. Wakefield, P.J. Dobson, Y.Y. Foo, A. Loni, A. Simons, and J.L. Hutchison, *Semicond. Sci. Technol.* **12**, 1304 (1997).
8. K. Li, D.C. Diaz, Y. He, J.C. Campbell, and C Tsai, *Appl. Phys. Lett.* **64**, 2394 (1994).
9. B.R. Saunders, R.J. Fleming, and K.S. Murray, *Chem. Mater.* **7**, 1082 (1995).

# The effect of hydrogen on the network disorder in hydrogenated amorphous silicon

S. Gupta, R. S. Katiyar, G. Morell, and S. Z. Weisz

*Department of Physics, University of Puerto Rico, San Juan 00931, Puerto Rico*

I. Balberg<sup>a)</sup>

*The Racah Institute of Physics, The Hebrew University, Jerusalem 91904, Israel*

(Received 12 March 1999; accepted for publication 10 September 1999)

Previous Raman scattering studies of the effect of hydrogen on the atomic network disorder in various hydrogenated amorphous silicon (*a*-Si:H) materials resulted in contradicting conclusions. We resolve these contradictions by showing that the surface and the bulk of *a*-Si:H films can behave differently due to their different hydrogen contents. In particular, we establish that hydrogen has a relatively moderate effect in improving the short-range order but a profound effect in improving the intermediate-range order of the atomic network. © 1999 American Institute of Physics. [S0003-6951(99)05244-4]

The effect of the disorder in the atomic network on the electronic properties of amorphous semiconductors has been discussed extensively in the literature.<sup>1,2</sup> In particular, for hydrogenated amorphous silicon (*a*-Si:H) an obvious issue is the role of hydrogen in the network disorder. While this issue has been considered already a decade ago,<sup>3</sup> it has regained recent interest<sup>4</sup> in relation to the Staebler-Wronski (SW) effect.<sup>5</sup> This relation is *a priori* not expected since the SW effect has been attributed<sup>5-7</sup> previously to the local breaking of "weak" Si-Si bonds. Following recent experimental findings, suggestions were made that the SW effect yields changes beyond the short-range (nearest-neighbor) order (SRO) of the atomic network.<sup>7-9</sup> While experiments<sup>9</sup> have not shown that such a change takes place in *a*-Si, they have shown that quite a significant change takes place in *a*-Si:H. Thus, the question of the importance of hydrogen in the determination of network order, in particular, intermediate-range (beyond nearest-neighbor) order (IRO) in *a*-Si:H became of wide interest.

The main tool for the characterization of the degree of order of the atomic structure in *a*-Si:H has been Raman scattering spectroscopy. It is quite generally accepted<sup>1,3,10-14</sup> that in *a*-Si and *a*-Si:H the features of the Raman spectrum that are associated with the crystalline silicon transverse-optical (TO) vibration mode reflect the degree of the SRO.<sup>10,11</sup> The lower the peak position of this spectral band,  $\omega_{TO}$ , and the larger its width,  $\Gamma_{TO}$ , the lower the SRO. On the other hand, the transverse acoustic (TA) mode that involves triads of atoms is associated with bond bending.<sup>3,14</sup> Correspondingly, the area under the TA spectral band  $I_{TA}$ , is considered to be proportional to the density of dihedral angle fluctuations,<sup>3,12,13</sup> i.e., to the IRO in the silicon network.<sup>11,13,14</sup> For the experimental normalization of the latter quantity, one uses<sup>3,12,13</sup> the area of the TO spectral band  $I_{TO}$ , which represents the density of the nearest-neighbor bond-angle fluctuations.<sup>10,11,14</sup>

Turning to the effect of hydrogen on the above three

features, one would expect that the higher the deposition temperature  $T_S$ , the higher the degree of order in the network. This is because the system can relax from its metastable state to a lower-energy state that is closer to the ordered crystalline-like state. Indeed, for *a*-Si films, it has been found<sup>12,15</sup> that both  $\Gamma_{TO}$  and  $I_{TA}/I_{TO}$  decrease with increasing  $T_S$ . In *a*-Si:H we have, however, in addition, the effect of the hydrogen content  $C_H$ , which decreases with the increase of  $T_S$ . Maley and Lannin<sup>3</sup> found that both the  $\Gamma_{TO}$  and  $I_{TA}/I_{TO}$  features decrease with  $C_H$ . They suggested that the decrease in atomic network order with decreasing  $C_H$  (which follows the increase of  $T_S$ , hereafter, the "H role") offsets the increase of this order due to the above thermal relaxation effect (hereafter the "T role"). While the same behavior was found in some studies,<sup>9,12</sup> the reverse behavior has been found in others.<sup>15,16</sup> Our own comprehensive study<sup>17</sup> on samples deposited by glow-discharge and sputtering techniques has shown a very small effect of  $T_S$  on both the SRO and the IRO. These results could be interpreted as caused by a delicate balance between the above two "roles."

The above interpretation appears, however, very unsatisfactory when one considers the results reported<sup>18</sup> for materials prepared by the "hot-wire" technique.<sup>19,20</sup> In these materials,  $C_H$  varies by about two orders of magnitude (20–0.2 at. % of hydrogen) when  $T_S$  is raised from 50 to 550 °C. This makes these materials excellent candidates for the study of the H role in the atomic network order. In sharp contrast with indications from transport measurements,<sup>21</sup> the earlier conclusion<sup>3</sup> and the theoretical expectations,<sup>22</sup> the Raman spectra<sup>18</sup> reported for these materials have hardly shown any change in  $\Gamma_{TO}$ , as a function of  $T_S$ , in spite of the large change in  $C_H$ . (The  $\omega_{TO}$  and the  $I_{TA}/I_{TO}$  features have not been reported.) Moreover, results of x-ray diffraction measurements have been interpreted<sup>18</sup> to indicate the increase of IRO with  $T_S$  in the "hot-wire" materials (see below).

Following this rather puzzling behavior, we have carried out a comprehensive Raman scattering study of the "hot-wire" materials. These materials that are very interesting in their own right,<sup>19,21,23</sup> exhibit a "weaker" SW degradation than the conventional "glow-discharge materials."

<sup>a)</sup>Corresponding author. Electronic mail: Balberg@vms.huji.ac.il

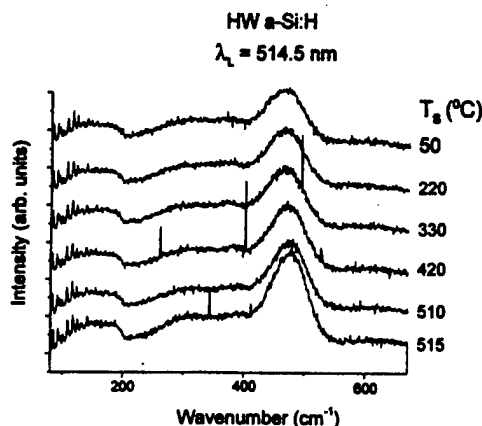


FIG. 1. Raman spectra of films prepared by the hot-wire technique as determined by using an excitation source of light wavelength of 514.5 nm. The samples differ by the substrate temperature  $T_S$  at which they were deposited.

The series of "hot-wire" films used here was deposited and characterized (especially for their hydrogen content<sup>19,20</sup>) in the same laboratory at which the previous Raman scattering studies were carried out.<sup>18</sup> Applying the micro-Raman technique and data analysis of our previous studies<sup>17,24</sup> of *a*-Si:H, we repeated first the previous measurements<sup>18</sup> using the standard 514.5-nm-wavelength illumination of an Ar<sup>+</sup>-ion laser as the excitation source.

The spectra obtained are shown in Fig. 1. In these spectra the "TO band" (around 480 cm<sup>-1</sup>) and the "TA band" (around 160 cm<sup>-1</sup>) are the conspicuous features of the data. The results of the analysis of the spectra shown in Fig. 1 are presented in Fig. 2. It is seen that there is a slight decrease of  $\Gamma_{TO}$  [Fig. 2(a)], an increase in  $\omega_{TO}$  [Fig. 2(b)], and a decrease of  $I_{TA}/I_{TO}$  [Fig. 2(c)] with  $T_S$ . In order to emphasize the relation between  $\Gamma_{TO}$  and the SRO, we have added in Fig. 2(a) the rms bond-angle deviations as suggested in Refs. 10 and 11. All these data indicate the dominance of the "T role" over the "H role," confirming the previous data<sup>18</sup> and

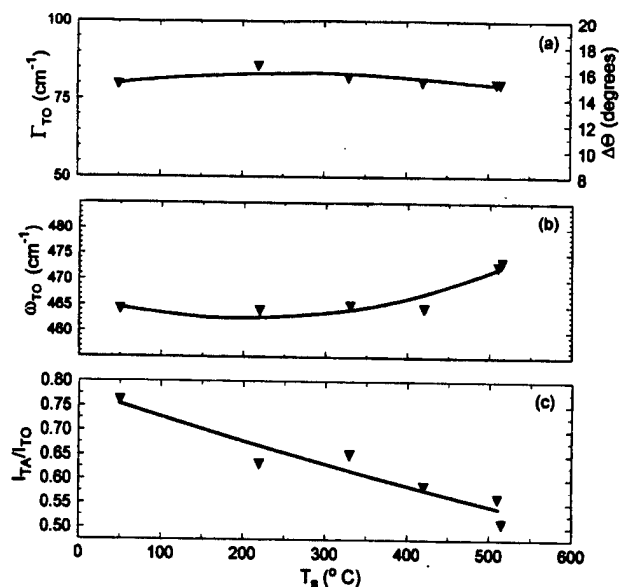


FIG. 2. Dependence of the main features of the Raman spectra on the substrate temperature at deposition  $T_S$  as derived from the data shown in Fig. 1.

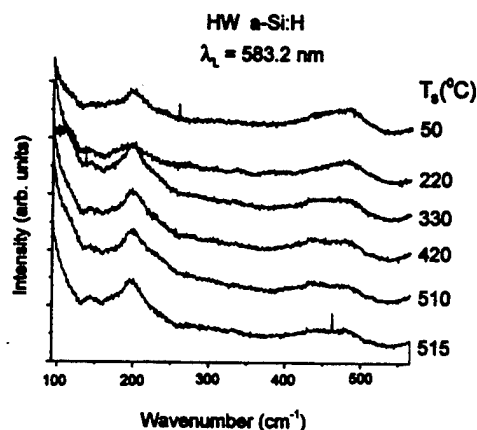


FIG. 3. Raman spectra of films prepared by the hot-wire technique as determined by using an excitation source of light wavelength of 583.2 nm. The samples differ by the substrate temperature  $T_S$  at which they were deposited.

leaving us with the above "puzzle" of the minute "H role" in spite of the large change in  $C_H$ .

We found a plausible clue to this puzzle noting that  $C_H$  near the surface of "hot-wire films" is higher than in the bulk, and that the surface is weakly effected by the out-diffusion of the hydrogen during the deposition process.<sup>20</sup> Since the 514.5 nm radiation is absorbed within 50 nm, it seemed to us reasonable to explain all the above results as reflecting the network disorder at the films' surface, where the  $C_H$  is varied, only by a factor of 2 (Ref. 20) throughout the wide  $T_S$  range employed in this study. Hence, we conjectured that the large  $C_H$  variation with  $T_S$  is a *bulk* effect that *could not* have been probed by the present and previous<sup>18</sup> Raman studies, which utilized the 514.5 nm laser light.

To test this conjecture we have repeated our measurements but with a laser light of a wavelength of 583.2 nm. At this wavelength the absorption depth is 300 nm. Noting that the samples' thickness is of the order of 1  $\mu$ m, the observed behavior can be considered to be associated with the *bulk* of the film. Furthermore, we note that this depth is much beyond the range where the  $C_H$  gradient takes place.<sup>20</sup>

For obtaining the 583.2 nm radiation, we have employed a dye laser (CR-599, rhodamine 6G) pumped by an Ar<sup>+</sup>-ion laser.<sup>17</sup> The spectra obtained with this "bulk probe" are shown in Fig. 3, and the analyzed  $T_S$  dependence of the main spectral features is presented in Fig. 4. Considering the above discussion, both Figs. 4(a) and 4(b) indicate an overall decrease in the SRO with increasing  $T_S$ . Similarly, Fig. 4(c) indicates a decrease of the IRO with increasing  $T_S$  (decreasing  $C_H$ ). The latter effect is significantly stronger in comparison with the one found in *a*-Si:H materials, which were deposited by other techniques.<sup>17</sup> Furthermore, the  $I_{TA}/I_{TO}$  ratios observed for the higher  $T_S$  (smaller  $C_H$ ) values are *larger than any ratio ever encountered before in a-Si and a-Si:H*. All the above results show then a clear domination of the "H role" over the "T role" when the variation in  $C_H$  is large. We can reconcile our conclusion with the x-ray diffraction results<sup>18</sup> (see above), that also sample the bulk of the material, by noting that such results have been attributed previously<sup>25</sup> to the SRO parameter that is manifested in the Raman spectrum by  $\Gamma_{TO}$ . If we adopt the latter interpreta-

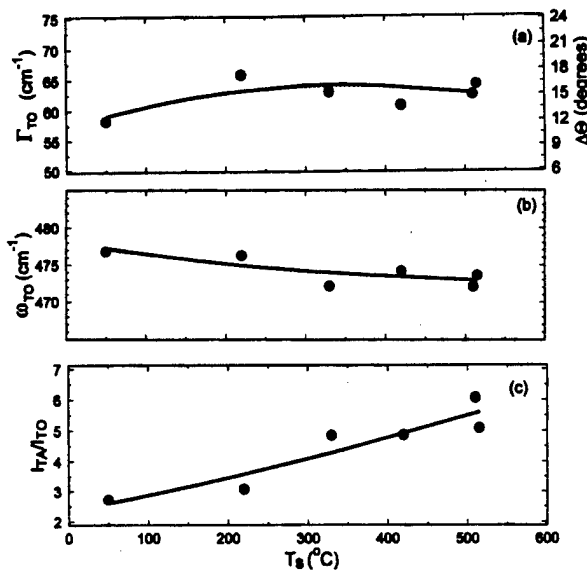


FIG. 4. Dependence of the main features of the Raman spectra on the substrate temperature at deposition  $T_S$  as derived from the data shown in Fig. 3.

tion, we get a consistent picture of the x-ray data and our data as shown in Fig. 4(a), i.e., that for the same  $T_S$  range (200–400 C) the SRO is slightly increasing with  $T_S$ .

The above solution of the “hot-wire” puzzle justifies then the physical interpretation of Maley and Lannin<sup>3</sup> showing that the effect of hydrogen is much stronger on the number of bond-bending mode fluctuations than on the number of bond-angle mode fluctuations. In addition, the present study solves the problem of the contradicting reports in the literature since it shows that *all the previously reported results* obtained by using the common 514.5 nm laser line are associated with the “surface” of *a*-Si:H, and that the attempts to correlate them with defect concentration and transport in the bulk should be examined with care.

Our results are also a further confirmation of our general conclusion<sup>26</sup> that in *a*-Si:H there is always a “surface” (a few tens of nm thick) layer, which has a lower SRO and IRO than the “bulk.” However, we can add now that once  $C_H$  is significantly different in them, as in the “hot-wire” materials, *the reverse may occur*.

In summary, we have established experimentally that hydrogen causes a relaxation of the atomic network in *a*-Si:H and that this effect is much more apparent for the intermediate-range order than for the short-range order. This reconfirmation resolves the seemingly contradicting available data as follows. It appears that, quite generally, the surface has a near-constant  $C_H$ , and thus, the degree of its order is determined by the temperature-induced network relaxation. Since in the bulk the value of  $C_H$  depends strongly on the deposition conditions, the role of hydrogen on the net-

work disorder is much more pronounced. It is expected then that intermediate-range-order effects in the network (as has been suggested for the SW effect) are associated with the presence of hydrogen.

The authors are indebted to A. H. Mahan for the samples used in this study. This work was supported by the Enrique Berman, Solar Energy Fund, by U.S.-NSF Grant No. NSF-OSR 9452893 and by Army Research Office Grant No. DAAH04-96-1-0405.

- <sup>1</sup>S. R. Elliott, *Physics of Amorphous Materials* (Longman, Essex, 1990).
- <sup>2</sup>See, for example, A. Aljishi, J. D. Cohen, S. Jin, and L. Ley, *Phys. Rev. Lett.* **64**, 2811 (1990).
- <sup>3</sup>N. Maley and J. S. Lannin, *Phys. Rev. B* **36**, 1146 (1987).
- <sup>4</sup>P. A. Fedders, Y. Fu, and D. A. Drabold, *Phys. Rev. Lett.* **68**, 1888 (1992); H. M. Branz, *Solid State Commun.* **105**, 387 (1998); R. Biswas and B. C. Pan, *Appl. Phys. Lett.* **72**, 371 (1998).
- <sup>5</sup>See, for example, P. V. Santos, N. M. Johnson, and R. A. Street, *Phys. Rev. Lett.* **67**, 2686 (1991).
- <sup>6</sup>H. Dersch, J. Stuke, and J. Beichler, *Appl. Phys. Lett.* **38**, 456 (1980).
- <sup>7</sup>For a review, see H. Fritzsche, *Mater. Res. Soc. Symp. Proc.* **467**, 19 (1997).
- <sup>8</sup>See also, for example, J. Fan and J. Kakalios, *Phys. Rev. B* **47**, 10903 (1993); D. P. Masson, A. Ouhlal, and A. Yelon, *J. Non-Cryst. Solids* **190**, 151 (1995).
- <sup>9</sup>J. M. Gibson, M. M. J. Treacy, P. M. Voiles, H.-C. Jin, and J. R. Abelson, *Appl. Phys. Lett.* **73**, 3093 (1998); *Mater. Res. Soc. Symp. Proc.* **507**, 837 (1998).
- <sup>10</sup>D. Beeman, R. Tsu, and M. F. Thorpe, *Phys. Rev. B* **32**, 874 (1985).
- <sup>11</sup>R. Tsu, M. A. Paesler, and D. Sayers, *J. Non-Cryst. Solids* **114**, 199 (1989).
- <sup>12</sup>A. P. Sokolov, A. P. Shebanin, O. A. Golikova, and M. M. Mezdrogina, *J. Non-Cryst. Solids* **137&138**, 99 (1991), and references therein.
- <sup>13</sup>J. Fortner and J. S. Lannin, *Phys. Rev. B* **37**, 10154 (1988); **39**, 5527 (1989).
- <sup>14</sup>M. Marinov and N. Zotov, *Phys. Rev. B* **55**, 2938 (1997).
- <sup>15</sup>Y. Hishikawa, K. Watanabe, S. Tsuda, M. Ohnishi, and Y. Kuwana, *Jpn. J. Appl. Phys., Part 1* **24**, 385 (1985).
- <sup>16</sup>A. J. M. Bernitsen, M. J. van der Boogaard, W. G. H. M. van Sark, and W. F. van der Weg, *Mater. Res. Soc. Symp. Proc.* **258**, 275 (1992).
- <sup>17</sup>G. Morell, R. S. Katiyar, S. Z. Weisz, H. Jia, J. Shinar, and I. Balberg, *J. Appl. Phys.* **78**, 5120 (1995).
- <sup>18</sup>A. H. Mahan, B. P. Nelson, S. Salamon, and R. S. Crandall, *Mater. Res. Soc. Symp. Proc.* **219**, 673 (1991); A. H. Mahan, D. L. Williamson, and T. E. Furtak, *ibid.* **467**, 657 (1997); D. L. Williamson, *ibid.* (in press).
- <sup>19</sup>A. H. Mahan, J. Carapella, B. P. Nelson, R. S. Crandall, and I. Balberg, *J. Appl. Phys.* **69**, 6728 (1991).
- <sup>20</sup>T. Unold, R. C. Reedy, and A. H. Mahan, *J. Non-Cryst. Solids* **227-230**, 362 (1998).
- <sup>21</sup>G. M. Khera, J. Kakalios, Q. Wang, and E. Iwaniczko, *Mater. Res. Soc. Symp. Proc.* **420**, 641 (1996).
- <sup>22</sup>I. Robertson, *Philos. Mag. B* **66**, 615 (1992).
- <sup>23</sup>D. Kwon, J. D. Cohen, B. P. Nelson, and E. Iwaniczko, *Mater. Res. Soc. Symp. Proc.* **377**, 301 (1995).
- <sup>24</sup>G. Morell, R. S. Katiyar, S. Z. Weisz, and I. Balberg, *J. Non-Cryst. Solids* **194**, 78 (1996).
- <sup>25</sup>D. Adler, in *Physical Properties of Amorphous Materials*, edited by D. Adler, B. B. Schwartz, and M. C. Steele (Plenum, New York, 1985), p. 10.
- <sup>26</sup>I. Balberg, Y. Goldstein, and A. Many, in *Solid State Phenomena: Hydrogenated Amorphous Silicon*, edited by H. Neber-Aeschbacher (Scitech, Zug, 1995), Vols. 44–46, p. 791.



ELSEVIER

Journal of Non-Crystalline Solids 266–269 (2000) 496–500

JOURNAL OF  
NON-CRYSTALLINE SOLIDS

www.elsevier.com/locate/jnoncrysol

# The effect of light soaking on the structural order in a-Si:H

S. Gupta<sup>a</sup>, R.S. Katiyar<sup>a</sup>, S.Z. Weisz<sup>a</sup>, I. Balberg<sup>b,\*</sup>

<sup>a</sup> Department of Physics, University of Puerto Rico, San Juan 00931, Puerto Rico

<sup>b</sup> The Racah Institute of Physics, The Hebrew University, 91904 Jerusalem, Israel

## Abstract

Following conflicting reports concerning the effect of light soaking (LS) on the structure of hydrogenated amorphous silicon (a-Si:H) we have carried out a comprehensive Raman scattering study of this effect on a-Si:H films prepared by different deposition techniques. We have found that first, the LS causes a major rearrangement of atoms as suggested by recent theoretical models. Second, the short-range order decreases upon LS as we expect from the breaking of Si-Si bonds. Third and counterintuitive, the intermediate range order may increase upon LS. © 2000 Elsevier Science B.V. All rights reserved.

## 1. Introduction

The effect of illumination induced degradation on the electronic properties of amorphous semiconductors, known as the Staebler–Wronski (SW) effect, has been a subject of study in the last 20 years [1,2]. In spite of its importance for understanding the covalent-amorphous system and in spite of its relevance to opto-electronic applications, it is still poorly understood and hardly controlled. While the recovery of the SW effect by annealing indicates that the effect is associated with a modification of the covalent amorphous network, the consideration of the structural mechanism underlying the SW effect has become a subject of interest only in the last few years [3]. In contrast with the traditional models of the SW effect that were concerned with the single dangling bond and its nearest neighbors, there is now ex-

perimental evidence [4–12], supported by theoretical calculations [13,14], that indicates that the SW effect is a global effect. This effect is a result of a reorganization of the network, which follows the carrier excitation and/or recombination.

While the very fact that this reorganization of the atomic network appears now to be a fundamental property of the SW effect, its description is still at a rudimentary level in our opinion. In fact while the theoretical predications for both unhydrogenated amorphous silicon (a-Si) and hydrogenated amorphous silicon (a-Si:H) have dealt with this reorganization, they did not address explicitly the question of the order. We note however that recent theoretical calculations [4,5,14] of the SW effect have implied the (intuitively expected) increase of the root mean square (rms) of the bond angle distribution, i.e., a decrease of the short-range order (SRO) upon light soaking (LS) in a-Si:H. Experimental data and variable coherence transmission electron microscopy (VC-TEM) results [15] (which do not monitor the SRO) suggested that the LS causes a decrease in the intermediate range order (IRO), i.e., the order

\* Corresponding author. Tel.: +972-2 658 5680; fax: +972-2 65 84437.

E-mail address: balberg@vms.huji.ac.il (I. Balberg).

beyond the nearest neighbor, upon the LS of a-Si:H. On the other hand, the results of the most common method to follow the degree of both SRO and IRO, i.e., the Raman scattering technique, are not conclusive. Considering that the effect of LS in one work [16] did not show a change in the features (see below) that account for the SRO and IRO, in another work [17], a decrease in the SRO (in agreement with the theoretical expectations [4,5,14]) and an *increase* in the IRO (in contrast with the VC-TEM data [15] and these expectations [4,5]) was found. In particular we note that different samples and different techniques have been used for the evaluation of this effect so that all these findings do not sum to consistent experimental results as to the effect of light soaking on the network disorder in a-Si:H. In the present work we intended to resolve this problem and to provide a consistent experimental analysis of the evolution of the disorder upon LS, by using the same technique on different a-Si:H materials.

## 2. Experimental

We have carried out our study on samples prepared by different deposition techniques and different laboratories. The first set of samples used in our study were 1  $\mu\text{m}$  thick, device quality, a-Si:H films, whose deposition has been described previously [18,19]. The substrate used for the samples was a 7059 Corning glass and the deposition technique was the dc glow discharge (GD) decomposition of silane with a substrate temperature,  $T_s$ , of 260°C. We have also reported previously [18,19] the effects of light soaking on the electronic properties of these films. These effects are similar to those well documented in the literature [1,2]. The second set of samples were prepared by the hot wire (HW) technique with thickness and substrate similar to the GD samples. For this set we have examined samples prepared with varying substrate temperatures,  $T_s$ . Again, we have reported the deposition, the electronic properties and the effect of LS on these properties previously [20,21].

The micro-Raman set-up and the measurement procedure and data analysis used in the present

study have been described [22,23]. The 514.5 nm laser illumination was obtained from an Ar-ion laser. For the present measurements, however, the power of the incident radiation was 7.5 mW, the beam diameter was 5  $\mu\text{m}$  and the measurement was carried out for 300 s to avoid, as much as possible, the light soaking by the 'Raman-probe' beam. The controlled light soaking was carried out using a (100 W Oriel Q) lamp with a broad band quartz fiber optics under a power of 400 mW/cm<sup>2</sup>. This illumination was applied for 2 h. The measurements and light soaking were carried out at room temperature (300 K) and at liquid nitrogen temperature (70 K). The properties found were much the same at both temperatures.

## 3. Experimental results

Turning to the results of our measurements we show in Fig. 1 the Raman spectra obtained before and after light soaking at 70 K for a GD sample. Similar data were obtained at 300 K and for the HW samples. We note, as is common in the

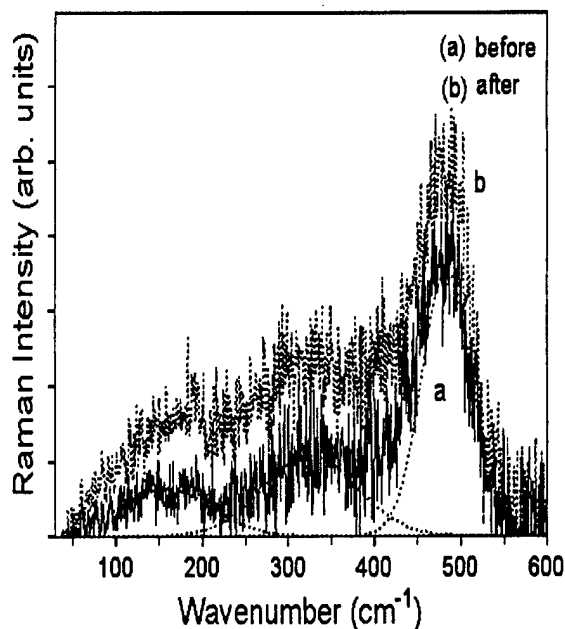


Fig. 1. The Raman spectra of a sample of the GD set before (a) and after (b) light soaking.

Raman spectrum [22-24] of a-Si:H and a-Si, two features, the one around  $480\text{ cm}^{-1}$  which is known as the TO band and is associated with the c-Si transverse optical (TO) mode and a band around about  $150\text{ cm}^{-1}$ , known as the TA band which is associated with c-Si transverse acoustic (TA) mode [22-24]. Due to the illumination intensity used, the spectra are noisier than usual and the Ar laser plasma lines are detected sometimes. For the present study the important observations are, however, the changes that take place in these spectral bands upon light soaking. We note that the broadening of the above spectral bands takes place when exposed to light. On the other hand, the fact that the integrated intensity of the TA spectral band ( $I_{\text{TA}}$ ) increases with respect to the integrated intensity of the TO spectral band ( $I_{\text{TO}}$ ), upon light soaking, is more subtle (and as in Ref. [16] hardly observable). This ratio requires then the more quantitative analysis to be presented below.

Based on the above-mentioned spectral bands, it is very well established that the linewidth of the TO band,  $\Gamma_{\text{TO}}$ , is representative of the rms of the bond-angle distribution of the network [16,17,22-24]. Similarly, the shift of the peak position of the TO spectral band,  $\omega_{\text{TO}}$ , to lower frequencies is associated with the increase in the average bond-length compared to that of crystalline silicon [22-24]. Hence, the larger the  $\Gamma_{\text{TO}}$  and the smaller the  $\omega_{\text{TO}}$ , (with respect to the c-Si,  $521\text{ cm}^{-1}$ , band), the smaller the SRO, i.e., the larger the departure of the nearest neighbor arrangement from that of the ideal (c-Si) tetrahedron. Based on the acoustic properties of the TA (bond bending) mode, it is associated with a vibration that extends further than the nearest neighbor. Indeed, it is quite well established [22-24] that the  $I_{\text{TA}}$  is affected by the concentration of the dihedral angle (between adjacent silicon tetrahedrons) bending fluctuations and thus it is a measure of the IRO. Since the  $I_{\text{TO}}$  is affected by the concentration of the fluctuations of the stretching mode, it became customary [16,17,22-24] to use the  $I_{\text{TA}}/I_{\text{TO}}$  ratio as a normalized measure of the development of the IRO with respect to the SRO in a-Si and a-Si:H.

Following the above considerations we have determined (as described above) the  $\Gamma_{\text{TO}}$ s,  $\omega_{\text{TO}}$ s and  $I_{\text{TA}}/I_{\text{TO}}$ s of the spectra in Fig. 1 by applying

our analysis to the data [22,23]. In particular for the data in Fig. 1 we found before light soaking (at 70 K) that  $\Gamma_{\text{TO}} = 41.2 \pm 3.0\text{ cm}^{-1}$ ,  $\omega_{\text{TO}} = 488.4 \pm 1.6\text{ cm}^{-1}$  and  $I_{\text{TA}}/I_{\text{TO}} = 1.56 \pm 0.02$ . After light soaking we found that  $\Gamma_{\text{TO}} = 57.5 \pm 3.0$ ,  $\omega_{\text{TO}} = 489.7 \pm 2.3\text{ cm}^{-1}$  and  $I_{\text{TA}}/I_{\text{TO}} = 1.99 \pm 0.02$ . Similar results have been obtained for the other samples and at room temperature. Hence, the data are consistent with the hypothesis that both SRO and IRO decrease upon light soaking.

Our results for the SRO are consistent then with previous Raman scattering data [16,17]. On the other hand, based on the fact that an increase of  $I_{\text{TA}}/I_{\text{TO}}$  occurs with LS, we suggest that the IRO decreases due to the SW effect. This suggestion is in agreement with the results of the independent measurement of the VC-TEM [15] on other a-Si:H materials but, as mentioned above, in disagreement with the only previous results that were derived by Raman scattering measurements (again, on other a-Si:H materials [17]).

Following these results we have applied our Raman scattering measurements to a different type of sample, i.e., films prepared by the HW technique. By using the same technique and the same method of analysis we hoped to resolve the sample vs. technique question and to evaluate the effects of LS on the structural order, in particular to resolve the issue for which the contradiction is apparent, i.e., the effect of LS on the IRO. The spectra we found on the HW materials were much the same as shown in Fig. 1. The analysis of the data for the features associated with SRO (as explained above) has indicated a decrease in the SRO

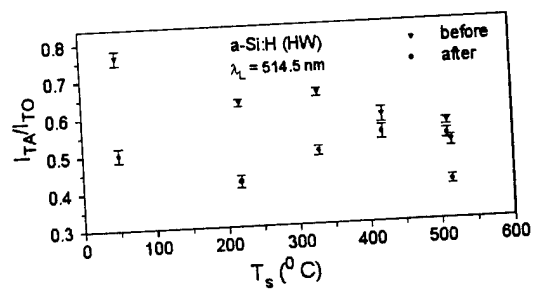


Fig. 2. The values of the Raman spectrum feature which are associated with the IRO for a few HW samples that were deposited under different substrate temperatures. These ratios are for measurements (a) before and (b) after light soaking.

upon LS in accordance with the above and the previous results [17]. This conclusion applies to all the samples ( $50 \leq T_s \leq 520^\circ\text{C}$ ) used. On the other hand, the results associated with the IRO were the opposite of those given above for the GD material. This difference is shown by the summary of the corresponding results which are presented in Fig. 2. In this figure we see a decrease of the  $I_{TA}/I_{TO}$  feature upon LS. This change as explained above, indicates the increase of the IRO with LS. We see then that in agreement with Ref. [17] the LS causes an increase in the IRO in spite of the fact that there is a decrease in the SRO.

#### 4. Discussion and conclusions

From our results we can conclude that the reorganization of the atomic network in a-Si:H, due to the SW effect, is accompanied by the decrease in the SRO and a change in the IRO. The observed opposite directions of this change have to do with the more subtle properties of the material under study. This conclusion explains then that the differences between previous results are due to the differences in the materials and not to the difference in the experimental techniques and their interpretation.

The above conclusion on the two possible properties of the IRO in a-Si:H has to be considered when models of the SW effect are proposed. In particular the simultaneous decrease of the SRO, with the possible increase or decrease of the IRO, has to be accounted for in any future model of the SW effect. The changes in SRO are expected due to the fact that the weak Si–Si bond, or the Si–H bond, retain the similarity to the c-Si tetrahedral configuration better than a Si atom with a dangling band. On the other hand, the fact that the IRO change does not follow the SRO change indicates that the atomic network rearrangement that follows is not trivial. Tentatively, we explain these changes by a competition of two effects. The first is that the breaking of bonds is also the breaking of dihedral bonds. This effect will decrease the correlation between adjacent tetrahedra and thus produce a decrease of the IRO. On the other hand, the breaking of the weaker bonds can

be followed by a relaxation of the network in the environment of the broken bond. If the network is not relaxed the breaking of bonds by the LS, which is manifested by the decrease of the SRO, may lead to a more relaxed network. If this effect overcomes the decrease in the correlation, the end result will be an increase in the IRO. On the other hand, if the network is a priori more relaxed, the decrease in the correlation will dominate and an overall decrease of the IRO will follow. An independent check of this suggestion can be made by various studies. For example a study of the valence-band tail width in materials that show different effects of LS on the IRO is called for since it is expected that a wider tail is associated with a less relaxed network.

#### Acknowledgements

The authors thank R.R. Arya, M. Keane and A.H. Mahan for the samples used in this study. This work was supported in part by the Enrique Berman Solar Energy Research Fund and in parts by the NSF-EPSCoR Grant No. GSR-94-52893 and DMR-98-01759.

#### References

- [1] H. Fritzsche, Mater. Res. Soc. Symp. Proc. 467 (1997) 19.
- [2] M. Stutzmann, Mater. Res. Soc. Symp. Proc. 467 (1997) 37.
- [3] H. Fritzsche, Solid State Commun. 94 (1995) 953.
- [4] K. Shimizu, et al., Mater. Res. Soc. Symp. Proc. 507 (1998) 735.
- [5] K. Shimizu, et al., Jpn. J. Appl. Phys. 36 (1997) 29.
- [6] K. Guanglin, et al., Phys. Res. Lett. 79 (1997) 4210.
- [7] B. Pashmakor, H. Fritzsche, Phys. Rev. Lett. 80 (1998) 5704.
- [8] R.E. Norberg, et al., Mater. Res. Soc. Symp. Proc. 258 (1992) 377.
- [9] R.E. Norberg, et al., J. Non Cryst. Solids 190 (1991) 71.
- [10] I.A. Popov, Semiconductors 30 (1994) 258.
- [11] D.P. Masson, A. Ouklal, A. Yelon, J. Non-Cryst. Solids 190 (1991) 151.
- [12] G.L. Kong, et al., Mater. Res. Soc. Symp. Proc. 507 (1998) 697.
- [13] P.A. Fedders, Y. Fu, D.A. Drabold, Phys. Rev. Lett. 68 (1992) 1888.
- [14] R. Biswas, Y.-P. Li, Phys. Rev. Lett. 82 (1999) 2512.





ELSEVIER

Journal of Luminescence 83–84 (1999) 187–191

JOURNAL OF  
LUMINESCENCE

www.elsevier.com/locate/jlumin

## Size-dependent optical properties of silicon nanocrystals

R.K. Soni\*, L.F. Fonseca, O. Resto, M. Buzaianu, S.Z. Weisz

*Department of Physics, University of Puerto Rico, P.O. Box 23343, Rio Piedras, PR 00931, USA*

### Abstract

We have synthesized green and red luminescent silicon nanocrystals in a  $\text{SiO}_2$  matrix by RF co-sputtering on a quartz substrate. The transmission coefficient measurements were used to estimate the nanocrystal size distribution. The size distribution reveals peaks in the range 1.1–2.6 nm with a long tail towards the larger size. As the nanocrystal size reduces photoluminescence spectrum shifts from red to green wavelengths. The measured PL emission energy is in agreement with the corrected LDA calculations. With decreasing nanocrystal size, the phonon Raman spectra exhibit softening accompanied with increasing asymmetrical broadening. The observed line shape is explained by considering phonon confinement in a spherical nanocrystal. The major contribution to the phonon line shape comes from those nanocrystals that favor resonance interaction with either incoming or outgoing photon. © 1999 Elsevier Science B.V. All rights reserved.

**Keywords:** Silicon nanocrystals; Si– $\text{SiO}_2$  film; Photoluminescence; Raman scattering; Quantum confinement

### 1. Introduction

Nanometer size silicon crystals show marked improvement in photoluminescence (PL) quantum efficiency compared to bulk silicon and are, therefore, attractive for silicon based optoelectronic applications [1]. The PL observed from Si nanocrystals is attributed to quantum size effects. The effect of carrier confinement and band gap upshift in silicon nanocrystals has been discussed intensively in the literature [1]. The photoluminescence energy for silicon nanocrystals have been calculated by using the empirical pseudopotentials (EPS) [2], the third-nearest-neighbor tight binding [3] and time-dependent tight binding techniques [4]. Despite the

apparent disagreement in predicting the PL emission energies, these calculations demonstrate that the PL energy increases as the nanocrystal size decreases and the dominant contribution to the visible light emission comes from nanocrystals smaller than 2 nm. The resonantly excited PL spectrum has shown long radiative lifetime in the Si nanocrystals and provides an important evidence that the phonons are directly involved in the radiative recombination process [5]. Clearly, this suggests that the Si nanocrystal electronic band structure remains indirect type. Theoretical calculations, however, indicate that quasi-direct gap in nanocrystal silicon is possible for sizes 1.0–1.5 nm in diameter [3].

Raman scattering technique is commonly used for semiquantitative determination of size effects on vibrational modes, such as confined optical phonon, surface phonon and confined acoustic

\* Corresponding author. Fax: + 1-787-764-9006.

E-mail address: rksoni@rrpac.upr.clu.edu (R.K. Soni)

phonon, in nanocrystals [6-9]. An adequate knowledge of the bulk phonon dispersion is a prerequisite for understanding lattice dynamical properties and electron-phonon interactions in nanocrystals. The effect of carrier confinement on optical phonons in silicon nanoparticles has been widely studied by Raman scattering [6-8]. The size effect is reflected in a finite wave vector of nanocrystal and corresponding lowering of phonon frequency from those of the bulk. A quantum confinement model that takes into account the finite phonon wave vector and Gaussian size distribution for spherical nanocrystals is generally invoked to explain the observed Raman line shape. Here, we investigate the size-dependent photoluminescence and Raman scattering from silicon nanocrystals dispersed in a  $\text{SiO}_2$  matrix grown on a quartz substrate. We emphasize the role of nanocrystals that favor the resonant interaction with incoming or outgoing photon.

## 2. Experiment

The Si- $\text{SiO}_2$  film was synthesized on the quartz substrate by RF co-sputtering. The substrate was a 6-in long quartz strip. The chamber was first evacuated down to  $1.0 \times 10^{-7}$  Torr and the deposition was performed under an argon pressure of  $2.0 \times 10^{-2}$  Torr at deposition temperature of  $115^\circ\text{C}$ . On a  $\text{SiO}_2$  target (6 in in diameter) small pieces of Si tips (area  $\sim 0.1 \text{ in}^2$ ) were placed and they were co-sputtered for 3 h. The number of Si tips and their position on the  $\text{SiO}_2$  were used to control the size of silicon nanoparticles. The film was subsequently annealed in nitrogen ambient at  $1100^\circ\text{C}$  for 30 min. The deposited film has an area of  $5 \times 0.2 \text{ in}$  and thickness of the order of  $1.7 \mu\text{m}$ . Both the size and density of silicon nanocrystals vary continuously along the length of the film. The transmission measurements were made in the range 190-820 nm using a HP-8452A spectrophotometer. The photoluminescence and Raman measurements were performed in a quasi back-scattering geometry at room temperature using the 514.5 nm line of an  $\text{Ar}^+$  laser. The spectra were dispersed by a TRIAX 320 spectrometer and detected by a cooled photomultiplier with GaAs photocathode.

## 3. Results

Fig. 1 shows typical transmission spectra taken from different positions on the Si- $\text{SiO}_2$  film. The deposited film is divided in 50 equal segments and designated a number, number 1 is assigned to  $\text{SiO}_2$  rich end and 50 to the Si rich end of the film. Each of these segments has different nanocrystal density and size. In order to study the size dependence of optical properties, we measured the transmission spectrum from each one of these segments. The optical absorption edge shifts to higher energy as one moves from silicon rich side (position 50) to  $\text{SiO}_2$  rich side (position 1) of the sample due to nanocrystal size reduction. The transmission coefficient of the film is related to the energy absorbed by the Si nanocrystal of size  $R$  imbedded in the  $\text{SiO}_2$  matrix. Assuming that the energy upshift is given by  $A/R^{1.3}$  ( $A$  is a constant), and the absorption is primarily due to interband transitions between the quantum confined states of spherical Si nanocrystals, the size distribution can be

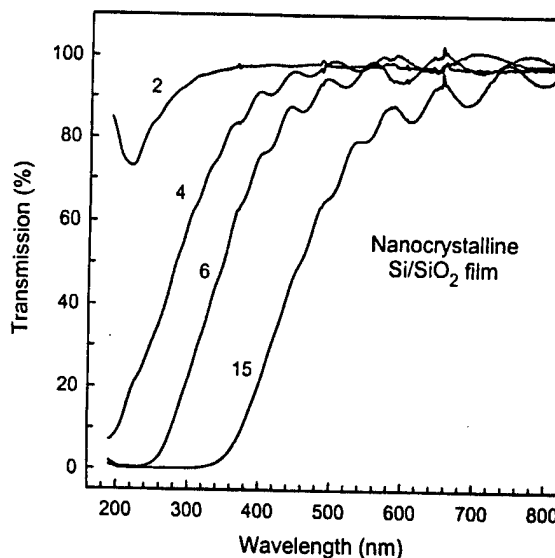


Fig. 1. Transmission spectra from different positions of a Si- $\text{SiO}_2$  film annealed at  $1100^\circ\text{C}$ . The film is divided in 50 equal segments; the number on each spectrum designates the segment number. The number 1 and 50 are assigned to the  $\text{SiO}_2$  rich and Si rich end of the film, respectively. The absorption edge shifts to lower wavelengths with decreasing silicon nanocrystal size and density.

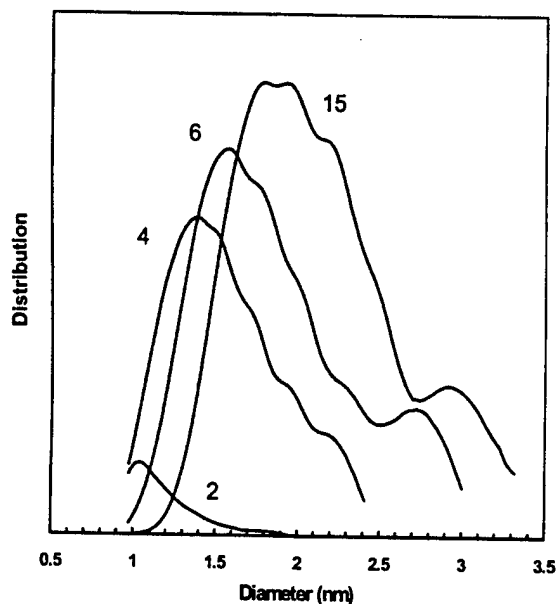


Fig. 2. Calculated nanocrystal size distribution in Si-SiO<sub>2</sub> films annealed at 1100°C at the positions where transmission spectra were taken. The size distribution is narrower for smaller sizes.

approximated with the first derivative of the transmission spectrum [10]. We have used the transmission measurements to estimate the nanocrystal size distribution in the film, the estimated size distribution is asymmetric with a long tail towards the larger size and centered around 1.1–2.6 nm as shown in Fig. 2.

Fig. 3 shows the PL emission spectra from Si-SiO<sub>2</sub> film excited with the green 514.5 nm (2.412 eV) line of an argon ion laser. The PL spectrum is broad and shifts to higher energy with decreasing size. In addition, there is a large reduction in integrated PL intensity for smaller sizes due to lower density. The peaks are observed at 782 nm (1.59 eV) and 601 nm (2.06 eV) for dot sizes of 2.6 and 1.4 nm, respectively. According to Delerue et al. [11], EPS or tight binding as well as corrected *ab initio* local density approximation (LDA) techniques give reliable predictions for Si nanocrystal band gap. It has also been pointed out that the quasi particle gaps and exciton coulomb energies of Si nanocrystals require a large correction to the band gap which are not included in the one electron theory. The exciton gap is defined as

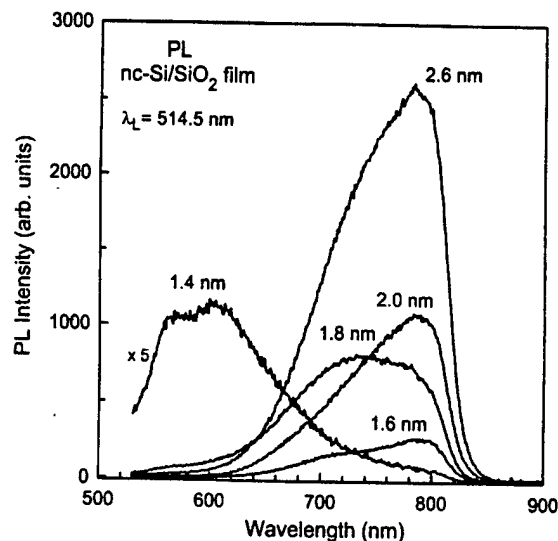


Fig. 3. Size-dependent PL spectra from silicon nanocrystals embedded in SiO<sub>2</sub>. The average size of the nanocrystal is calculated from the transmission data.

$E_{\text{exc}}^{\text{exc}} = E_{\text{g}}^{\text{QP}} - E_{\text{coul}}$ , where the quasi-particle gap  $E_{\text{g}}^{\text{QP}}$  is the difference in energies resulting from the separate addition of an electron and hole to the system while the correction  $E_{\text{coul}}$  results from the corresponding attraction between these two quasi-particles. Our PL results are in agreement with corrected LDA calculation [11]. We attribute the featureless broad PL spectrum to band-to-band recombination in Si nanocrystal and fluctuation in their sizes. For the 1.4 nm nanocrystal, we also see structure towards the high energy (2.2 eV) due to resonant excitation with laser line. It should be noted that PL energy is lower than the absorption edge at each segment of the film, and this difference is appreciably large towards the SiO<sub>2</sub> side of the film where the nanoparticle sizes are smaller. Self-trapped exciton at the interface between Si and SiO<sub>2</sub> or a defect state is considered to be responsible for the observed Stokes shift of PL emission energy [11].

The Raman spectra from Si-SiO<sub>2</sub> film were excited with 514.5 nm (2.41 eV) laser line of an argon ion laser from the region that emits green-orange luminescence. Fig. 4 shows representative spectra from three different positions of the sample characterized by the average nanocrystal diameter. The

observed spectra show phonon softening and line shape broadening with decreasing size. As the size decreases from 2.2 to 1.4 nm, the Raman peak shifts from 511 to 502  $\text{cm}^{-1}$ . The Raman lines are asymmetrically broadened with a tail towards the low-energy side. In the uncorrected data, the integrated intensity remains fairly constant. The broad line shape arises from size distribution in an ensemble of nanocrystals, which leads to a large fluctuation in wave vectors, particularly for size smaller than 2 nm.

In order to explain the observed resonance line shape, we assume that the optical vibrations are confined to the spherical nanocrystal with effective wave vector,

$$q_n = \frac{\mu_n}{R}, \quad (1)$$

where  $\mu_n$  is  $n$ th node of the spherical Bessel function  $j_1$ , and  $R$  is the nanocrystal radius. A quadratic bulk Si dispersion gives the eigen frequencies,

$$\omega_n^2(R) = \omega_0^2 - \beta^2 q_n^2(R), \quad (2)$$

where  $\omega_0$  is the bulk silicon optical phonon frequency ( $520.5 \text{ cm}^{-1}$ ) and  $\beta$  is a parameter ( $6.977 \times 10^{12} \text{ s}^{-1}$ ) describing the dispersion of the optical phonon in the bulk silicon. The observed Raman frequencies are in agreement with the calculated eigenfrequencies of optical vibrations of zero angular momentum ( $l = 0$ ) mode as a function of  $R$  in a spherical Si nanocrystal embedded in the  $\text{SiO}_2$ . It should be pointed out that a precise determination of nanocrystal size, particularly for  $R < 1 \text{ nm}$ , is necessary for the estimation of equivalent wave vectors and corresponding eigenfrequencies. The Raman line shape can be written as  $I(\omega, R)$  [9],

$$I(\omega_s, R) = I_0$$

$$\times \sum_n \frac{1}{[(\hbar\omega_i - E_{\mu_1}(R))(\hbar\omega_s - E_{\mu_2}(R)) - \Gamma_{\mu_1}\Gamma_{\mu_2}]^2 + [\Gamma_{\mu_2}(\hbar\omega_i - E_{\mu_1}(R)) + \Gamma_{\mu_1}(\hbar\omega_s - E_{\mu_2}(R))]^2} \\ \times \frac{\Gamma/\pi}{[\hbar\omega_i - \hbar\omega_s - \hbar\omega_n(R)]^2 + \Gamma^2}, \quad (3)$$

where  $I_0$  is the product of scattering efficiency and eigenvalues of the appropriate scattering matrix

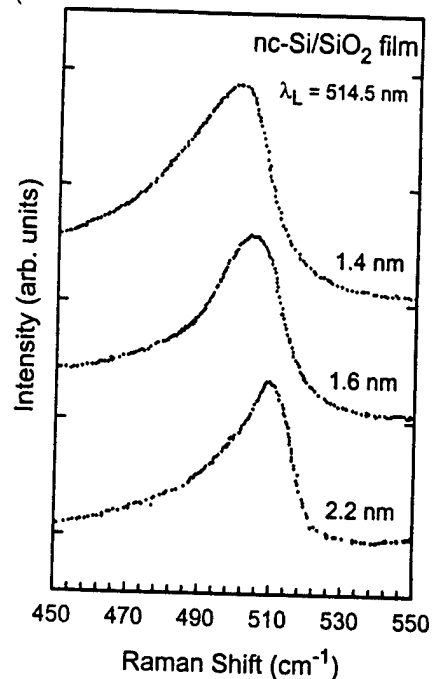


Fig. 4. Size-dependent Raman spectra from silicon nanocrystals. The average size of the nanocrystal is calculated from the transmission data.

elements over all the intermediate states,  $R$  is the mean nanocrystal radius,  $E_{\mu_1}(R)$  and  $E_{\mu_2}(R)$  are the eigenenergy for  $R$  in the  $\mu_1$  and  $\mu_2$  intermediate states, respectively,  $\Gamma_{\mu}(\Gamma)$  is the intermediate state (phonon) lifetime broadening,  $\omega_i$  and  $\omega_s$  are the excited laser energy and scattered photon energy, respectively. In the incoming resonance process,  $\omega_i$  coincides with one of the electronic states  $E_{\mu_1}(R)$  while outgoing resonance occurs when  $\omega_s$  approaches  $E_{\mu_2}$ . The resonance conditions is described as  $\hbar\omega_i = E_{\mu_1}(R)$  for incoming resonance,

and  $\hbar\omega_i - \hbar\omega_n(R) = E_{\mu_2}(R)$  for outgoing resonance. We assume that the intermediate electronic state is an electron-hole pair state and the electron-phonon couple via deformation potential

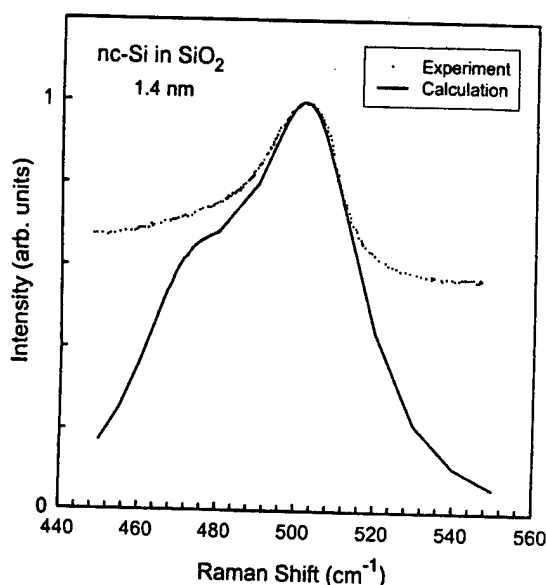


Fig. 5. Calculated resonance contribution to the experimentally observed Raman line shape of 1.4 nm silicon nanocrystal.

interaction. The resonant nanocrystals at the laser photons at 2.412 eV have diameters in the range 1.3–1.4 nm. Fig. 5 shows the calculated line shape for 1.4 nm nanocrystal. It is evident from the figure that the main contribution to the Raman line shape comes from the resonant radii, though non-resonant nanocrystals provide broad constant background to the Raman spectrum.

#### 4. Conclusions

We have synthesized Si nanocrystals in a SiO<sub>2</sub> matrix on quartz strip by RF co-sputtering. The silicon nanocrystals are dispersed in size along the length of the strip. Optical transmission measurements were employed to estimate the nanocrystal size distribution which shows peaks in the range 1.1–2.6 nm with an asymmetrical tail towards the large particle size. The PL emission from the Si-SiO<sub>2</sub> film exhibits broadband in the red and green region, and their energies are in agreement with corrected LDA calculation of Si nanocrystals.

Size dependence of the Raman scattering was performed on Si nanocrystals, the results show phonon softening and large asymmetrical broadening. With decreasing nanocrystals size, broadening increases further due to fluctuation in effective wave vector associated with size distribution. The observed Raman frequency and asymmetry was calculated by considering phonon confinement in a spherical nanocrystal. For small size, the line shape is dominated by the resonant nanocrystals that favor incoming or outgoing resonance. The electronic state responsible for the resonant interaction with nanocrystal has a large lifetime broadening of the order of 25 meV. The weak resonance enhancement seen under the resonant condition is indicative of band-to-band transitions in the Raman process.

#### Acknowledgements

Authors acknowledge partial support from US ARO grant No. DAAH04-96 and NASA grant No. NCCW-0088.

#### References

- [1] L. Tsybeskov, MRS Bulletin, April 1998, p. 33.
- [2] L.W. Wang, A. Zunger, J. Phys. Chem. 98 (1994) 2158.
- [3] C. Delerue, G. Allan, M. Lannoo, Phys. Rev. B 48 (1993) 11024.
- [4] N.A. Hill, K.B. Whaley, Phys. Rev. Lett. 75 (1995) 1130.
- [5] M. Rosenbauer, S. Finkbeiner, E. Bustarret, J. Weber, M. Stutzmann, Phys. Rev. B 51 (1995) 10 539.
- [6] H.D. Fuchs, M. Stutzmann, M.S. Brandt, M. Rousenbauer, J. Weber, A. Breitschwerdt, P. Deak, M. Cardona, Phys. Rev. B 48 (1993) 8172.
- [7] Y. Kanazawa, S. Hayashi, K. Yamamoto, J. Phys.: Condens. Matter 8 (1996) 4823.
- [8] M. Fujii, Y. Kanazawa, S. Hayashi, K. Yamamoto, Phys. Rev. B 54 (1996) R8373.
- [9] C. Trallero-Giner, A. Debernardi, M. Cardona, E. Menendez-Proupin, A.I. Ekimov, Phys. Rev. B 57 (1998) 4664.
- [10] L.F. Fonseca, O. Resto, S. Gupta, R.S. Katiyar, S.Z. Weisz, Y. Goldstein, A. Many, J. Shappir, in: Proceedings of the 24th International Conference on Physics of Semiconductor, Israel, 1998, World Scientific, Singapore, in press.
- [11] C. Delerue, G. Allan, M. Lannoo, J. Lumin. 80 (1999) 65.



ELSEVIER

Journal of Luminescence 83–84 (1999) 37–41

JOURNAL OF  
LUMINESCENCE

www.elsevier.com/locate/jlumin

## Observation of picosecond nonlinear optical response from porous silicon

Huimin Liu<sup>a,\*</sup>, Luis F. Fonseca<sup>b</sup>, S.Z. Weisz<sup>b</sup>, Weiyi Jia<sup>a</sup>, Oscar Resto<sup>b</sup>

<sup>a</sup>Department of Physics, Materials Research Center, University of Puerto Rico, Mayaguez, PR 00681, USA

<sup>b</sup>Department of Physics and Materials Research Center, University of Puerto Rico, Rio Piedras, PR 00931, USA

### Abstract

Optical quality, free standing and highly photoluminescent PSi was prepared from both, p- and n-type Si wafers using electrochemical anodization of c-Si. A broad and intense absorption band is in the UV–Visible region with a cut-off edge at  $\sim 400$  nm. A strong emission was found in the red region. At 8 K the broadband luminescence is peaked at  $\sim 670$  nm. The band maximum shifts toward low-energy side while excitation wavelength increases. The size distribution of the nanoparticles was obtained from the optical transmission data and the theoretical relation between the size of the particles and the energy gap. Nonlinear optical response measurement was also performed using degenerate four-wave-mixing (DFWM) in a backward configuration with all waves in s-polarization. The response signal consists of an instantaneous component followed by a long lived, slowly decaying component. The former is associated with the third-order susceptibility of the material whereas the latter originates from the contribution of surface states created by laser excitation. The response due to the surface state is significant, which has potential in practical applications. © 1999 Elsevier Science B.V. All rights reserved.

PACS: 42.65.Re; 78.55.Mb; 78.55. – m

Keywords: Porous silicon; Photoluminescence; Wave mixing; Optical response

### 1. Introduction

It is well known [1] that the small and indirect band gap of crystalline silicon (c-Si) is characterized by an extremely low quantum efficiency of luminescence while porous silicon (PSi), obtained by electrochemical etching of c-Si surfaces, yields extremely high photoluminescence (PL) efficiencies up to  $10^{-1}$  in the visible range [2–5]. The origin of

the PL has been the subject of many studies. We have studied the photodynamical process and Raman spectra of PSi [4,6]. It was found that S-band luminescence comes from highly confined regions with a distribution of size. Quantum confinement increases the emission energy and the oscillator strength of the radiative transition, decreasing the radiative lifetime. Therefore, the most accepted luminescence mechanism at this time is associated with quantum confinement in the nc-Si formed in the PSi by the anodization process [5]. The presence of  $\sim 3$  nm size nanocrystallites is the size required by the confinement mechanisms to enlarge the band gap. On the other hand,

\*Corresponding author. Fax: +1-787-832-1135.

E-mail address: h-liu@rumac.upr.clu.edu (H. Liu)

in nonlinear optical experiments a key parameter to be measured is the nonlinear refractive index which is related to a variety of other NLO effects through the formalism of NLO susceptibilities. To study ultrafast nonlinear optical response on the picosecond time scale plays an important role for practical NLO applications such as switching and modulation. However no study on PSi has been reported to our knowledge. In this paper we demonstrate the size-related emission property and show that the excitation is mainly localized. The localized surface state is responsible for the post-instantaneous signal.

## 2. Sample preparation

The optical quality, free standing and highly photoluminescent PSi was obtained from both, p- and n-type Si wafers using electrochemical anodization of c-Si. The key role of the holes in the etching process requires that n-type samples be illuminated during the anodization. The porosity and the final structural and optical properties of the samples can be varied by changing the acid concentration, current density, anodization time as well as the characteristics of the Si-wafer as resistivity and crystalline orientation. We prepared a Si wafer with (1 0 0) crystalline orientation and 0.5–1.5  $\Omega$  cm resistivity. Using a HF : ethanol : water (1 : 2 : 1) solution, the anodization current (200 mA/cm<sup>2</sup>) was applied in 280 steps of 0.8 s each and with resting intervals of 1.4 s between anodizations, such that a high-optical quality, free-standing porous films were obtained. The preliminary studies we have made including the determination of electronic surface states densities, electrical transport properties, optical and morphological properties as well as surface properties show that the material prepared is homogeneous with high porosity. The passivation of the nanostructure of PSi for increasing stability, such as post-oxidation of the samples was also proceeded and tested.

The obtained free-standing sample is transparent, brownish. The optical absorption measurement was taken using a Hitach U-2001 spectrophotometer at room temperature. A sharp cut-off absorption edge is located at 410 nm. The absorption wing extends to 600 nm.

## 3. Crystallite size variation

In emission measurement, a broad-band red luminescence can generally be observed by illumination of the sample at wavelength shorter than 600 nm. Fig. 1 stands for typical luminescence spectrum of PSi at room and low temperature at 8 K using Ar<sup>+</sup> laser as a light source. At room temperature, the position of emission band maximum is insensitive to the excitation wavelength whereas at low temperature of 8 K the peak shifts toward low energy in parallel to the excitation photon energy. Comparing the spectra obtained at different temperatures, no distinct correlation between peak position and temperature, or between emission bandwidth and temperature was observed. It suggests that all excitations are highly localized. For excitation at 458 nm, the electrons in conduction band with energy well above the band gap could undergo a direct radiative transition in the area where they were excited while the others could migrate away. The excitation migration would then

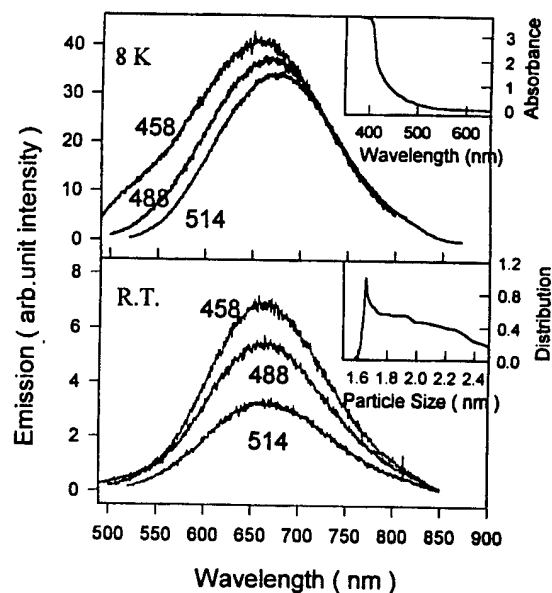


Fig. 1. Emission spectra of PSi by excitation of an Ar<sup>+</sup> laser at three different wave lengths. The upper graph stands for low temperature at 8 K, while the lower one for room temperature. The upper inset is the absorption spectrum, the lower inset represents the size distribution of particles.

Due to the quantum confinement of the free carriers in the nanocrystallites it is expected that each particle is transparent for energies ( $E$ ) less than its optical gap ( $E_g$ ) and its absorbance increases abruptly for  $E > E_g$ . The transmission coefficient of the PSi film can be expressed as

where  $C$  is a constant and  $A(r, \lambda)$  is proportional to the energy absorbed by a particle of radius  $r$ .  $A(r, \lambda)$  is approximated by the Heavy-side step function,  $A(r, \lambda) \propto \Theta(\lambda_{g,r} - \lambda)$  where  $\lambda_{g,r} = 2\pi\hbar c/E_{g,r}$ , and  $E_{g,r}$  is the energy gap for particles of size  $r$ . From the above expression, we obtain that the first derivative of the transmission spectrum is proportional to the size distribution density,

where  $r_0$  is the size which gives an energy gap corresponding to  $\lambda_0$ . To obtain this size distribution we used the relation between the magnitude of the energy gap and the size of the (spherical) particle suggested in Ref. [7],  $E_{g,r} = 1.1 + 3.65 r^{-1.3}$  where  $E_{g,r}$  is in eV and  $r$  in nm. As shown in Fig. 1 (lower inset) this calculation shows a nonsymmetric size distribution peaking at  $\sim 1.65$  nm in our PSi film.

The nonlinear optical response measurement in PSi is difficult in visible to UV region because of higher absorption that the free-standing sample is used to be burned out before getting signal. In this experiment we use a frequency-tripled  $\text{Y}_3\text{Al}_5\text{O}_{12}:\text{Nd}$  laser operated at 355 nm with pulse width of 45 ps as a pump source for ps optical parametric generation (OPG). The OPG output wavelength can be continuously tuned from 400 to 700 nm. It was found that significant absorption by PSi free standing film in the region of 550–590 nm would cause a damage of sample. In the region of 590–600 nm the obtained response signal is dominant by the slow-response component which originates from the excited state population grating formed by the two pump-pulses across inside the sample. Tuning the wavelength beyond 610 nm caused the DFWM signal too weak to record in transverse geometry. The final measurement was therefore, conducted at 604 nm. In the experiment the laser beam was split into two pump beams and a probe beam as shown in Fig. 2. The latter carried





10% of the total laser power. The probe went through an optical delay line, and was then incident on the sample from the substrate side. The two pump beams were crossed on the film at an angle, interfering to form a transient grating in the film. The delay line in one of the pump beam paths was used to ensure simultaneity of the pulses at the sample. The beam size of the probe was about 50% that of the pump. Thus, the probe could uniformly sense the susceptibility within the interference region of the two pump pulses. DFWM methods for thin films have been amply discussed in the literature [8,9]. All the beams in our experiment were in backward phase conjugation configuration, which can allow higher signal-to-noise ratio. The pump-pulse intensity was typically  $10\text{--}20\text{ mJ/cm}^2$ . The polarization for all measurements was perpendicular to the incidence plane for all four beams, expressed as  $\langle ssss \rangle$ . In this configuration, the time-resolved NLO spectrum can adequately be used to characterize the amorphous PSi's NLO properties.

Fig. 3 shows the DFWM signal of free standing PSi wafer compared with  $\text{CS}_2$  reference. For  $\text{CS}_2$  reference, the intense coherent response signal with a half-width of about 55 ps located at zero delay of the probe pulse is associated with the third-order nonlinearity of the  $\text{CS}_2$  material. It is an instantaneous response. It comes from the change in polarizability of grating peak versus grating valley when two pump pulses are cross inside the sample writing a periodic bright-dark interference pattern. For  $\text{CS}_2$  reference, the fast response is well known as due to the vibrational character of the intermolecular motion in liquid. The signal width is consistent with the intensity autocorrelation of the three laser pulses. For PSi sample, however, the signal consists of two components. One is similar to  $\text{CS}_2$ , with the peak located at zero delay of the probe pulse. The other is a slow response signal, can be identified as to start at  $\sim +30$  ps of the probe pulse delay. The signal intensity of the slow response (SR) is almost a half of the instantaneous response signal, but it lives for much longer. By estimation it can enter into microseconds region.

The first component at zero delay is a direct measure of  $\chi^{(3)}$  of the PSi material. It has two distinct features. Firstly, the ratio of peak intensity

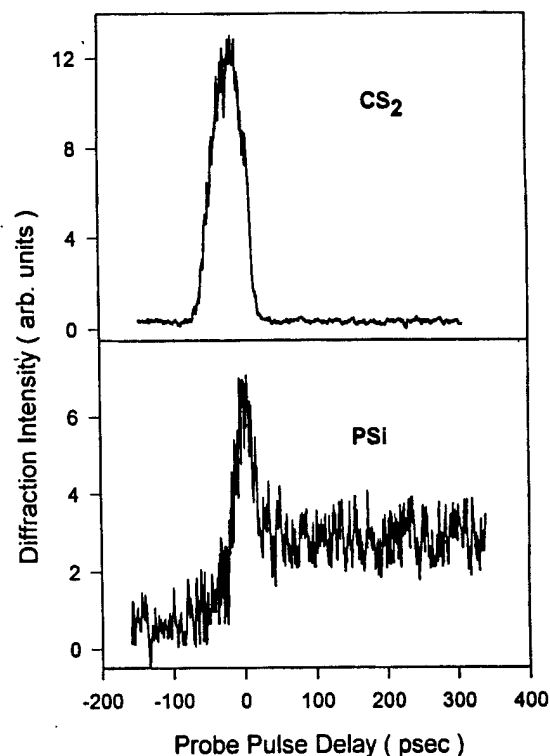


Fig. 3. Picosecond nonlinear optical response of PSi compared with  $\text{CS}_2$  reference.

to sample thickness is extremely large compared to most bulk crystals. In solid-state materials the contribution to the instantaneous signal component may come from electronic cloud deformation as well as the nucleus reorientation. The latter contribution in solids is usually smaller. The second feature of the coherent response component is the squeezed nature in time domain.

When the two pump pulses are polarized in the same direction, the coherent signal component is directly related to the third-order susceptibility by  $\eta = \exp(-\alpha d / \cos \theta) \sin^2(d\pi\Delta n / \lambda \cos \theta)$ , where  $\Delta n = 12\pi\chi^{(3)}/n_0\langle E^2 \rangle$ .  $E$  is optical electric field,  $d$  is the grating thickness, and  $2\theta$  is the crossing angle of the two pump pulses. The intrinsic nonlinear optical response signal generated in this circumstance can be analyzed as the probe beam diffracted by the grating formed by the two pump pulses A and B, which intersect at an angle of  $2\theta$  inside the thin film. The grating vector is  $q = \pm(k_A - k_B)$ , confined in

the film along the  $x$  direction. The electric field amplitude  $A$  is  $A = A_A e^{+ikx} + A_B e^{-ikx}$ , where  $k$  represents the wave vector. The light intensity is then modulated as  $I = I_A + I_B + 2\Delta I \cos(2kx)$ , here  $\Delta I = 1/2n\epsilon_0 A_A \cdot A_B$ . In our experiment,  $I_A = I_B$ , so  $I = 2I_A(1 + \cos(qx))$  for identical polarizations ( $ss$ ) of  $A_A$  and  $A_B$ . The diffracted signal intensity is directly related to the third-order susceptibility as expressed by Eq. (1). Compare the FWHM of Psi sample to  $CS_2$ , the former is about 70% of the latter compared to the electronic part. For isotropic sample  $\chi_{xxxx}^{(3)} = 3\chi_{xxyy}^{(3)} = 3\chi_{yyxx}^{(3)}$  [14]. We obtained  $\chi_{xxxx}^{(3)} = \chi_{xxyy}^{(3)} = \chi_{yyxx}^{(3)} = 0.12 \times 10^{-11} \text{ cm}^3 \text{ erg}$ , which is significantly large compared to many bulk crystals.

The “squeezing” feature observed in the Psi wafer is quite interesting. We previously reported a compression effect of the DFWM signal in bulk  $KNbO_3$  crystal. It was due to TPA interaction [10] between the pump and probe pulses when the laser fluence was greater than  $280 \text{ mJ/cm}^2$ . The narrowed signal was shifted towards negative delay. In the present case, however, the laser fluence was lower and the peak does not shift. Further increasing the laser power would, unfortunately, cause the sample to be damaged. For other thin amorphous samples such as amorphous quartz wafer, no squeezing effect could be observed. The reason for this is not completely understood yet. In four-wave-mixing, squeezed light was first observed by Slusher et al. [11] in an optical cavity (atomic vapor). It was due to the generation of “squeezed states”. In this phenomenon the statistical variance in one of the two in-quadrature components of the coherent electric field is reduced below the shot noise value, while variance of the other component is increased so that the uncertainty principle is satisfied. The squeezing, which could have applications in communications, has also been observed in semiconductors, optical fibers, as well as in waveguides. It is due in these cases to a nonlinear mechanism through the third-order nonlinear susceptibility, including Kerr effect, which can affect the transverse spatial profile of the generated light [12,13]. In our case it possibly relates to a similar mechanism, except for the small optical interaction length in the film.

The second component in Fig. 3 is a SR signal. This signal component is attributed to the population grating produced by the interference of the two crossed laser pulses. In the bright region of the grating, the intrinsic interband transition occurs, forming highly localized surface state as discussed in the above section. It in turn alters the polarizability. In many crystal samples, the SR signal, following the coherent component, used to be built up for a risetime of up to 10 ps [10], which corresponds to relaxation process of the excited state dynamics. In Psi sample, however, no risetime was observed, which further proves that the excitation at 604 nm was highly localized without further migration or other dynamical processes.

#### Acknowledgements

This work was supported by US ARO-DAA, NASA NCCW-0088, US. DoE and NSF-EPSCoR.

#### References

- [1] R. Newman, Phys. Rev. 100 (1955) 700.
- [2] L.T. Canham, Appl. Phys. Lett. 57 (1990) 1046.
- [3] Amato, Science 252 (1991) 922.
- [4] J. Yu, H. Liu, Y. Wang, W. Jia, L.F. Fonseca, S.Z. Weisz, O. Resto, J. Lumin. 81 (1999) 1.
- [5] Z.C. Feng, R. Tsu, Porous Silicon, World Scientific, Singapore, 1994.
- [6] L.F. Fonseca, O. Resto, R. Katiyar, S. Gupta, S.Z. Weisz, Y. Goldstein, A. Many, J. Shappir, in: D. Gershoni (Ed.), Proceedings of the 24th International Conference on the Physics of Semiconductors, CD version, World Scientific, Singapore, 1999.
- [7] C. Delerue, M. Lannoo, G. Allan, J. Lumin. 57 (1993) 249.
- [8] J.M. Nunzi, F. Charra, Appl. Phys. Lett. 59 (1991) 13.
- [9] C. Malouin, A. Villeneuve, G. Vitrant, P. Cottin, R.A. Lessard, J. Opt. Soc. Am. B 15 (1998) 826.
- [10] H. Liu, R.J. Reeves, R.C. Powell, L.A. Boatner, Phys. Rev. 49 (1994) 6323.
- [11] R.E. Slusher, L.W. Hillberg, B. Yurke, J.C. Mertz, J.F. Valley, Phys. Rev. Lett. 55 (1985) 2409.
- [12] M.E. Anderson, D.F. McAlister, M.G. Raymer, J. Opt. Soc. Am. B 14 (1997) 3180.
- [13] A.M. Fox, J.J. Baumberg, M. Dabbicco, B. Huttner, J.F. Ryan, Phys. Rev. 74 (1995) 1728.
- [14] J.P. Bourdin, P.X. Nguyen, G. Rivoire, J.M. Nunzi, Non-linear Opt. 7 (1994) 1.

# Optical property and picosecond response of porous silicon wafer

H. Liu, L.F. Fonseca\*, S.Z. Weisz\*, Q. Yan, W. Jia and O. Resto\*

*Department of Physics, University of Puerto Rico, Mayaguez, PR 00681, USA*

*\*Department of Physics, University of Puerto Rico, Rio Piedras, PR 00931, USA*

**Abstract.** Optical quality, free standing and highly photoluminescent PSi was prepared from both, p- and n-type Si wafers using electrochemical anodization of c-Si. The porosity and the final structural and optical properties of the samples were found to be altered drastically by changing the acid concentration, current density, anodization time as well as the characteristics of the Si-wafer. In optical measurement, a broad and intense absorption band is in the UV-Visible region with a cut-off edge at  $\sim 400$  nm. A strong red emission was found to be at  $\sim 670$  nm. It is extremely broad even at 8 K. The experimental results show that a group of sites can be simultaneously excited by pump laser due to excitation energy coincidence. In nonlinear optical measurement the optical response was characterized using degenerate four-wave-mixing (DFWM) in a backward configuration. The response signal consists of an instantaneous component followed by a long lived, slowly decaying component. They are associated with the third-order susceptibility of PSi and the surface states. The response due to the surface state is significant.

## INTRODUCTION

It is well known that the small and indirect band gap of crystalline silicon (c-Si) is characterized by an extremely low quantum efficiency of luminescence while porous silicon (PSi), obtained by electrochemical etching of c-Si surfaces, yields extremely high photoluminescence (PL) efficiencies up to  $10^{-1}$  in the visible range (2). The origin of the PL has been the subject of many studies. We have studied the photodynamical process and Raman spectra of PSi (3,4). It was found that S-band luminescence comes from highly confined regions with a distribution of wire widths. Quantum confinement increases the emission energy and the oscillator strength of the radiative transition, decreasing the radiative lifetime. Therefore the most accepted luminescence mechanism at this time is associated with quantum confinement in the nc-Si formed in the PSi by the anodization process. The presence of  $\sim 3$  nm size nanocrystallites is the size required by the confinement mechanisms to enlarge the band gap. On the other hand, there is interest in the changes of the size-sensitive optical properties due to the quantum confinement. The microstructure of the vitreous state exhibits short-range order within a c-Si core but long-range disorder. The wave vector and eigenfunction associated with an optical process are thus no longer valid due to the lack of periodicity of the structure. In PSi the network can be tailored within one size-category by using size-sensitive, fast selective excitation. This will reveal the associated optical properties of the material, such as photorefractive sensitivity, FWM signal polarization, appearance of ultrafast NLO responses, optical activity, etc.

In nonlinear optical experiments a key parameter to be measured is the nonlinear refractive index which is related to a variety of other NLO effects through the formalism of NLO susceptibilities. It is through these related effects (polarization rotation, optical Kerr effect, self-phase modulation, optical mixing, etc.) that much of the available data on nonlinear refraction as well as the fast third-order nonlinear properties of the material can be obtained. The ultrafast response time on the picosecond time scale is in fact a key point for practical NLO applications such as switching and modulation. However no study on the NLO response from P<sub>Si</sub> has been reported to our knowledge. In this paper we present the experimental results on degenerate-four-wave-mixing (DFWM) measurement as well as the conventional optical spectral.

## EXPERIMENTAL

The optical quality, free standing and highly photoluminescent P<sub>Si</sub> was obtained from both, p- and n-type Si wafers using electrochemical anodization of c-Si. The acid solution for the anodic etching was 1:2:1 (HF:ethanol:water). The electrolytic cell included a standard Platinum electrode as a cathode and the crystalline silicon wafer as an anode. The aluminum ohmic contact at the bottom of the wafers were made by sputtering deposition and annealing. Prior to the anodization, the silicon surface of the wafers were cleaned with 20% HF-aqueous solution for 5 minutes. Samples were anodized and finally dried using the critical point method. Free standing samples were also prepared by applying a high electropolishing pulse at the end of the anodizing process. Such a pulse disengages the porous layer from the underlying crystalline silicon. The key role of the holes in the etching process requires the illumination of the n-type samples during the anodization. The porosity and the final structural and optical properties of the samples can be varied by changing the acid concentration, current density, anodization time as well as the characteristics of the Si-wafer (resistivity and crystalline orientation). The preliminary studies we have made including the determination of electronic surface states densities, electrical transport properties, and optical and morphological properties and surface properties show that the material prepared is homogeneous with high porosity. The passivation of the nanostructure of P<sub>Si</sub> for increasing stability, such as post-oxidation of the samples was also proceeded and tested. Optically, nanoporous-Si behaves as a homogenous material in the visible and longer wavelength regions, as tested by ellipsometry, reflectivity measurements and by transmittance as well. The sample studied here was prepared from a boron doped Si wafer with (100) crystalline orientation and 0.5-1.5  $\Omega\text{cm}$  resistivity. The anodization current (200mA/cm<sup>2</sup>) was applied in 280 steps of 0.8sec each and with resting intervals of 1.4 sec between anodizations, such that a high-optical quality, free-standing porous film was obtained.

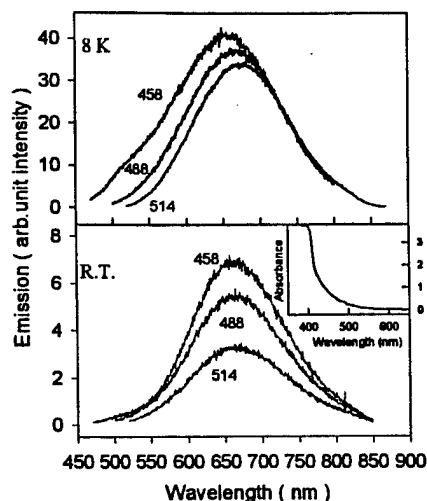


**FIGURE 1.** Emission spectra of PSi by excitation of an  $\text{Ar}^+$  laser at 3 different wavelengths. The upper graph stands for low temperature at 8 K, while the lower one for room temperature. The inset represents the absorption spectrum.

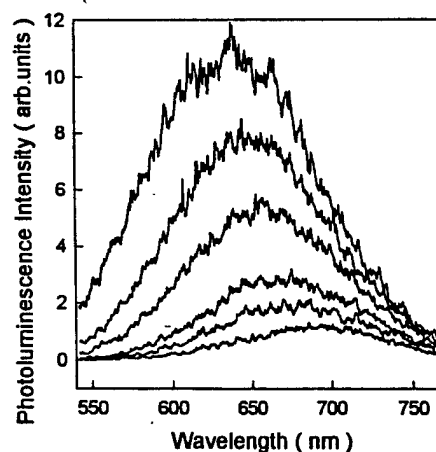


**FIGURE 2.** Time-resolved emissionspectra of PSi excited at 532 nm. The delay time from upper to lower: 4, 24, 44, 64, 84  $\mu\text{s}$ .

### Absorption and emission

The absorption measurement was conducted using a Hitach spectrophotometer at room temperature. A sharp cut-off absorption edge at the high energy side is located at  $\sim 410\text{nm}$  and the low energy side is at  $\sim 510\text{ nm}$  (shown in the inset of Figure 1) with a tail extended to 600 nm. At the wavelength greater than 510 nm the absorption becomes very weak, and at 633 nm the absorption is negligible.

The emission measurements were conducted using lasers setting at different wavelengths covering 458 - 633 nm region in purpose to provide different excitation photon energy. Nevertheless, in all cases a broad band red luminescence can generally be observed. Fig. 1 stands for a typical luminescence spectra of PSi at room and low temperature 8 K. Three lines from an  $\text{Ar}^+$  laser at 458, 488 and 514 nm were used for excitation. At room temperature, the emission band maximum does not shift markedly with changing excitation wavelength, but emission intensity varies significantly because absorption changes from 458 nm to 514 nm. At low temperature 8 K however, the emission peak obviously shifts toward longer wavelengths while the excitation tuned to longer wavelength. But the emission intensity does not change so much as what observed at room temperature. It is presumably due to a flat plateau in this absorption region at low temperature. On the other hand, to compare the spectra obtained at different temperature no distinct correlation between peak position and temperature, or between emission bandwidth and temperature was observed. Furthermore, emission spectra excited at 633 nm. were also obtained, and used to compare with those excited at shorter wavelengths. The photon energy of 633 nm excitation is

lower than the absorption edge 510 nm. However, the luminescence can still be observed. In all cases the common feature for all emission spectra is the large bandwidth. From excitation at 458 nm to 633 nm, the difference of bandwidth was found to be less than 10%. Therefore, it is suggested that all excitations are highly localized. Fig.2 shows the time-resolved emission spectra at room temperature. The excitation was at 532 nm with the delay time from 4 to 84  $\mu$ s. It features a typically glassy-like profile. As the delay time increases shorter-lived emitter dies out leaving luminescence due to longer-lived emitter dominant. As shown in the figure there is no interaction evidence in any emission profile. The contribution of phonon-assisted transition is less important here, compared to the case of 3d or 4f ions-doped materials. The reason is two-fold, as discussed in the following. From general understanding we may assume two possible recombination processes. For those electrons excited from valence band to conduction band by excitation at 458 nm, they possess excitation energy well above the bandgap. A part of them could undergo a direct radiative transition in the area where they were excited while the others could migrate away. The excitation migration would then be trapped in some different confined region, and emit from that region. If this latter case were true the entire emission would be an overlap of entire emission from different regions, resulting in a much broader and diffusive feature with an obvious wavelength dependence. On the other hand, for those electrons excited by 633nm excitation they possess energy well below the bandgap. These electrons can not undergo a migration process. They must immediately be localized and/or emit light from the excited region. In this case the emission profile is supposed to be not as broader as that in the former case. Therefore, because all emissions excited at different wavelengths exhibit similar breadth it implies that the confined regions giving light emission are mainly isolated and scattered in porous Si samples. This is in consistence with conclusions of other studies. For instance, the studies on the polarization of the luminescence of porous Si have supported the model that only limited migration of carriers to neighboring regions may occur (5-7). The second-fold consideration is that in nanocrystals, the phonon spectra are modified due to the break-down of the lattice periodicity. Anharmonic effects of lattice vibration may also become important. A large number of activators are expected to be located in a distorted lattice environment near the surface. The radiative recombination in the localized state on the nanocrystallite surface causes the strong visible photoluminescence. This kind of PL is sensitive to the nanocrystallite size, and insensitive to the temperature.

### Transient optical response from PSi

Study on nonlinear optical property of porous Si, particularly the transient optical response measurement has not yet reported to our knowledge. It is due mainly to the technical difficulty in performing such kind of measurements. With a green light source (available for most commercial pulsed lasers) the absorption by PSi film is too strong for the material to sustain. We are able to perform this kind of measurement by turning the picosecond light source into the yellow - orange region. using technique of picosecond optical parametric generation. A frequency-tripled  $\text{Y}_3\text{Al}_5\text{O}_{12}:\text{Nd}$  laser operated at 355 nm

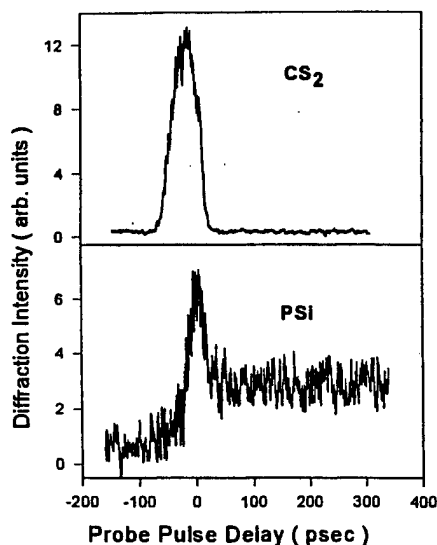


**FIGURE 3.** Picosecond nonlinear optical response of PSi compared with CS<sub>2</sub> reference.

with pulse width of 45 ps was used for optical parametric generation. The output wavelength can be continuously tuned from 400 to 700 nm. In order to determine which wavelength can be best used for characterization, the measurement was checked by turning laser was within 550 - 650 nm. Significant absorption by Psi free standing film in the region of 550 - 590 nm would cause a damage of sample. In the region of 590 - 600 nm the obtained response signal is dominant by the slow-response component which originates from the excited state population grating formed by the two pump-pulses across inside the sample. Tuning the wavelength beyond 610 nm caused the DFWM signal too weak to record in transverse geometry. The final measurement was therefore conducted at 604 nm. In the experiment the laser beam was split into two pump beams and a probe beam. The latter carried 10% of the total laser power. The probe went through an optical delay line, and was then incident on the sample from the substrate side. The two pump beams were crossed on the film at an angle, interfering to form a transient grating in the film. The delay line in one of the pump beam paths was used to ensure simultaneity of the pulses at the sample. The beam size of the probe was about 50% that of the pump. Thus, the probe could uniformly sense the susceptibility within the interference region of the two pump pulses. DFWM methods for thin films have been amply discussed in the literature (8,9). All the beams in our experiment were in backward phase conjugation configuration, which can allow higher signal-to-noise ratio. The pump-pulse intensity was typically 10 - 20 mJ/cm<sup>2</sup>. The polarization for all measurements was perpendicular to the incidence plane for all 4 beams, expressed as <ssss>. In this configuration, the time-resolved NLO spectrum can adequately be used to characterize the amorphous PSi's NLO properties.

Fig. 3 shows the DFWM signal of free standing PSi wafer compared with CS<sub>2</sub> reference. For CS<sub>2</sub> reference, the intense coherent response signal with a half width of about 55 psec located at zero delay of the probe pulse is associated with the third-order nonlinearity of the CS<sub>2</sub> material. It is an instantaneous response. It comes from the change in polarizability of grating peak versus grating valley when 2 pump pulses are cross inside the sample writing a periodic bright-dark interference pattern. For CS<sub>2</sub> reference, the fast response is well know as due to the vibrational character of the intermolecular motion in liquid. The signal width is consistent with the intensity autocorrelation of the three laser pulses. For PSi sample, however, the signal consists of 2 components. The one is similar to CS<sub>2</sub>, with the peak located at zero delay of the probe pulse. The other one is a slow response signal,

can be identified as to start at  $\sim +30$  ps of the probe pulse delay. The signal intensity of the slow response (SR) is almost a half of the instantaneous response signal, but it lives for much longer. By estimation it can enter into microseconds region.

The first component at zero delay is a direct measure of  $\chi^{(3)}$  of the PSi material. It has two distinct features. Firstly, the ratio of peak intensity to sample thickness is extremely large compared to most bulk crystals. In solid state materials the contribution to the instantaneous signal component may come from electronic cloud deformation as well as the nucleus reorientation. The latter contribution in solids is usually smaller. The second feature of the coherent response component is the squeezed nature in time domain.

When the two pump pulses are polarized in the same direction, the coherent signal component is directly related to the third-order susceptibility by

$$\eta = \exp(-\alpha d / \cos \theta) \sin^2(d\pi \Delta n / \lambda \cos \theta), \quad (1)$$

where

$$\Delta n = \frac{12\pi}{n_0 \langle E^2 \rangle} \chi^{(3)}, \quad (2)$$

here,  $E$  is optical electric field,  $d$  is the grating thickness, and  $2\theta$  is the crossing angle of the two pump pulses. The intrinsic nonlinear optical response signal generated in this circumstance can be analyzed as the probe beam diffracted by the grating formed by the two pump pulses A and B, which intersect at an angle of  $2\theta$  inside the thin film. The grating vector is  $q = \pm (k_A - k_B)$ , confined in the film along the x direction. The electric field amplitude  $A$  is

$$A = A_A e^{+ikx} + A_B e^{-ikx}, \quad (3)$$

where  $k$  represents the wavevector. The light intensity is then modulated as

$$I = I_A + I_B + 2\Delta I \cos(2kx), \quad (4)$$

here  $\Delta I = 1/2 n \epsilon_0 A_A A_B$ . In our experiment,  $I_A = I_B$ , so  $I = 2I_A(1 + \cos(qx))$  for identical polarizations (ss) of  $A_A$  and  $A_B$ . The diffracted signal intensity is directly related to the third-order susceptibility as expressed by Eq.(1). Compare the FWHM of PSi sample to  $\text{CS}_2$ , the former is about 70% of the latter compared to the electronic part. For isotropic sample  $\chi^{(3)}_{xxxx} = 3 \chi^{(3)}_{xxyy} = 3 \chi^{(3)}_{yyxx} (10)$ . We obtained  $\chi^{(3)}_{xxxx} = \chi^{(3)}_{xxyy} = \chi^{(3)}_{yyxx} = 0.12 \times 10^{-11} \text{ cm}^3 \text{ erg}$ , which is significantly large compared to many bulk crystals.

The "squeezing" feature observed in the PSi wafer is quite interesting. We previously reported a compression effect of the DFWM signal in bulk  $\text{KNbO}_3$  crystal. It was due to TPA interaction (11) between the pump and probe pulses when the laser fluence was greater than  $280 \text{ mJ/cm}^2$ . The narrowed signal was shifted towards negative delay. In the present case, however, the laser fluence was lower and the peak does not shift. Further increasing the laser power would, unfortunately, cause the sample to be damaged. For other thin amorphous samples such as amorphous quartz wafer, no squeezing effect could be observed. The reason for this is not completely understood yet. In four-wave-mixing,



squeezed light was first observed by R.E. Slusher et al. (12) in an optical cavity (atomic vapor). It was due to the generation of "squeezed states". In this phenomenon the statistical variance in one of the two in-quadrature components of the coherent electric field is reduced below the shot noise value, while variance of the other component is increased so that the uncertainty principle is satisfied. The squeezing, which could have applications in communications, has also been observed in semiconductors, optical fibers, as well as in waveguides. It is due in these cases to a nonlinear mechanism through the third-order nonlinear susceptibility, including Kerr effect, which can affect the transverse spatial profile of the generated light (13, 14). In our case it possibly relates to a similar mechanism, except for the small optical interaction length in the film.

The second component in Fig. 3 is a SR signal. This signal component is attributed to the population grating produced by the interference of the two crossed laser pulses. In the bright region of the grating, the intrinsic interband transition occurs, forming highly localized surface state as discussed in the above section. It in turn alters the polarizability. In many crystal samples, the SR signal, following the coherent component, used to be built up for a risetime of up to tens picoseconds (14), which corresponds to relaxation process of the excited state dynamics. In PSi sample, however, no risetime was observed, which further proves that the excitation at 604 nm was highly localized without further migration or other dynamical processes.

## ACKNOWLEDGMENTS

This work was supported by US ARO-DAA, NASA NCCW-0088, US. DoE and NSF-EPSCoR.

## REFERENCES

1. L.T. Canham, Appl. Phys. Lett. 57, 1046 (1990).
2. Z.C. Feng and R. Tsu, Porous Silicon (World Scientific, Singapore, 1994).
3. J.Yu, H.Liu, Y.Wang, W.Jia, L.F. Fonseca, S.Z. Weisz and O Resto, "A new analysis method to characterize the S-band luminescence decay of porous Si", J.Lumin., 81 (1999) 1.
4. L.F. Fonseca, O. Resto, R. Katiyar, S. Gupta, S.Z. Weisz, Y. Goldstein, A. Many and J. Shappir, Proc. 24th Int. Conf. Semiconductor Physics, ICPS 24, Jerusalem, August 1998 (World Scientific, Singapore), to be published.
5. Hideki Koyama, Ysuyoshi Ozaki, and Nobuyoshi Koshida, Phys. Rev. 52, 11561 (1995).
6. A. G. Cullis, L. T. Canham and P. D. J. Calcott, J. Appl. Phys., 82, 909 (1997).
7. H. Koyama and N. Koshida, Phys. Rev. B 52, 2649 (1995).
8. J.M. Nunzi and F. Charra, Appl. Phys. Lett., 59, pp. 13-15 (1991).
9. C. Malouin, A. Villeneuve, G. Vitran, P. Cottin and R.A. Lessard, J. Opt. Soc. Am. B, 15, pp. 826-837 (1998).
10. J.P. Bourdin, P.X. Nguyen, G. Rivoire and J.M. Nunzi, Nonlinear Opt., 7, 1 (1994).
11. H. Liu, R.J. Reeves, R.C. Powell and L. A. Boatner, Phys. Rev., 49 (1994) 6323.
12. R.E. Slusher, L.W. Hillberg and B. Yurke, J.C. Mertz and J.F. Valley, Phys. Rev. Lett., 55 (1985) 2409.
13. M.E. Anderson, D.F. McAlister and M.G. Raymer, J. Opt. Soc. Am. B, 14 (1997) 3180.
14. A.M. Fox, J.J. Baumberg, M. Dabbicco, B. Huttner and J.F. Ryan, Phys. Rev., 74 (1995) 1728.

## LINE SHAPE IN RESONANCE RAMAN SCATTERING FROM SILICON QUANTUM DOTS

R.K. SONI, L.F. FONSECA, O. RESTO, S.Z. WEISZ AND S. TRIPATHY \*

Department of Physics, University of Puerto Rico, San Juan, PR-00931, USA

\*Department of Physics, Indian Institute of Technology, New Delhi-110016, INDIA

### ABSTRACT

We have carried out a resonance Raman study of line-shape in silicon quantum dots synthesized on a quartz substrate by co-sputtering bulk Si and SiO<sub>2</sub>. Optical transmission measurements are used to evaluate dot size distribution. The size distribution shows peaks around 1.0 and 1.4 nm. The Si dots exhibit photoluminescence in the visible region, which shifts to higher energy with decreasing size. The size dependence of Raman scattering shows phonon softening and increasing asymmetrical broadening for small dots (< 2nm). The observed spectra are compared with calculations considering electron-hole interactions at a quasi-direct gap of a spherical quantum dot.

### INTRODUCTION

Nanometer size Si crystals show marked improvement in photoluminescence (PL) quantum efficiency compared to bulk silicon and are, therefore, attractive for silicon based optoelectronic applications [1]. The PL observed from Si nanocrystals is attributed to quantum size effects. The effect of carrier confinement and band gap upshift in Si nanocrystals has been discussed intensively in the literature [1]. The photoluminescence energy for Si nanocrystals have been calculated by using the empirical pseudopotentials [2], the third nearest neighbor tight binding [3] and time dependent tight binding techniques [4]. Despite the apparent disagreement in predicting the peak PL energy, these calculations demonstrate that the PL energy increases as the nanocrystal size decreases and the dominant contribution to the visible light emission comes from nanocrystals smaller than 2 nm.

The resonantly excited PL spectrum has shown long radiative lifetimes in Si nanocrystals and provides important evidence that phonons are directly involved in the radiative recombination process [5]. Clearly, this suggests that the Si nanocrystal energy band remains indirect type. Theoretical calculations, however, indicate that a quasi-direct gap in nanocrystal Si is possible for sizes 1.0-1.5 nm in diameter [3].

Raman scattering techniques are commonly used for semiquantitative determination of size effects on vibrational modes, such as confined optical phonon, surface phonon and confined acoustic phonon, in nanocrystal or quantum dots (QD) [6-11]. An adequate knowledge of the bulk phonon dispersion is a prerequisite for understanding lattice dynamical properties and electron-phonon interactions in QD. The first-order resonant Raman scattering via the Frölich interaction has been investigated for spherical QD [9]. The electronic intermediate state was considered as uncorrelated electron-hole pairs. Electron-hole correlation effects via Coulomb interaction on Raman amplitude for spherical QD has also been reported [10,11]. It was shown that the resonant scattering efficiencies depend strongly on the Coulomb correlation and only excitonic states and vibrational modes with zero angular momentum were allowed in the Raman process.

The effect of carrier confinement on optical phonons in Si QD has been widely studied by Raman scattering [6-8]. The size effect is reflected in a finite wave vector of QD and

corresponding lowering of phonon frequency from bulk. A quantum confinement model that takes into account the finite phonon wave vector and gaussian size distribution for spherical quantum dots is generally invoked to explain the observed Raman line shape. In this report, we investigate the Raman line shape from Si dots dispersed in a  $\text{SiO}_2$  matrix grown on a quartz substrate. We emphasize the role of Si dots that favor the resonant interaction with incoming or outgoing photon in the Raman process.

## EXPERIMENTAL

The Si- $\text{SiO}_2$  film was grown on the quartz substrate by rf co-sputtering. The substrate was a 6-inch long quartz plate. On a  $\text{SiO}_2$  target (6 inch in diameter) small pieces of Si tips (area  $\sim 0.1 \text{ in}^2$ ) were placed and they were co-sputtered for 3 hours. The number of Si tips and their position on the  $\text{SiO}_2$  were used to control the size of silicon dots. The film was subsequently annealed in nitrogen ambient at  $1100^\circ\text{C}$  for 30 minutes. The deposited film has an area of  $5 \text{ in} \times 0.2 \text{ in}$  and thickness of the order of  $1.7 \mu\text{m}$ . Dot size and silicon concentration vary monotonically along the length of the film. The estimated Si dot density varies from  $1.5 \times 10^{22}/\text{m}^3$  at  $\text{SiO}_2$ -rich end to  $3.5 \times 10^{23}/\text{m}^3$  at Si-rich end of the film. The transmission measurements were made in the range 190-820 nm using a HP-8452A spectrophotometer. The photoluminescence and Raman measurements were performed in a quasi back-scattering geometry at room temperature using the 514.5 nm line of an  $\text{Ar}^+$  laser. The laser power was kept low (20 mW) and the laser beam was focussed to a spot of  $25 \mu\text{m}$  size on the film. The spectra were dispersed by a TRIAX 320 spectrometer and detected by a cooled photomultiplier with GaAs photocathode.

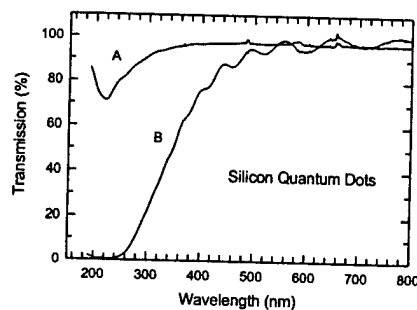


Fig.1(a). Transmission spectra from two regions (A and B) of Si- $\text{SiO}_2$  film.

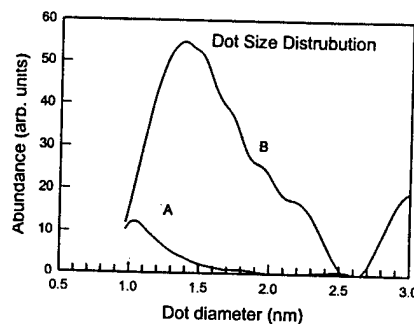


Fig.1(b). Size distribution at the region A and B of the film calculated from transmission spectra.

## RESULTS

Figure 1(a) shows typical transmission spectra taken from two regions of Si- $\text{SiO}_2$  film. In our case the Si dot size is dispersed along the length of the film on the quartz plate. The transmission coefficient of the film is related to the energy absorbed by the Si quantum dot of size  $R$  imbedded in the  $\text{SiO}_2$  matrix. From the optical transmission we calculated the dot size

distribution by assuming that the absorption is primarily due to interband transitions between the quantum confined states of a spherical Si dot. Furthermore, it is assumed that at the enlarged gap of the quantum dot the absorption coefficient changes abruptly from zero to a finite value. By taking the dependence of energy gap on the size of spherical dot as  $1.1 + 3.65 R^{-1.3}$  [12], size distribution can be approximated with the first derivative of the transmission spectrum [13]. The estimated size distribution is asymmetric with long tail towards the larger size and centered around 1.0 nm and 1.4 nm as shown in Figure 1(b). With increasing size, the distribution becomes broader.

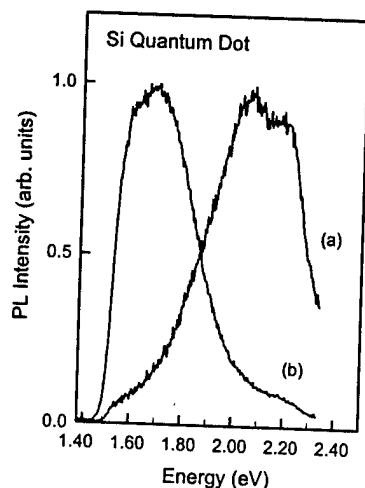


Fig. 2. Normalized PL spectra from (a) 1.4 nm, and (b) 2.2 nm diameter Si dots excited with 514.5 nm laser line.

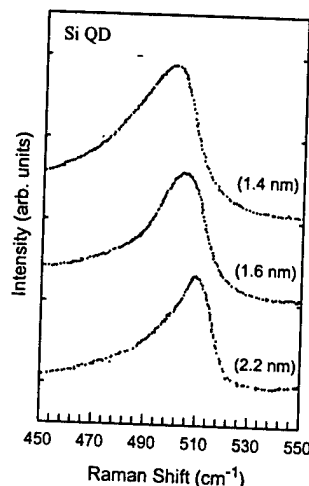


Fig. 3. Size dependence Raman spectra from Si dots excited with 514.5 nm laser line.

Figure 2 shows the PL emission spectra from Si QD excited with the green line (2.412 eV) of an argon ion laser. The PL spectrum is broad and shifts to higher energy with decreasing dot size. The peaks are observed at 1.69 eV and 2.06 eV for dot sizes of 2.2 nm and 1.4 nm, respectively. The average dot sizes were obtained from the transmission data with an error of  $\pm 0.2$  nm. We attribute the featureless broad PL spectrum to band-to-band recombination in Si QD and fluctuation in QD sizes. For the 1.4 nm dot size, we also see structure towards the high energy (2.2 eV) due to resonant excitation with laser line. According to Delerue et al. [14], EPS or tight binding as well as corrected *ab initio* local density approximation (LDA) techniques give reliable predictions for Si nanocrystal band gap. It has been pointed out that the quasi particle gaps and exciton coulomb energies of Si nanocrystals require a large correction to the band gap which are not included in the one electron theory. The optical gap is defined as  $E_g^{\text{band}} = E_g^{\text{QP}} - \Sigma_{\text{LDA}} - \Sigma_{\text{C}}$ , where the quasi

particle gap  $E_g^{QP}$  is the difference in energies resulting from the separate addition of an electron and hole to the system,  $\Sigma_{LDA}$  is the self energy corrections and  $\Sigma_C$  is due to exchange correlation effects. The  $\Sigma_{LDA}$  practically compensates for the screened electron-hole interaction  $E_{coul}$  with full dielectric constant. Though our PL results are in qualitative agreement, they fall below the calculated values of optical band gap of silicon nanocrystals with the excitonic correction [14]. It should be emphasized that PL energy is lower than the absorption edge for a given dot size, and this difference is considerably large for smaller size dots. Self trapped exciton at the interface between Si and  $SiO_2$  or a defect state is considered to be responsible for the observed Stokes shift of PL emission energy [14].

The Raman spectra from Si- $SiO_2$  film were excited with the 514.5 nm (2.41 eV) laser line of an argon ion laser from the region that emits green-red luminescence. Figure 3 shows representative spectra from three different positions of the sample characterized by the average Si dot diameter. The observed spectra show phonon softening and line shape broadening with decreasing dot size. As the average dot size decreases from 2.2 nm to 1.4 nm, the Raman peak shifts from 511  $cm^{-1}$  to 502  $cm^{-1}$ . The Raman lines are asymmetrically broadened with a tail towards the low energy side. In the uncorrected data, the integrated intensity remains unchanged. The broad line shape arises from size distribution in an ensemble of dots, which leads to a large fluctuation in wave vectors, particularly for dot sizes smaller than 2 nm.

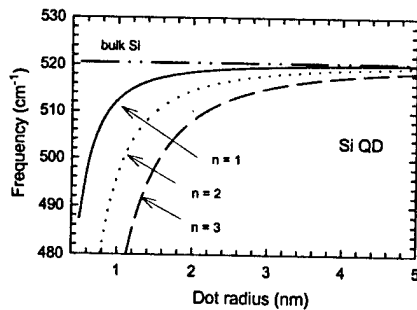


Fig. 4. The radial dependence of  $l = 0$  optical phonon mode for a Si quantum dot embedded in a  $SiO_2$  matrix.

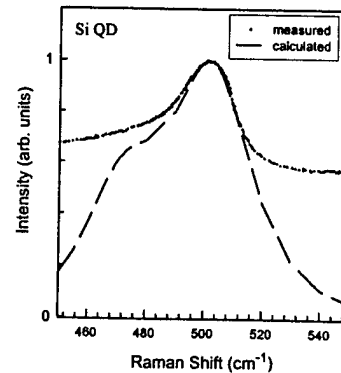


Fig. 5. Calculated resonance contribution to the experimentally observed Raman line shape of a 1.4 nm Si dot.

In order to explain the observed resonance line shape, we assume that the optical vibrations are confined to the spherical dot with effective wave vector  $q_n = \mu_n/R$ , where  $\mu_n$  is  $n^{\text{th}}$  node of the spherical Bessel function  $j_1$ , and  $R$  is the dot radius. A quadratic bulk Si dispersion gives the eigen frequencies  $\omega_n(R)$ . The eigen-frequencies of optical vibrations of zero angular momentum ( $l = 0$ ) mode as a function of  $R$  in a spherical Si dot embedded in  $SiO_2$  are shown in Fig. 4. It should be pointed out that a precise determination of dot size,

particularly for  $R < 1$  nm, is necessary for the estimation of equivalent wave vectors and corresponding eigen-frequencies.

The Raman line shape can be written as  $I(\omega, R)$  [11],

$$I(\omega, R) = I_0 \sum_n \frac{1}{\frac{[(\hbar\omega_i - E_{\mu_1}(R))(\hbar\omega_s - E_{\mu_2}(R)) - \Gamma_{\mu_1}\Gamma_{\mu_2}]^2 + [\Gamma_{\mu_2}(\hbar\omega_i - E_{\mu_1}(R)) + \Gamma_{\mu_1}(\hbar\omega_s - E_{\mu_2}(R))]^2}{\Gamma/\pi}} \frac{1}{[\hbar\omega_i - \hbar\omega_s - \hbar\omega_n(R)]^2 + \Gamma^2} \quad (1)$$

where  $I_0$  is the product of scattering efficiency and eigen-values of the appropriate scattering matrix elements over all the intermediate states,  $R$  is the mean QD radius,  $E_{\mu_1}(R)$  and  $E_{\mu_2}(R)$  are the eigen energy for  $R$  in the  $\mu_1$  and  $\mu_2$  intermediate states, respectively,  $\Gamma_{\mu}$  ( $\Gamma$ ) is the intermediate state (phonon) life time broadening,  $\omega_i$  and  $\omega_s$  are the excited laser energy and scattered photon energy, respectively. In the incoming resonance process,  $\omega_i$  coincides with one of the electronic states  $E_{\mu_1}(R)$  while outgoing resonance occurs when  $\omega_i$  approaches  $E_{\mu_2}$ . The resonance conditions are described as  $\hbar\omega_i = E_{\mu_1}(R)$  for incoming resonance, and  $\hbar\omega_i - \hbar\omega_n(R) = E_{\mu_2}(R)$  for outgoing resonance. We assume that the intermediate electronic state is an electron hole pair state and the electron phonon coupling is via deformation potential interaction. The energy of the QD band edge as a function of dot size is estimated from the two-particle exciton calculation [4]. The resonant dots at the laser photons at 2.412 eV have diameter 1.3-1.4 nm. Figure 5 shows the calculated line shape for 1.4 nm dot. It is evident that the main contribution to the line shape comes from the resonant radii, though non-resonant dots give broad constant background.

The Raman line shape in QD is indeed a convolution of dot size distribution, size selected vibrational modes in resonance with incoming photon or scattered photon. The resonant radii correspond to the resonant dots and give the main contribution to the line shape. Phonons in different quantum confinement dots are also expected to play a significant role in the scattering process, especially when the resonance condition favors smaller radii. The broadening and asymmetry of the Raman spectrum follows from the contribution of several phonon modes of dots with different radii in the resonance region. Appreciable contribution comes from  $|R_c - R| < \delta R$ , where,  $R_c$  = radius for which either incoming or outgoing resonance is reached. In our case  $\delta R = 0.04$  nm. The behavior of  $E_{\mu}(R)$  as a function of  $R$  is taken from the calculations of Ref. 4. A lifetime broadening of 25 meV for all intermediate electronic states involved and phonon half width of  $9 \text{ cm}^{-1}$  was used in the calculation.

## CONCLUSIONS

We have synthesized Si nanocrystals in a  $\text{SiO}_2$  matrix on quartz plate by rf co-sputtering. The Si dots are dispersed in size along the length of the plate. Optical transmission measurements were used to estimate the dot size distribution which shows peaks around  $1.0 \pm 0.2$  nm and  $1.4 \pm 0.2$  nm with an asymmetrical tail towards the large particle size. The PL emission from the dots exhibits broadband in the red and green region, and their peak

energies are smaller compared to the calculated values of the optical gap with the excitonic correction. Size dependence of the Raman scattering was performed on Si dots, the results show phonon softening and large asymmetrical broadening. With decreasing dot size broadening increases further due to fluctuation in effective wave vector associated with size distribution. The observed asymmetry was calculated by considering phonon confinement in a spherical dot. For small dot size, the line shape is dominated by the resonant dots that favor incoming or outgoing resonance.

The electronic state responsible for the resonant interaction with the dot has a large lifetime broadening of the order of 25 meV. The weak resonance enhancement seen under the resonant condition is indicative of band-to-band transitions in the Raman process. The size distribution in our sample does not allow a quantitative determination of relative contribution of vibrational and electronic states to the Raman line shape as has been done for CdSe [11].

We have assumed a quasi-direct gap for Si dots in this calculation, and it should be emphasized that the distinction between resonance near a direct gap or an indirect gap of Si QD can be seen only in a two-phonon scattering process. The two-phonon scattering usually consists of contribution from several zone-edge regions and involves phonons of particular symmetry. The resonance near a direct gap shows enhanced amplitude for phonons of all symmetries whereas near an indirect gap, phonons of particular symmetry show selective resonance enhancement due to iterative electron-one phonon process.

#### ACKNOWLEDGEMENT

Authors acknowledge partial support from US ARO grant No. DAAH04-96 and NASA grant No. NCCW-0088.

#### REFERENCES

1. L. Tsybeskov, MRS Bulletin, April 1998, 33.
2. L.W. Wang and A. Zunger, J. Phys. Chem. **98**, 2158 (1994).
3. C. Delerue, G. Allan, and M. Lannoo, Phys. Rev. B **48**, 11024 (1993).
4. Nicola A. Hill and K. Birgitta Whaley, Phys. Rev. Lett. **75**, 1130 (1995).
5. M. Rosenbauer, S. Finkbeiner, E. Bustarret, J. Weber, and M. Stutzmann, Phys. Rev. B **51**, 10539 (1995).
6. H.D. Fuchs, M. Stutzmann, M.S. Brandt, M. Rousenbauer, J. Weber, A. Breitschwerdt, P. Deak, and M. Cardona, Phys. Rev. B **48**, 8172 (1993).
7. Y. Kanazawa, S. Hayashi, and K. Yamamoto, J. Phys. Condens. Matter **8**, 4823 (1996).
8. M. Fujii, Y. Kanazawa, S. Hayashi and K. Yamamoto, Phys. Rev. B **54**, R8373 (1996).
9. M.P. Chamberline, C. Trallero-Giner, and M. Cardona, Phys. Rev. B **51**, 1680 (1995).
10. E. Menendez, C. Trallero-Giner, and M. Cardona, Phys. Status. Solidi, B **199**, 81 (1997).
11. C. Trallero-Giner, A. Debernardi, M. Cardona, E. Menendez-Proupin and A.I. Ekimov, Phys. Rev. B **57**, 4664 (1998).
12. C. Delerue, M. Lannoo, and G. Allan, J. Luminescence. **57**, 249 (1993).
13. L.F. Fonseca, O. Resto, S. Gupta, R.S. Katiyar, S.Z. Weisz, Y. Goldstein, A. Many, and J. Shappir, in *Proc. of the 24th International Conference on Physics of Semiconductor, Israel 1998 World Scientific*, in press.
14. C. Delerue, G. Allan, M. Lannoo, J. of Lumines. **80**, 65 (1999).

## Relation between electroluminescence and photoluminescence in porous silicon

E. Savir <sup>a,\*</sup>, J. Jedrzejewski <sup>a</sup>, A. Many <sup>a</sup>, Y. Goldstein <sup>a</sup>, S.Z. Weisz <sup>b</sup>, M. Gomez <sup>b</sup>,  
L.F. Fonseca <sup>b</sup>, O. Resto <sup>b</sup>

<sup>a</sup> *Racah Institute of Physics, The Hebrew University, Jerusalem 91904, Israel*

<sup>b</sup> *Department of Physics, University of Puerto Rico, Rio Piedras PR 00931, USA*

### Abstract

We present combined measurements of electroluminescence (EL) and photoluminescence (PL) in p-type porous silicon. The EL spectra were measured using an electrolyte contact for electron injection into the porous face of the sample. Upon applying the current, the EL intensity first rises with time, reaches a maximum, and then decays to zero. (The whole process takes about half an hour.) At the same time, the peak of the EL spectrum shifts from  $\approx 850$  nm in the beginning to  $\approx 600$  nm at the end of the process. The PL, which was measured simultaneously, peaked at  $\approx 750$  nm in the beginning and was much wider than all of the EL spectra. Towards the end of the EL process, the red part of the PL spectrum practically disappears. This shifts the PL peak towards the blue, to about the same wavelength as the EL peak ( $\approx 600$  nm) and the spectrum becomes much narrower, comparable to the EL spectrum. The voltage across the sample during the EL process shows a moderate increase up to the point where the EL disappears, and then the voltage rises steeply. This behavior is associated with the build-up of a thin oxide layer on the porous surface. The combined results of EL and PL, and especially the disappearance of the red part in the photoluminescence spectrum at the end of the EL process, suggest that in addition to quantum confinement, localized surface states play an important role in the luminescence process, at least in the red part of the spectrum. Such states may be associated with adsorbed species and disappear upon oxidation. © 2000 Elsevier Science S.A. All rights reserved.

**Keywords:** Electroluminescence; Photoluminescence; Porous silicon; Localized surface states

### 1. Introduction

Porous silicon [1–4], obtained by electrochemical etching procedures applied to crystalline silicon surfaces, exhibits high luminescence efficiencies in the visible range. It is generally accepted that the visible luminescence originates from the band-gap enlargement due to quantum confinement in the porous silicon nanocrystallites [3,4]. At the same time, the reasons for the high-efficiency luminescence are still somewhat under debate [3–5]. It was suggested that it is the amorphous or microcrystalline nature of the porous silicon that is responsible for the phenomenon, or that the formation of silicon compounds such as siloxene ( $\text{Si}_6\text{O}_3\text{H}_6$ ) or Si–H, Si–O and Si–F bonds are involved in the luminescence [3,4].

In this paper we present combined measurements of electroluminescence (EL) and photoluminescence (PL) in p-type porous silicon. It is shown that our combined results of EL and PL point to the important conclusion that in addition to quantum confinement, localized surface states play an important role in the luminescence process at the red part of the spectrum. Such states may be associated with adsorbed species and disappear upon oxidation.

### 2. Experimental

The starting material was high-grade p-type (100) silicon of resistivity in the range 0.5–1.5  $\Omega\text{cm}$ . A p+ layer was formed by diffusing metallic Al into the back faces of the silicon wafers to obtain an ohmic contact. The sample was attached to a cylindrical Teflon cell via a Kalrez O-ring. The sample constituted the bottom of

\* Corresponding author.



the cell, with its front surface facing upwards. Before anodization, the samples were etched in 20% HF. In order to prepare the porous surface [4], a solution of HF, ethanol and water (1:2:1) was poured into the cell. A platinum electrode was immersed in the solution and a spring contact was attached to the bottom p+ contact. The anodization of the Si surface was carried out with a current density of  $15\text{--}50\text{ mA cm}^{-2}$ .

The EL and PL were measured in the same cell using a CCD-based computer board spectrometer. In the former case the cell was filled with an electrolyte consisting of an aqueous solution of NaCl. The EL was obtained under constant current conditions, the current densities ranging from  $1\text{--}3\text{ mA cm}^{-2}$ . The PL was excited by a 45-mW argon laser beam of 488 nm wavelength.

### 3. Results

In order to determine the EL characteristics we applied to the cell a constant current (the electrolyte negative) and continuously measured the EL spectra. In Fig. 1 we show some of these spectra (assorted symbols) obtained at different times of the EL current flow as marked on the curves. We see that upon applying the current the EL intensity first rises with time, reaches a maximum, and then decays to zero. The whole process usually takes about half an hour. At the same time, the peak of the EL spectrum shifts from  $\approx 850\text{ nm}$  in the beginning to  $\approx 600\text{ nm}$  towards the end of the process.

The solid curve represents the total luminescence power as a function of wavelength, obtained by integrating the EL emission intensity. It is seen that this curve forms an envelope of the EL spectra at the different stages of the current flow, as expected.

The width of the different EL spectra was found to be about 120 nm and is essentially the same for all samples studied. This is illustrated also by the data in Fig. 2. Here we plot the EL peak amplitude as a function of the area of the spectrum. The various symbols (nine altogether) correspond to samples prepared under different anodization conditions, while the recurrence of the same symbol represents measurements at different times of the EL current flow. We note that all data lie on a straight line, showing the proportionality between the emitted EL power (area) at any time and the peak amplitude. This indicates that both the shape and the width of the various spectra are constant. Accordingly we used the peak amplitude to represent the emitted EL power.

The main conclusions from Fig. 1 are summarized in Fig. 3. Here we plot the emitted EL power and the wavelength of the spectral peak as functions of time. Also plotted is the time variation of the voltage across the sample. Note that during the time that the EL persists, the voltage rises moderately, but shortly after the disappearance of the EL, it rises steeply. This behavior is associated with the buildup during the EL current flow of an insulating layer, most probably an oxide, on the porous surface. In fact we have measured the buildup process of such an oxide layer on crys-

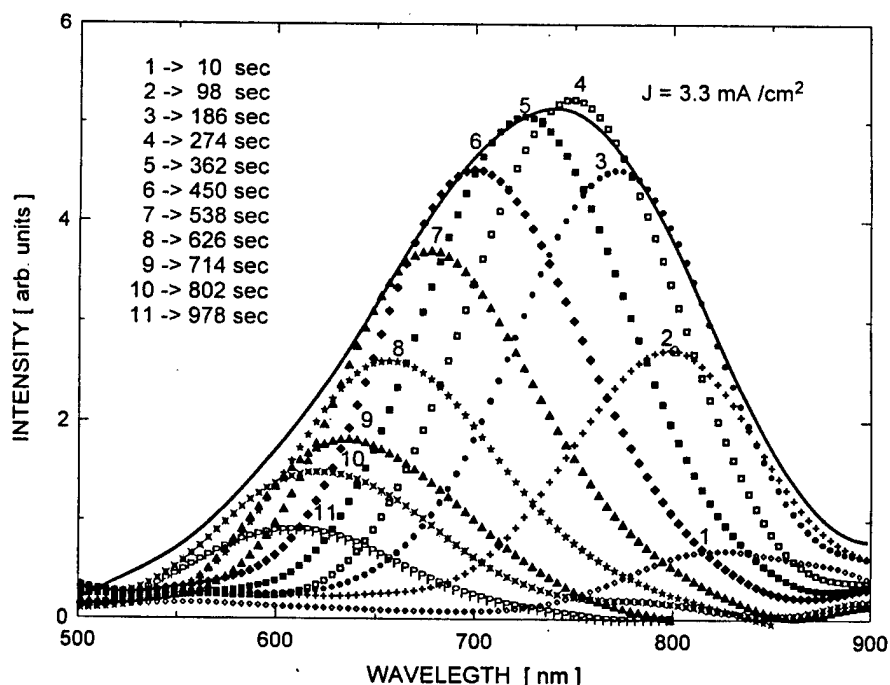


Fig. 1. Several EL spectra (assorted symbols) obtained at different times of the EL current flow (current density  $J = 3.3\text{ mA cm}^{-2}$ ) as marked on the curves. The solid curve represents the total luminescence power.

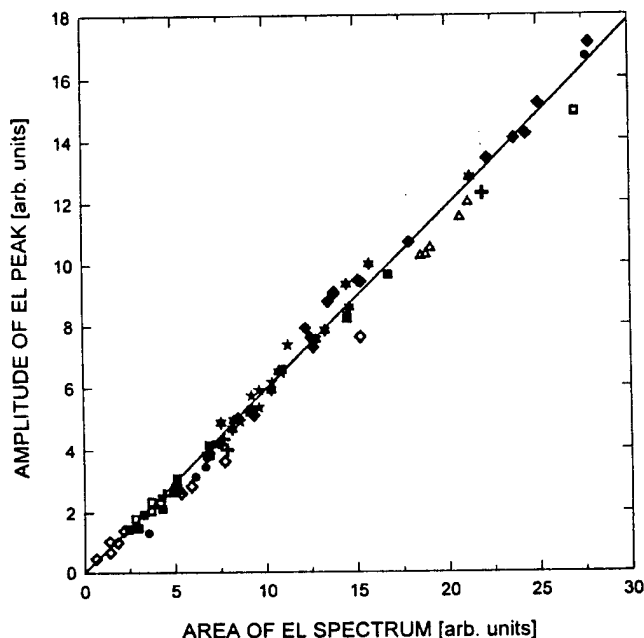


Fig. 2. EL peak amplitude as a function of the area of the spectrum. The various symbols (nine altogether) correspond to samples prepared under different anodization conditions, while the recurrence of the same symbol represents measurements at different times of the EL current flow.

talline silicon during current flow under similar conditions to those used for EL in porous silicon. Use was made of the space charge capacitance technique of the silicon–electrolyte interface [5]. Fig. 4 shows the growth of the oxide thickness with the time of the applied current. We see that the current flow causes an appreciable enhancement in the oxide thickness. It is only to

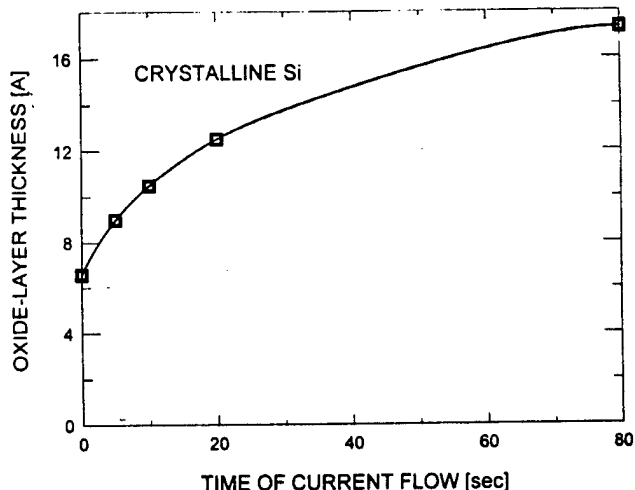


Fig. 4. Growth of the oxide-layer thickness on crystalline silicon with time of applied current.

be expected that the EL current induces an oxide growth in porous silicon as well.

Fig. 5 displays the PL spectra (solid curves) at the onset of the EL (curve 1) and after the EL disappears (curve 2). We see that due to the EL current flow, the red part of the PL practically disappears. As a result, the PL spectrum is appreciably narrower and blue shifted. For comparison purposes we replotted from Fig. 1 (dotted curves) the total EL emitted power (curve 3) and one of the last measured EL spectra (curve 4). The two curves were normalized to the respective PL curves. It is seen that each pair of curves coincide quite closely.

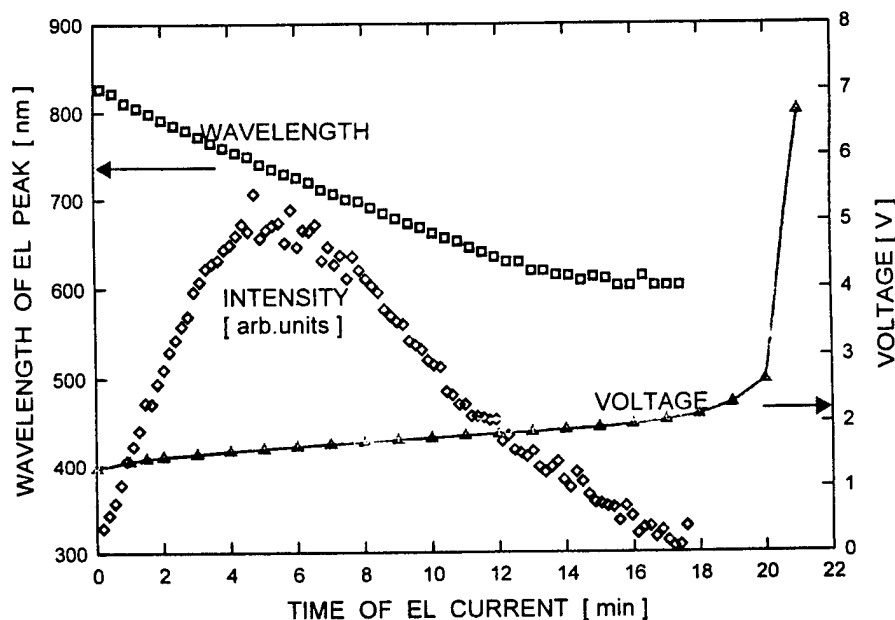


Fig. 3. Emitted EL power and wavelength of the spectral peak as functions of time. Also plotted is the time variation of the voltage across the sample.

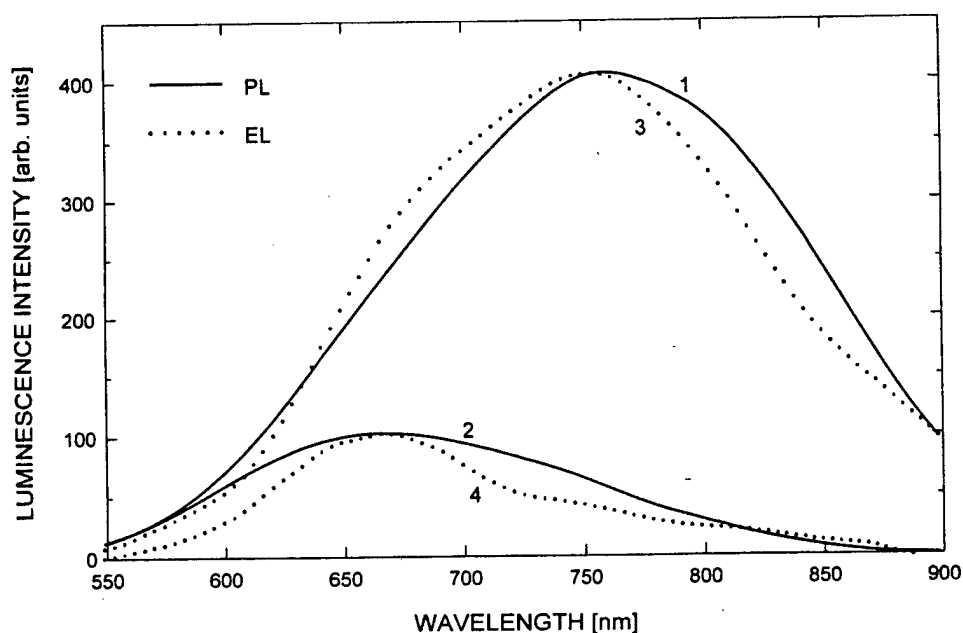


Fig. 5. PL spectra (solid curves) at the onset of the EL (curve 1) and after the EL disappears (curve 2). For comparison purposes, we replotted from Fig. 1 (dotted curves) the total EL emitted power (curve 3) and one of the last measured EL spectra (curve 4).

#### 4. Discussion

The blue shift of the EL peak with the EL time and the accompanying moderate increase of the voltage across the sample are somewhat similar to results obtained by Bsiey and Vial [6] and are probably due to the same mechanism. Because of quantum confinement, the energy gap associated with the nanocrystallites is higher, the smaller the size of the crystallite. At the beginning, the contribution to the EL is mainly from the larger nanocrystallites. This is because such particles are associated with smaller energy gaps so that electron injection from the electrolyte requires less energy (lower voltage). With time, these nanocrystallites become covered with an oxide due to the EL current flow. At this point the current is diverted to smaller nanocrystallites and electron injection into such crystallites requires a higher voltage. As pointed out above, the measurements were performed under constant current conditions and we see indeed from Fig. 3 that the voltage across the cell rises with the time of the EL current flow. The EL disappears when all of the nanocrystallites, large and small, become covered with an oxide. One might conceivably assume that the EL originates from band-to-band transitions and thus account for the blue shift as the EL current switches from larger to smaller nanocrystallites. Such a model, however, is inconsistent with some PL data. In the first place we reported previously [7] that the excitation of the PL is practically nonexistent in the range of wavelengths encompassed by the PL spectrum (above 600 nm). This suggests that the PL involves some intermedi-

ate localized states, and that the luminescence results from transitions between such states and either energy band. As the gap of the nanocrystallites involved increases, so does the energy separation between the states and the relevant band. Further information about the nature of the localized states is provided by the observation that the red part of the PL spectrum disappears at the end of the EL process (Fig. 3). This suggests that at least the localized states responsible for the red part of the spectrum reside at the surface of the nanocrystallites. Such states may be associated with adsorbed species and disappear upon oxidation.

In conclusion, it appears that in addition to quantum confinement, localized states play an important role in the luminescence process in porous silicon. Our combined results of EL and PL suggest that the states responsible for the red part of the spectrum reside at the surface.

#### References

- [1] L.T. Canham, *Appl. Phys. Lett.* 57 (1990) 1046.
- [2] I. Amato, *Science* 252 (1991) 22.
- [3] Z.C. Feng, R. Tsu, *Porous Silicon*, World Scientific, Singapore, 1994.
- [4] A.G. Cullis, L.T. Canham, P.D.J. Calcott, *J. Appl. Phys.* 82 (1997) 909 and references therein.
- [5] E. Savir, A. Many, Y. Goldstein, S.Z. Weisz, *J. Avalos, Surf. Rev. Lett.* 2 (1995) 765.
- [6] A. Bsiey, J.C. Vial, *J. Lumin.* 70 (1996) 310.
- [7] T.V. Torchinskaya, N.E. Korsunskaya, M.K. Sheinkman, L. Yu, Khomenkova, A.L. Kapitanchuk, Y. Goldstein, E. Savir, A. Many. *Proc. Int. Semiconductor Conf., CAS'98, Sinaia, October 1998* (Romanian Academy of Sciences, Bucarest, 1999), p. 451.

# Comparative analysis of the 1.54 $\mu\text{m}$ emission of Er-doped Si/SiO<sub>2</sub> films and the size distribution of the nanostructure

Luis F. Fonseca <sup>a,\*</sup>, O. Resto <sup>a</sup>, R.K. Soni <sup>a</sup>, M. Buzaiianu <sup>a</sup>, S.Z. Weisz <sup>a</sup>,  
M. Gomez <sup>a</sup>, W. Jia <sup>b</sup>

<sup>a</sup> Department of Physics, University of Puerto Rico, Rio Piedras 00931, Puerto Rico

<sup>b</sup> Department of Physics, University of Puerto Rico, Mayaguez 00681, Puerto Rico

## Abstract

Er<sup>3+</sup>-doped nanocrystalline-Si/SiO<sub>2</sub> composite films were synthesized by RF co-sputtering of bulk-Si, SiO<sub>2</sub>, and Er<sub>2</sub>O<sub>3</sub> targets. The visible and 1.54  $\mu\text{m}$  emission bands of the samples were measured, as well as their optical transmission. We varied the relative concentrations of Si, Er, and the annealing temperature. The nanoparticles size distributions of the samples were obtained from their optical transmission spectra. We analyzed the dependence of the characteristic 1.54  $\mu\text{m}$  Er-emission intensity on the size and concentration of the nanocrystalline particles and the dependence of the emission on the preparation conditions. © 2000 Elsevier Science S.A. All rights reserved.

**Keywords:** Nanostructure; Preparation conditions; Emission

## 1. Introduction

Recently, efficient light emission has been demonstrated by erbium (Er) incorporation into silicon [1]. The erbium ion, in its 3<sup>+</sup> state, emits photon in the infrared (IR) region at 1.54  $\mu\text{m}$  resulting from an intra 4f transition between the <sup>4</sup>I<sub>13/2</sub> state to the <sup>4</sup>I<sub>15/2</sub> state. This emission is particularly suitable for the low loss transmission through silica based optical fiber. The strong quenching of luminescence at room temperature (RT), through nonradiative decay channels, is considered to be a principal limitation for the development of Er-doped silicon devices. It has been shown that in the presence of impurities such as O and F, the reduction in the quenching as well as higher erbium solubility can be achieved [2,3].

Er-doped porous silicon, on the other hand, shows strong 1.54  $\mu\text{m}$  emission even at RT and a considerable weak thermal quenching [4]. It is argued that in the porous silicon, the Er<sup>3+</sup> excitation results from the recombination of the photoexcited carriers in the silicon nanocrystallites and subsequent energy transfer to Er<sup>3+</sup>. The modification in the band structure properties of

nanocrystalline silicon due to carrier confinement appears to favor energy transfer to Er<sup>3+</sup>. Indeed, in SiO<sub>2</sub> films containing nanocrystalline silicon and Er, a correlation between visible emission from the nanocrystallites and IR emission from Er<sup>3+</sup> was observed [5], which further corroborate that the IR emission of Er<sup>3+</sup> is mediated by the nanocrystallites.

In this paper we investigate the dependence of the 1.54  $\mu\text{m}$  emission intensity on the nanocrystal size and concentration in Er<sup>3+</sup> doped nanocrystalline Si/SiO<sub>2</sub> composite films. The films were prepared by varying the relative concentration of Si, Er, and the annealing temperature.

## 2. Results and discussion

The material was synthesized by RF co-sputtering. The sputtering setup that was used to prepare the samples included a Varian system in a target downside — substrate upside vertical configuration. The chamber had 62-l volume connected to a 2500 l s<sup>-1</sup> diffusion pump. A SiO<sub>2</sub> disk with 13.2 cm in diameter was used in the target configuration. The substrates were quartz plates with dimensions 12.6 × 1.1 × 0.09 cm<sup>3</sup>. A piece of crystalline silicon wafer with 7 cm<sup>2</sup> of area was

\* Corresponding author.

mounted on top of the SiO<sub>2</sub> target disk just below one end of the substrate deposition area. With such a configuration a density gradient of silicon along the sputtered film can be obtained in one sputtering session. The Er<sub>2</sub>O<sub>3</sub> material was obtained as a powder and then pressed and prepared as pellets.

The deposited films had an area of 11 × 0.44 cm<sup>2</sup> and the thickness was in the order of ~3.5 μm after 6 h of deposition. The sputtering was made with a residual gas pressure ~5 × 10<sup>-7</sup> Torr, Argon (99.9995%) pressure of 19 mTorr, 1100 V substrate-to-target voltage, 180 W forward power, and 2.5 W reflected power. The substrate-to-target distance was 5 cm. The substrate temperature raised up to ~130°C during the sputtering period. Previously to the deposition, the quartz substrates were cleaned by immersion in a HF (20%) water solution for 30 min and then washed with deionized water and dried with a nitrogen flux. After sputtering, the samples were annealed in a N<sub>2</sub>-rich atmosphere using a Lindberg Heavy Duty oven. The samples were kept in the oven during the heating-up and cooling-down periods.

Er-doped samples were synthesized by adding to the sputtering target configuration a line of small (~4 × 9 mm<sup>2</sup>) Er<sub>2</sub>O<sub>3</sub> pellets oriented along the substrate. The distance between each pellet and the next was ~7 mm and they were located just on top of the Si and SiO<sub>2</sub> targets. With this target configuration a quasi-uniform Erbium concentration was sputtered along the film. The samples were annealed at different temperatures from 1200 to 700°C. Auger Electron Spectroscopy (AES) gave an erbium concentration of 3.9% along the film. In

order to correlate the optical properties of the material with different density of the constituents, each film was divided in 50 segments (0.22 cm. in length) and labeled successively with the SiO<sub>2</sub>-rich end as the No. 1 and the other end as No. 50. We measured the optical transmission and the photoluminescence properties of each segment of the films in both the visible and the IR (near 1.54 μm) regions. The transmission spectra were obtained using a HP-8452A spectrophotometer and the photoluminescence was measured with an ISA-TRIAx 320 spectrometer.

Fig. 1 shows the IR-emission between 1500 and 1600 nm for a sample that was annealed at 700°C. Each curve corresponds to a different position along the film as written in the graph. Above position 30, Fig. 1 shows the characteristic emission of Er<sup>3+</sup>. The intensity of the IR emission increases as the silicon concentration does. This gives a clear indication that the Er-emission is enhanced by the presence of the silicon nanoparticles. Positions 30 and below that correspond to lower concentration of silicon give almost no emission. As mentioned above, it is expected that both the density and the size of the nanoparticles reduce when approaching the lower silicon concentration side of the film. At the same time during the sputtering, oxygen released from Er<sub>2</sub>O<sub>3</sub> can react with silicon and reduce even further the available amount of silicon required for the formation of the nanoparticles in this part of the film. The PL measurements of this film in the visible region give no direct emission from the nanoparticles at any of the studied positions. This can be explained as the quenching of the visible PL because of the energy transfer to the Er-emission for the samples where the IR emission is observed.

In order to correlate the IR emission with the size of the nanostructures, we determined the size of the particles at positions 35 and 45 by optical means. Fig. 2(a) shows the optical transmission spectra in the visible region of the film at those positions. The optical absorption edge shifts are attributed to the quantum enlargement of the effective energy gap of the particle when the size is reduced. From the optical transmission, we calculated the particle size distribution by assuming that, due to the electron quantum confinement, the energy dependence of the absorption coefficient for a silicon nanoparticle shows a sudden increase from zero to a finite value at the energy corresponding to the enlarged energy gap [6]. Under this assumption the size distribution is proportional to the derivative of the transmission versus energy curve. Fig. 2(b) shows the normalized size distributions obtained from the optical transmission data at the same points, 35 and 45. The maximum of the distribution changes from 1.18 nm at point 35 to 1.8 nm at point 45.

The as-sputtered silicon concentration at each site was obtained from the determination of the film thick-

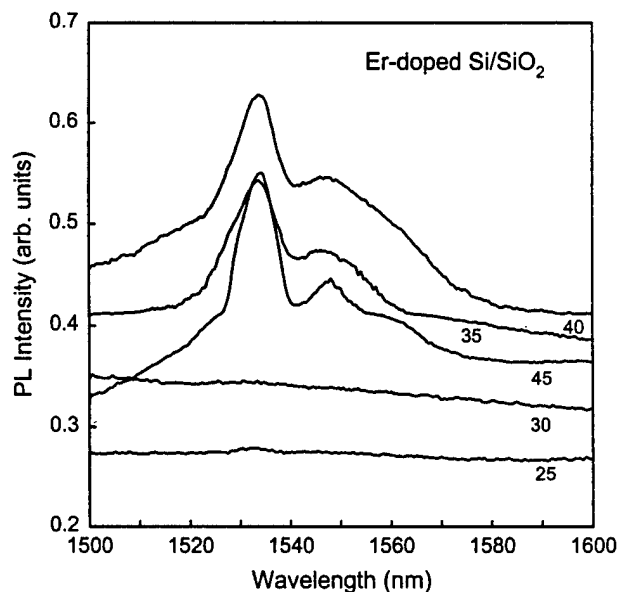


Fig. 1. Infrared emission spectra from uniformly Er-doped Si/SiO<sub>2</sub> films annealed at 700°C and excited with 488 nm laser line. The number on each spectrum designates the segment number of the film.

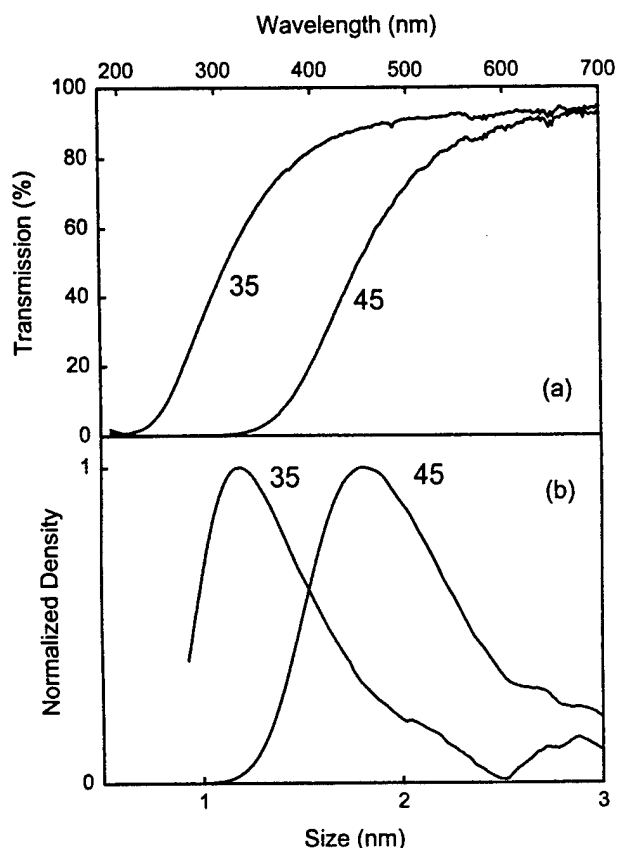


Fig. 2. (a) Optical transmission spectra from segment 35 and 45 of a uniformly Er-doped Si/SiO<sub>2</sub> film annealed at 700°C. (b) Calculated normalized Si-nanocrystal size distribution at the positions where transmission spectra were taken.

ness, measured with a Sloan Dektak Surface Profilometer, and the Hanak et al. algorithm [7]. With the silicon concentration data and the particle average size assigned to each site from Fig. 2(b), the density of particles can be estimated at each position assuming that all the silicon excess has been grown into particles. In that case the silicon density at position 35 is 0.93% and the particle density  $\sim 1.08 \times 10^{19}$  part per cc and at position 45 the silicon density is 2.3% and the particle density  $\sim 7.53 \times 10^{18}$  part per cc. These numbers and the fact that the maximum of the IR-emission at position 45 is larger than the IR-emission at position 35, brings us to the conclusion that the energy transfer in the sample with particles of the size of  $\sim 1.8$  nm is enhanced as compared with the sample with particles of  $\sim 1.18$  nm in size. It is worth noting that, according to the statement that oxygen coming from the sputtering of the Er<sub>2</sub>O<sub>3</sub> pellets can oxidize the silicon during the film formation, the silicon concentration used on the above calculations can be overestimated specially at position 35, where the silicon concentration is lower.

To study how the variation of the erbium concentration changes the optical properties of the system, the sputtering-target configuration was changed by replac-

ing the line of small pellets oriented along the film by only one Er<sub>2</sub>O<sub>3</sub> pellet with 13 mm in diameter located below the center of the substrate. In such a way the erbium concentration will change down from close to the center to both ends. Fig. 3(a) shows the IR emission at positions 20 and 28 of a film that was prepared with the new target configuration and annealed at 900°C. The figure shows a reduction of the IR emission at position 20, where the amount of erbium is lower as compared with position 28. Fig. 3(b) shows the correspondent visible emission that is related with the PL of the silicon nanoparticles. The intensity of the visible PL increases when the IR emission intensity reduces.

Another sample was prepared using the new target configuration and annealing the film at 700°C. This sample showed strong IR emission and non-detectable visible emission as in the case of the first sample that was also annealed at the same temperature. Fig. 4(a) shows the dependence of the IR emission intensity as a function of the position. The curve shows that the PL decreases when the position moves to the ends where the erbium concentration reduces and the PL curve is not symmetric with larger intensity where the silicon concentration and silicon nanoparticles are larger as in

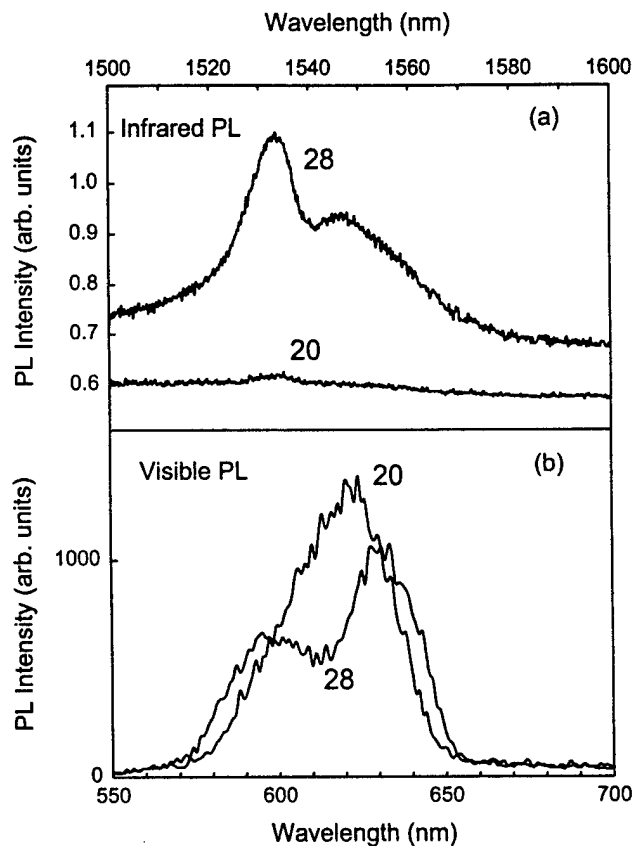


Fig. 3. (a) Infrared emission spectra from non-uniformly Er-doped Si/SiO<sub>2</sub> films annealed at 900°C excited with 488 nm laser line. The number on each spectrum designates the segment number of the film. (b) Visible PL at the same positions, where IR emission is also seen.

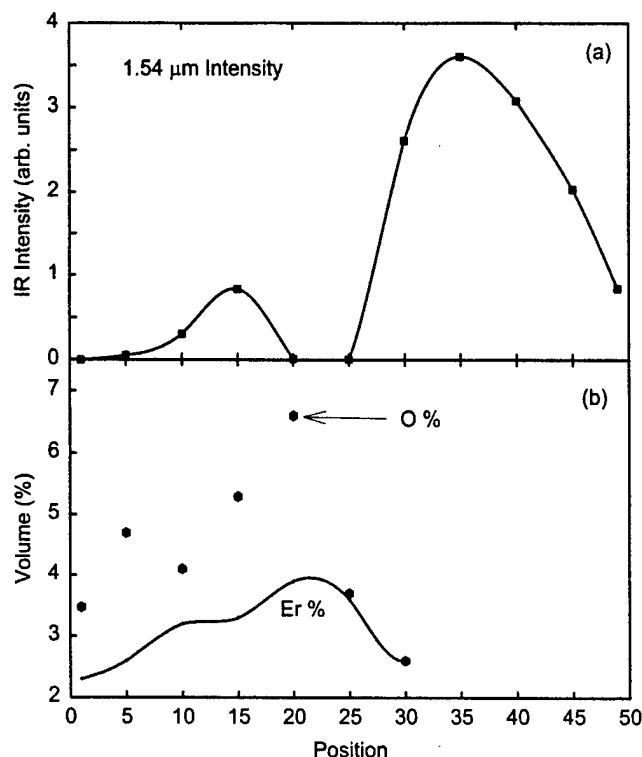


Fig. 4. (a) Variation of 1.54  $\mu\text{m}$  peak intensity with position on the film, and (b) variation of Er and oxygen concentration measured by Auger spectroscopy with position on the film. Positions 1 and 50 are assigned the  $\text{SiO}_2$  rich and Si rich sites, respectively, on the film.

the case of the sample of Fig. 1. An interesting feature is observed at positions where the erbium concentration is maximum (around the center of the film), the PL is quenched at these sites. This observation also suggests that the silicon oxidized at this region because of the increasing amount of oxygen coming from the  $\text{Er}_2\text{O}_3$ . This conclusion is supported by the fact that there is a bleaching of the film at these positions. We included in Fig. 4(b) the erbium and oxygen concentrations measured by Auger spectroscopy. The curves support the fact that the increasing of the Er-concentration is also accompanied by large amounts of oxygen due to the target composition that will promote the silicon oxidation and the quenching of the IR emission.

### 3. Conclusions

We have synthesized  $\text{Er}^{3+}$  doped nanocrystalline

$\text{Si/SiO}_2$  composite films on quartz plates by RF sputtering using  $\text{Er}_2\text{O}_3$ , crystalline silicon and  $\text{SiO}_2$  targets. During the process we varied the relative concentration of Si, Er and the annealing temperature. The characteristic 1.54  $\mu\text{m}$  emission is found to be sensitive to the Si nanocrystallite density, size, Er concentration and oxygen incorporation in the film. At low temperature annealing ( $700^\circ\text{C}$ ), both uniform and non-uniformly Er-doped samples exhibit pronounced IR emission in the high Si nanocrystallite density region. This clearly suggests that the IR emission is being enhanced by the presence of the Si nanocrystallites and that high Si nanocrystallite density is essential. At higher annealing temperature ( $900^\circ\text{C}$ ), both visible and IR emission were measured and we observed a correlation between the 1.54  $\mu\text{m}$  emission and the energy transfer between the  $\text{Er}^{3+}$  and the Si nanoparticle. On the other hand, IR emission efficiency depends not only on the silicon particles density and Er concentration but also on the size of the nanocrystallites. We observed that, at the particles size range we were working ( $\sim 1.2$  to  $\sim 2$  nm), larger particles produce larger enhancement of the IR emission. The use of  $\text{Er}_2\text{O}_3$  as sputtering target can also introduce large amounts of oxygen and prevent the silicon particles formation when increasing density of erbium is required.

### Acknowledgements

This work was supported by US ARO-DAAH04-96 grant.

### References

- [1] S. Coffa, G. Franzo, F. Priolo, MRS Bulletin, April 1998, 25.
- [2] S. Coffa, G. Franzo, F. Priolo, A. Poloman, R. Serna, Phys. Rev. B 49 (1994) 16313.
- [3] J. Stimmer, A. Reittinger, J.F. Nützel, H. Holzbrecher, Ch. Buchal, G. Abstreiter, Appl. Phys. Lett. 68 (1996) 23.
- [4] X. Wu, U. Hömmerich, F. Namavar, A.M. Cremins-Costa, Appl. Phys. Lett. 69 (1996) 1903.
- [5] M. Fujii, M. Yoshida, S. Hayashi, K. Yamamoto, J. Appl. Phys. 84 (1998) 4525.
- [6] L.F. Fonseca, O. Resto, R. Katiyar, S. Gupta, S.Z. Weisz, Y. Goldstein, A. Many, J. Shapir, Proceedings of the 24th ICPS (CD version), D. Gershoni (Ed.), World Scientific, 1999.
- [7] J.J. Hanak, H.W. Lehman, R.K. Wehner, J. Appl. Phys. 43 (1972) 1666.

## STUDY OF THE LUMINESCENCE OF Eu-DOPED NANOCRYSTALLINE Si/SiO<sub>2</sub> SYSTEMS PREPARED BY RF CO-SPUTTERING

G.A. NERY\*, A. MAHFOUD\*\*, L.F. FONSECA, H. LIU\*\*, O. RESTO, AND S.Z. WEISZ

Physics Department, University of Puerto Rico, San Juan, PR, USA.

\*Physics and Chemistry Department, University of Puerto Rico, Arecibo, PR, USA.

\*\*Physics Department, University of Puerto Rico, Mayaguez, PR, USA.

### ABSTRACT

We prepared Eu-doped films of Si nanoparticles embedded in SiO<sub>2</sub> using pellets of Eu<sub>2</sub>O<sub>3</sub> by sputtering. We studied their photoemission, transmission and fluorescence to obtain data about their composition and particle size and the Eu interaction characteristics. We were able to incorporate Eu(III) into the Si nanoparticle / SiO<sub>2</sub> host. We also found we obtained Eu(II) in the process. We found a lowering of photoluminescence intensity with lowering of temperature. An as yet unanswered question is the reason for the intense whitish luminescence found in some regions of the samples. Some involvement with Eu(II) is suspected. Eu(III) related peaks were only observed where the size distribution peak of the nanoparticles was lower than 1.3nm. Whitish luminescence was related to peak sizes ranging from 1.1nm to 1.4nm. Annealing the samples had clear effects upon their photoluminescence, but did not necessarily involve changes in particle sizes, nor were these size changes necessary to increase luminescence. The Eu doping has a tendency to halt the annealing effects on size and, when changes did occur, the particles generally became smaller.

### INTRODUCTION

Europium is an interesting material when incorporated as a dopant into solid state materials. This is because trivalent Eu(III) ions can be used as a structure probe, and due to its large quadrupole splitting and spin-lattice relaxation times, Eu(III) is particularly attractive in high-resolution laser spectroscopy [1]. One proposed application is in a frequency domain optical data memory, based on the large ratio of inhomogeneous-to-homogeneous line widths present. In some solid state materials the Eu(III) dopant ions exhibit the longest ever dephasing time of 822 $\mu$ s and the narrowest homogeneous line width at low temperature [2]. This has stimulated interest in searching for appropriate materials to host Eu(III) ions, which could be optimized for operation at room temperature.

We have produced and studied Si/SiO<sub>2</sub> material in which visible light emitting Si nanoparticles are embedded in a SiO<sub>2</sub> matrix. We made subsequent studies incorporating another rare-earth metal, Er, into the Si nanoparticle embedded SiO<sub>2</sub> matrix and verified that the luminescence of Er is enhanced due to energy transfer between the nanoparticles and the Er [3].

These considerations led us to attempt to ascertain the interactions between Eu and this new host material. Due to the amorphous nature of the SiO<sub>2</sub> material prepared by this particular technique, the dopant europium ions must experience large variations of their environment. Additionally, some Eu(III) ions may be placed at the Si nanoparticle / SiO<sub>2</sub> interface while the others are inside the SiO<sub>2</sub> host. This would produce fluorescence line broadening. Also, our use of Eu<sub>2</sub>O<sub>3</sub> as the source of our dopant could lead to interactions between the oxygen thus incorporated into our samples and the Si, as had apparently happened in our previous Er incorporation experiments.



## EXPERIMENT

We combined  $\text{Eu}_2\text{O}_3$ , Si and  $\text{SiO}_2$  producing a series of samples by Ar sputtering deposition on quartz substrates. We produced samples with Si and  $\text{SiO}_2$ ;  $\text{Eu}_2\text{O}_3$  and  $\text{SiO}_2$ ;  $\text{Eu}_2\text{O}_3$  and Si; and  $\text{Eu}_2\text{O}_3$ , Si and  $\text{SiO}_2$ . The samples were made by a 12hr deposition. The plates holding the sample and the target materials reached temperatures in the vicinity of  $110^\circ\text{C}$ . The target voltage was 1100V with a 0.12A plate current.

The largest portion of the target was a 13.2cm diameter disk of  $\text{SiO}_2$  (except for the  $\text{Eu}_2\text{O}_3$  with Si sample, in which case it was a disk of Si). When including Si in the sample (for the nanoparticles) we placed a 3.00cm by 2.30cm Si rectangle on the border of the  $\text{SiO}_2$  disk. The 14cm x 1cm x 0.1cm rectangular quartz substrate was placed with one end above the Si rectangle and oriented almost along the diameter of the  $\text{SiO}_2$  disk. The target to substrate distance was about 5cm. This produced a gradient in the Si concentration along the sample. The  $\text{Eu}_2\text{O}_3$  pellet was a half-circle placed with its 1cm diameter perpendicular to the length of the substrate. For different samples, the pellet's position was varied from being next to the Si rectangle, to beneath approximately halfway along the substrate, to a bit beyond the substrate on the side opposite to the Si rectangle. This way we could see the effects of a variety of Si-Eu combination proportions. The  $\text{Eu}_2\text{O}_3$  /  $\text{SiO}_2$  sample had the pellet near the center. The  $\text{Eu}_2\text{O}_3$  / Si sample had it near one edge of the sample. The samples were marked lengthwise. Position 50 is closest to the Si.

We measured the luminescence and transmission of the samples, and then annealed them at  $700^\circ\text{C}$ , except in the case of pure Si with  $\text{SiO}_2$ , which was annealed at  $1100^\circ\text{C}$ . Annealing took place in a Lindberg Heavy Duty Oven in a  $\text{N}_2$  or Ar rich atmosphere. Annealing the as-sputtered Si/ $\text{SiO}_2$  at  $1100^\circ\text{C}$  results in Si nanoparticles with sizes ranging from about 1 to greater than 3nm, with the dominant sizes ranging from about 1.0 to 2.1 nm as we go from position 1 to position 50. We observed that higher annealing temperatures result in smaller particles and less variation in size at each position and overall. Annealing should help crystallization and other bond formation processes, and perhaps nanoparticle growth, but some oxidation could also take place with  $\text{O}_2$  from the atmosphere (or, in the Eu-doped samples, from the  $\text{Eu}_2\text{O}_3$ ). For Er doped Si/ $\text{SiO}_2$   $700^\circ\text{C}$  was sufficient [4], and we tried it for Eu.

The photoluminescence was measured with an Argon laser 514.5nm beam. We used an ISA Triax 320 spectrometer. We measured the luminescence of the  $\text{Eu}_2\text{O}_3$  pellet and a  $\text{EuCl}_3$  pellet to characterize the Eu(III) luminescence peaks for comparison with our samples. The results were comparable to others found in the literature [4]. A CW Ar laser at 488nm and a high power pulsed YAG laser were used for further studies to again observe the general behavior and also identify the components of the luminescence via luminescence decay and time resolved spectroscopy measurements.

## RESULTS

The  $\text{Eu}_2\text{O}_3$  /  $\text{SiO}_2$  samples were transparent and colorless. The  $\text{Eu}_2\text{O}_3$  / Si sample looked like Si. The Si /  $\text{SiO}_2$  sample was caramel like at the Si rich end, getting lighter in color until about three centimeters from the Si side it was almost transparent, and finally completely transparent at the Si poor end. The  $\text{Eu}_2\text{O}_3$  / Si /  $\text{SiO}_2$  samples were the same as the Si /  $\text{SiO}_2$  samples except that in the vicinity of where the Eu pellet had been the Si caramel color (when present) gave way to transparency. If this "bleaching effect was due to  $\text{Eu}_2\text{O}_3$  donating some of its oxygen atoms to Si, the oxidizing of Si would have to be accompanied by a change in the Eu bonding. In  $\text{Eu}_2\text{O}_3$  we have Eu(III) present. Upon donating the oxygen it could become Eu(II), which is also a relatively stable valence state for Eu.

The photoluminescence (PL) studies with the 514.5nm Ar laser showed two types of spectra. On the one hand we saw wide bands (from 550nm-800nm) with peaks in the vicinity of 600-680nm. On the other hand, we saw a well defined peak at 619nm. This peak only occurred in Eu doped samples and corresponded to the  $^5D_0$ - $^7F_2$  Eu(III) transition. Quite a few times we saw the Eu(III) peak piggybacked atop one of the larger bands. In those cases the bands tended to be triangular in shape (Fig. 1).

The as-sputtered samples were also viewed under the light of a 366nm u-v lamp. To the naked eye, a strong whitish luminescence was observed on either side of the  $\text{Eu}_2\text{O}_3$  pellet position in the  $\text{Eu}_2\text{O}_3$  / Si /  $\text{SiO}_2$  samples, while the position corresponding to the pellet itself tended to be transparent and not luminescent. Farther off this luminescence ceased. The positions where the whitish luminescence occurred were somewhat affected by annealing later. It should be noted that the whitish luminescence occurred in non-caramel areas in the sample but not in the most Eu rich bleached areas centered where the Eu pellet was located. The lone exception may have occurred where the Si rich side was bleached when the Eu pellet was next to the Si rectangle. This luminescence had not been observed either in the Si,  $\text{SiO}_2$  samples or a series of  $\text{Er}_2\text{O}_3$ , Si,  $\text{SiO}_2$  samples. The source for this luminescence was not clear. We considered that the Eu could be serving as a nucleation center for the growth of Si nanoparticles and that they be present even before annealing, but we had never observed a whitish luminescence nor one as strong as we were seeing due to only Si nanoparticles. Another option was that the Eu itself was emitting.

The transmission measurements were used to obtain the size distributions of the Si nanoparticles through the derivative of the transmission curves. From each of these distributions, the peak position was used to obtain the size of the most numerous particles [5]. We assumed the absorption is from the nanoparticles and that they are of spherical shape for these calculations. Distribution peak particle sizes were found to range from 1.0nm to 2.1nm among the  $\text{Eu}_2\text{O}_3$  / Si /  $\text{SiO}_2$  samples while sizes go up to 2.2nm in the Si /  $\text{SiO}_2$  sample. As we continue it is to these distribution peak particle sizes to which we will refer.

All the Si containing samples showed variation in size of the particles with position along the sample. However, it was present before annealing and, we did not detect significant changes in that particle size (Fig. 2a) upon annealing except in the sample where the Eu pellet was on the side opposite to the Si rectangle. In this latter case the changes occurred only after about the midpoint of the sample, on the Si rich side. In fact, in this case the particles did not grow but rather reduced in size. These changes may have been due to an oxidation process with oxygen from the  $\text{Eu}_2\text{O}_3$  doping material. Interestingly enough, also, the changes in size began just at the location where the whitish luminescence occurred. It would seem that the  $\text{Eu}_2\text{O}_3$  was interfering

because the particles sizes vary along the whole length of the Si /  $\text{SiO}_2$  sample (Fig. 2b).

Upon annealing the luminescence peaks in the Eu opposite side to Si sample shifted to lower wavelengths values after annealing. This also occurred in the Eu and Si on the same side sample. The Eu opposite side to Si sample showed a large increase in absolute and relative

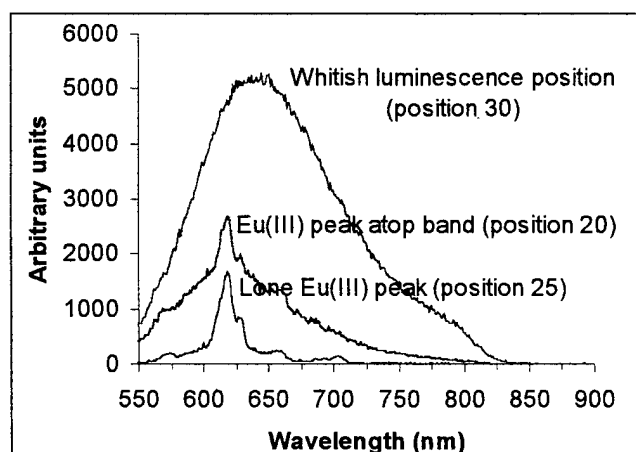


Figure 1 Photoluminescence with 514.5nm excitation. Sample with:  $\text{Eu}_2\text{O}_3$  (middle) / Si /  $\text{SiO}_2$ , positions 20, 25, 30.

luminescence in the Si rich Eu poor side, beginning at the whitish luminescence location and correlated with the increasing particle size region where the change in size also occurred. No changes in size occurred in the Eu in the middle sample. In all Eu containing samples, other luminescence changes also occurred (Fig. 2a).

The very bleached Eu rich locations tended to show the Eu(III) peak both before and after annealing. They did not occur at the high Si concentration areas. Particle sizes ranged from 1.1nm to 1.3nm in these regions. To the sides of these regions we noticed an intense band of luminescence similar in shape and peak position (640-650nm) to that of the Si / SiO<sub>2</sub> bands. These correspond to the positions at which we saw the whitish luminescence present before and after annealing. The particles ranged from 1.1nm to 1.4nm there. Farther from these areas, we reach the positions at which we could find Eu(III) peaks piggybacked atop bands. These were seen after annealing in locations where previously there was a band. The bands luminescence was reduced relative to the other locations after annealing. They occurred in the lower Si concentration areas. Particle sizes here were lower than 1.3nm. Only one piggyback case occurred between the Eu(III) peak and the whitish luminescence position. It occurred in a relatively large Si concentration (for these peaks) and also large Eu concentration area (right next to the Eu(III) peak) in the Eu at the middle sample. It almost disappeared completely both relative to the rest and in absolute terms. Particle size here and in the whitish luminescence position next to it was 1.3nm, and in the pure Eu(III) peak position particle size was 1.1nm.

With respect to the cause for the strong whitish luminescence, various sources indicate that Eu(II) can luminesce in the visible range, with a very wide band going from IR to UV with a maxima in the green region of the spectrum [6, 7, 8, 9]. Given that it was possibly due to Eu(II) but our deposition source had Eu(III) we had to check for a clear Eu(II) signal. The problem was that in the whitish luminescence regions of our samples we would observe a Si / SiO<sub>2</sub> like curve upon illuminating with our 514.5nm laser (albeit a very strong one relative to the rest). Finally, to excite Eu(II) we might need photons in the blue to u-v region [9]. Since we observe the whitish luminescence under u-v light, this might indicate that Eu(II) is the actual source, even if we only observe the nanoparticles with our 514.5nm or other blue source.

Time-resolved fluorescence measurement was employed to identify the origin of the observed photoluminescence. Using a CW Ar laser tuned at 488 nm the general behavior of the observed integrated fluorescence was characterized by a broad band feature with the peak varying in the region of 600 - 750 nm, recognizable as the luminescence from Si/SiO<sub>2</sub> host material [10-12]. The measured luminescence decay was very fast with a lifetime typically

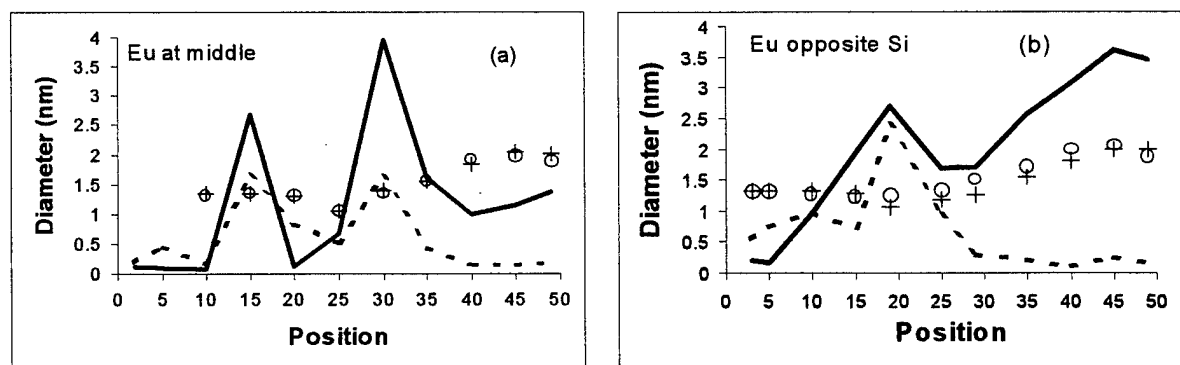


Figure 2 Sizes of particles (in nm) and maximum photoluminescence values (in arb. units) versus position. Solid line and crosses: photoluminescence and particle size, respectively, after annealing. Dotted line and circles: photoluminescence and particle size, respectively, before annealing

being  $< 10$  ns [10]. For some samples the fine PL features from Eu(III) emission which is overlapped with host emission could be identified.

Using a high-power pulsed YAG laser with a pulse width of 30 ps as a light source the PL decay at  $\sim 600 - 620$  nm was carefully examined. We identified 2 components. Right after excitation a fast decay component occurs with a lifetime of 800 ns followed by a buildup of a long-lived signal which has a lifetime of 2 ms. Time-resolved spectroscopy was thereafter used to separate the two PL components.

Setting a gate width of 400ns with the delay at 300ns (to eliminate the host emission) a broadband luminescence was obtained, it was PL from Eu(II) ions. In order to verify this, a sample without the Europium dopant was measured. With the same setup, in this other sample no fast PL component nor long-lived component could be observed. This pointed to the possible origin of the observed fast PL in Eu-doped sample as divalent europium ions.

Eu(II) has an  $f^7$  electron configuration. The ground state, 3.8 eV below the conduction band, is the  $^8S_{7/2}$  level and the first excited state is  $^6P$  level of the  $4f^65d$  electron configuration. The characteristic optical absorption band of ground state  $^8S_{7/2}$  to excited state  $^6P$  transition is at around 270 - 300 nm. Using the 3<sup>rd</sup> harmonics of an intense YAG laser operating at 355 nm, this PL was just observable, but overlapped by a strong Eu(III) emission. Using the laser operating at 532 nm with a high-power output of  $\sim 27$  GW/cm<sup>2</sup>, we increased the relative intensity of Eu(II) w/r Eu(III). The two-photon-absorption (TPA) induced Eu(II) emission is shown in Fig.3. This photoluminescence has a lifetime of  $\sim 800$ ns, the peak is at  $\sim 540$  nm, and FWHM is  $\sim 4200$  cm<sup>-1</sup>. This emission profile looks similar to the PL from the Si nanoparticles and from defect centers in SiO<sub>2</sub> as well [13]. But the lifetime measurement as well as the experimental results with the non-doped sample convinced us in making the judgement.

The luminescence from Eu(III) ions showed a well resolved feature in the range of 575 nm to 705 nm. The PL intensity versus temperature showed an interesting behavior. It was found to decrease with lower temperature. Presumably it is associated with the phonon-assisted photodynamical processes in the host conduction band. Its emission decay rate is 3 orders of magnitude greater than that of Eu(II). With a large delay of the sampling gate the fluorescence spectra of Eu(III) was obtained as in Fig.4. It shows a nature typical of Eu(III) in an amorphous host. Its PL profile consists of 5 emission groups. In the spectral range from 584 to 609 nm there is a triplet structure. At first glance it looks like the triple components of the transition from metastable  $^5D_0$  to  $^7F_1$  state with  $j = 0, \pm 1$ . If the first peak at 580 nm of the triplet were assigned to  $^5D_0 - ^7F_1$  transition, the  $^5D_0 - ^7F_0$  transition would occur at an even shorter

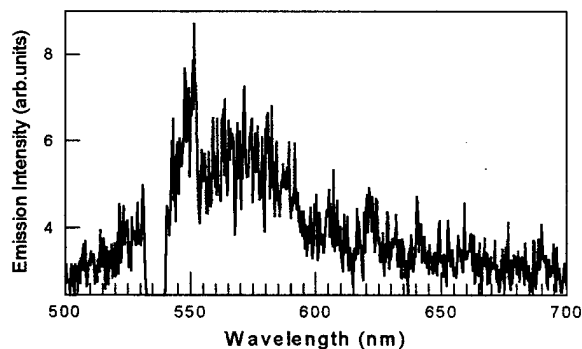


Figure 3. TPA-induced Eu(II) PL in Si/SiO<sub>2</sub>. Data points are missing at laser wavelength.

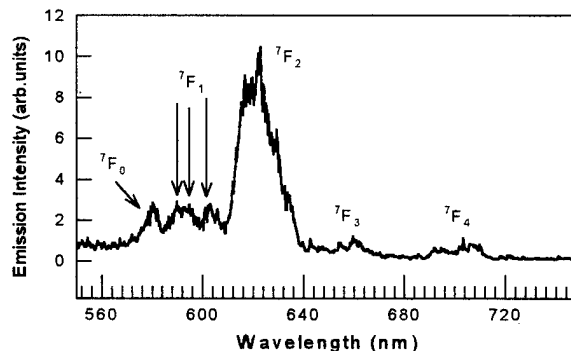


Figure 4. PL of Eu(III) dopant in Si/SiO<sub>2</sub> at 25°C. The transitions are labeled.

wavelength. This is inconsistent with most data obtained for Eu(III) in crystals. Actually, the component in the middle at ~590 nm is broadened, can be seen as a twin peak due to the superposition of two subcomponents. Therefore the spectral features within 584 - 609 nm can be assigned to the  $^5D_0 - ^7F_1$  transition while the first peak at 580 nm is assigned to  $^5D_0 - ^7F_0$ . An intense emission peaked at 622 nm is due to the  $^5D_0 - ^7F_2$  transition. The other two weak groups of emission at longer wavelengths of 659 and 703 nm belong to the transitions of  $^5D_0 - ^7F_3$  and  $^5D_0 - ^7F_4$  respectively. All components were well resolved at room temperature.

## CONCLUSIONS

We were able to incorporate Eu(III) into the Si nanoparticle / SiO<sub>2</sub> host. We also found we obtained Eu(II) in the process. We found a lowering of photoluminescence intensity with lowering of temperature. An as yet unanswered question is the reason for the intense whitish luminescence found in some regions of the samples. Some involvement with Eu(II) or Eu(III) is suspected. Eu(III) related peaks were only observed where the peak distribution size of the nanoparticles was lower than 1.3nm. Whitish luminescence was related to peak sizes ranging from 1.1nm to 1.4nm. Annealing the samples had clear effects upon their photoluminescence, but did not necessarily involve changes in particle sizes, nor were these size changes necessary to increase luminescence. The Eu doping has a tendency to halt the annealing effects on size and, when changes did occur, the particles generally became smaller.

## ACKNOWLEDGEMENTS

The authors acknowledge partial support from US ARO grant No. DAAH04-96 and NASA grant No. NCCW-0088.

## REFERENCES

1. R.M. Macfarlane and R.M. Shelby, in *Spectroscopy of Solids Containing Rare-Earth ions*, ed., by A.A. Kaplyanskii and R.M. Macfarlane (North-Holland, Amsterdam, 1987) 51.
2. R. Yano, M. Mitsunaga and N. Uesugi, *J. Opt. Soc. Am. B* **9**, 992 (1992).
3. L. F. Fonseca, O. Resto, R. K. Soni, M. Buzaianu, S. Z. Weisz, and M. Gomez, to be published in *Materials Science and Engineering B*
4. R. Reisfeld, R. A. Velapoldi, L. Boehm and M. Ish-Shalom, *The Journal of Physical Chemistry* **75**, 3980 (1971).
5. L. F. Fonseca, O. Resto, S. Gupta, R. S. Katiyar, S. Z. Weisz, Y. Goldstein, A. Many, and J. Shapir, *Proc. of the ICPS. CD-version* (1998).
6. M. Nogami and Y. Abe, *App. Phys. Lett.* **69**, 3776 (1996).
7. E. Kaldis, P. Streit and P. Wachter, *J. Phys. Chem. Solids* **32**, 159 (1971).
8. J. Qi, T. Matsumoto, M. Tanaka, and Y. Masumoto, *App. Phys. Lett.* **74**, 3203 (1999).
9. M. Nogami, T. Yamazaki, and T. Abe, *J. of Luminescence* **78**, 63 (1998).
10. D.B. Geohegan, A.A. Puretzky, G. Duscher and S.J. Pennycook, *Appl. Phys. Lett.* **73**, 438 (1998).
11. P. Li, G. Wang, Y. Ma and R. Fang, *Phys. Rev. B*, **58** (1998) 4057.
12. V.M. Akulin, E. Borsella, G. Onida, O. Pulci and A. Sarfati, *Phys. Rev. B*, **57** (1998) 6514.
13. N. Itoh, T. Shimizu-Iwayama, T. Fujita, *J. Non-Cryst. Solids* **179**, 194 (1994).